IPP-Report

Jonas Puchmayr

Optimization of Pedestal Stability on ASDEX Upgrade

Optimierung der Plasmarand-Stabilität an ASDEX Upgrade

Optimization of Pedestal Stability on ASDEX Upgrade

Optimierung der Plasmarand-Stabilität an ASDEX Upgrade

_____

Masterarbeit an der Fakultät für Physik
der Ludwig-Maximilians-Universität München

Jonas Puchmayr

München, den 22.10.2020

Prüfer: Prof. Dr. Hartmut Zohm

Betreuer: Dr. Michael G. Dunne, Prof. Dr. Hartmut Zohm

Contents

Abstract

In the high confinement mode (H-mode) of Tokamak plasmas, a region of strongly reduced heat and particle transport builds up at the plasma edge. Consequently, the thermodynamic profiles (pressure, temperature and density) in the H-mode are characterized by steep gradients in the plasma edge region, while the core profiles are raised as if they were on a growing pedestal. For this reason, the plasma edge in H-mode plasmas is also known as the "pedestal".

While the transport barrier results in significantly enhanced pressure, temperature and energy confinement, the pedestal provides the energy to drive a new type of plasma instabilities localized at the plasma edge, which are called Edge Localized Modes (ELMs). Large ELMs, so-called type I ELMs, cause massive bursts of lost energy and particles that limit the achievable pedestal top pressure (pedestal height) and will lead to severe damage on the vessel for future fusion devices. Hence, for the operation of future fusion devices in H-mode, it is inevitable to understand the physics of ELMs. Pedestal stability against type I ELMs is well-described by the theory of ideal magnetohydrodynamics, where ELMs are identified with the occurrence of two classes of instabilities, peeling and ballooning modes. However, in general the coupling of these modes is complex and has to be determined numerically. A predictive model for pedestal stability, the EPED framework, which generates model thermodynamic profiles and determines ideal growth rates, was developed previously. This framework predicts a stability regime at significantly enhanced pedestal pressures, the so-called Super H-mode, that can only be experimentally accessed by varying the plasma density. Recently, another predictive model, IPED, was developed which is based on the EPED definitions for the model density and temperature profiles but determines ideal growth rates based on a different stability code.

In this work, a new procedure which estimates the equilibrium area and volume profiles in flux coordinates was developed in order to improve the normalization of pressure and current density profiles generated by the IPED framework. In addition, the IPED framework is expanded by a new model calculating the edge current density, which was recently developed. The upgraded IPED framework is used to determine pedestal stability over a large range of plasma parameters. Firstly, in contrast to predictions of the EPED framework, we generally observe intermediate mode numbers to block access to the Super H regime. In this context, the influence of different stability criteria and model specific details was tested, showing no tendencies towards a Super H solution. That aside, we observe a similar structure of the stability boundary in the EPED parameter space, which is the space of pedestal top pressure and electron density (p-n space), where "peeling" modes are destabilizing at lower densities and "ballooning" modes are destabilizing at higher densities. Furthermore, dimensionless scaling laws for the critically stable pedestal top pressure were determined, highlighting the beneficial impact of positive triangularity and large edge safety factor on the pedestal stability. As a result, it is suggested to operate at high positive triangularity and high toroidal magnetic field at a density slightly below the density at which the stability regime transitions from "peeling" to "ballooning" limited, in order to optimize the pedestal top pressure. To interpret our findings, simple analytical mappings were derived which relate stability diagrams in s-α and p-n space, where the former is a natural space for describing peeling and ballooning stability. The numerically predicted p-n diagrams aligned well with the analytical predictions using the derived transformation to p-n space.

Zusammenfassung

Das Regime hohen Einschlusses (H-Mode) in Tokamak Plasmen zeichnet sich durch eine Region stark reduzierten Wärme- und Teilchentransports am Plasmarand aus. Auf Grund des verminderten Transports entstehen starke Gradienten der Druck-, Dichte- und Temperaturprofile am Plasmarand, während die Profile im Plasmain-neren wie auf einem wachsenden Podest angehoben werden.

Die Transportbarriere führt zu einer erheblichen Steigerung von Druck, Temperatur und Energieeinschluss im Plasmainneren. Die starken Gradienten in der Randre-gion ermöglichen jedoch die Entstehung einer neuen Art von Instabilitäten, welche am Plasmarand lokalisiert sind. Diese werden im Allgemeinen "Edge Localized Modes" (ELMs) genannt. Besonders starke ELMs (Typ I ELMs) führen zu einem massiven Verlust von Teilchen und Energie auf kurzen Zeitskalen und beschränken damit den maximalen Druck im Plasmarand. Zudem schädigen die Ausbrüche das Vakuumgefäß größerer Fusionsreaktoren erheblich. Ein tiefgründiges Verständnis der ELMs ist somit für den Betrieb von zukünftigen Fusionsmaschinen essenziell. Die Stabilität des Plasmas gegen Typ I ELMs wird gut von der idealen Magnetohydrody-namik beschrieben, wobei ELMs durch zwei Klassen von Randinstabilitäten, Peeling und Ballooning Moden, erklärt werden können. Die Kopplung dieser Instabilitäten ist jedoch im Allgemeinen komplex und erfordert eine numerische Auswertung. Das EPED Framework, ein System zur numerischen Vorhersage der Plasmarand-Stabilität, basiert auf Modellprofilen für Temperatur und Dichte und bestimmt für diese die idealen Wachstumsraten. Dieses Framework findet ein stabiles Regime stark erhöhten Drucks, welches experimentell nur zugänglich ist, indem die Dichte des Plasmas variiert wird, den sogenannten Super H-Mode. In den letzten Jahren wurde ein unabhängiges Framework, IPED, entwickelt, welches auf den EPED Def-initionen für Dichte- und Temperaturprofilen basiert, jedoch die Wachstumsraten mit Hilfe eines anderen Stabilitätscodes bestimmt.

In dieser Arbeit wurde ein neues Verfahren zur Abschätzung der Flächen- und Vol-umenprofile in Flusskoordinaten entwickelt, um die Normierung von Druck- und Stromdichteprofilen in IPED zu verbessern. Zudem wurde das IPED Framework um ein kürzlich neu entstandenes Modell zur Berechnung der Randstromdichte erweitert. Die Randstabilität wurde mit der neuen Version von IPED über einen großen Bereich von Plasmaparametern bestimmt. Im Gegensatz zum EPED Framework beobachten wir, dass Instabilitäten mittlerer Modenzahlen den Zugang zum Super H Regime ver-hindern, wobei auch der Einfluss von verschiedenen Stabilitätskriterien und mod-ellspezifischen Details untersucht wurde. Andererseits beobachten wir eine ähnliche Struktur der Stabilitätsgrenze im EPED Parameterraum, dem Raum von Druck und Elektronendichte des Plasmarands (p-n Raum), wobei der Druck bei niedrigen Dichten von Peeling Instabilitäten und bei hohen Dichten von Ballooning Insta-bilitäten limitiert wird. Des Weiteren wurden dimensionslose Skalengesetze für den höchsten stabilen Druck des Plasmarands bestimmt, die den vorteilhaften Einfluss von hoher positiver Triangularität und hohem Sicherheitsfaktor am Rand auf die Plasmarand-Stabilität widerspiegeln. Um den erreichbaren Druck im Plasmarand zu optimieren, wird ein Betrieb mit hohem toroidalen Magnetfeld und hoher positiver Triangularität bei einer Dichte knapp unter der Dichte, bei welcher der Übergang von Peeling zu Ballooning Moden lokalisiert ist, vorgeschlagen. Zur Interpretation der numerischen Ergebnisse wurden vereinfachte analytische Transformationen zwis-chen p-n Raum und s-α Raum hergeleitet, wobei der erste einen natürlichen Raum zur Beschreibung von Peeling und Ballooning Stabilität darstellt. Die numerisch bestimmten p-n Stabilitäts-Diagramme stimmen gut mit den theoretisch vorherge-sagten und in den p-n Raum transformierten Stabilitäts-Diagrammen überein.

1 Magnetically confined nuclear fusion

Magnetically confined nuclear fusion is a promising approach for a future energy source emitting no greenhouse gases and producing hardly any long-lived radioactive waste. This concept is based on the energy production of the sun, where hydrogen fuses to helium mainly in the proton-proton reaction at high temperatures and densities. However, for possibly achievable reactor densities or pressures the proton-proton reaction is not self-sustained, i.e. the energy loss exceeds the produced fusion energy which heats the plasma. The criterion for a fusion reactor to be self-sustained is given by the "triple product" [1]:

$$n_e T \cdot \tau_E \geqslant \text{const.} \cdot T^2 / \overline{\sigma v} \equiv L \tag{1}$$

where $p_e = n_e T$ is the electron pressure, τ_E is the time scale at which the system loses its energy (the energy confinement time), $\overline{\sigma v}$ is the reaction rate, L is the ignition threshold, n_e is the electron density and T is the temperature, assumed to be equal for all particle species. Thus, the triple product is a condition for the product of energy confinement time and plasma pressure. The requirement on both of these quantities, L, is desired to be as small as possible in order to build an economic fusion reactor [2]. For this reason, fusion reactors aim to produce energy by the fusion of deuterium and tritium to helium, because this reaction, characterized by $\overline{\sigma v}(T)$, has a comparably low minimum of the triple product at $T \approx 15$ keV [2]. The deuterium-tritium ignition threshold, considering realistic density and temperature distributions across the plasma volume, is roughly given by $L \approx 5 \cdot 10^{21}$ keV s m^{-3}, which results in required energy confinement times of $\tau_E \approx 3.3$ s at typical reactor densities of $n_e \approx 10^{20}$ m^{-3} [1]. At temperatures of $T \sim 15$ keV the hydrogen atoms are fully ionized. This is utilized by magnetic confinement devices, which use strong magnetic fields to trap the ionized particles and generate the required pressures. There are two prevailing reactor designs following this concept, the Stellarator and the Tokamak, both sharing a toroidal field line topology.
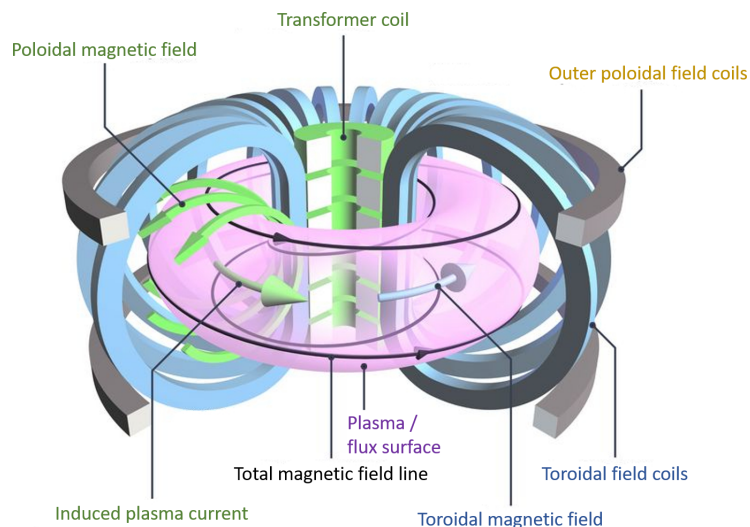

Figure 1: Basic structure of a Tokamak fusion reactor. Adapted from www.euro-fusion.org (Effective: 09.08.2020).

In this work, we focus on the toroidally symmetric Tokamak device, which is illustrated in figure 1. In a purely toroidal magnetic field, the Lorentz force would lead to a drift motion $\vec{v}_D \sim \vec{B} \times \vec{\nabla}|\vec{B}|/q$ of the charged particles due to the gradient and curvature of the magnetic field $\vec{B}$ [1]. This drift separates positive and negative charges q and therefore generates an electric field $\vec{E}$. Then, a secondary drift motion $\vec{v}_D \sim \vec{E} \times \vec{B}$ would occur which causes the particles to leave the plasma volume [1]. The superposition of a poloidal magnetic field neutralizes the initial drift motion. For this reason, the confining magnetic field of a Tokamak is a superposition of a toroidal magnetic field generated by the toroidal field coils and a poloidal magnetic field generated by the plasma current, which is induced by the transformer coil [1]. For this magnetic field configuration, one can define radially nested flux surfaces, i.e. surfaces that embed the magnetic field lines [1]. Such a flux surface is also displayed in figure 1. Finally, the outer poloidal field coils generate a vertical magnetic field used to position the plasma and shape its flux surfaces [1].

The toroidal magnetic field is usually strong enough that the mean free path of the particles perpendicular to the field lines is small compared to the system size. In contrast, the mean free path parallel to the field lines typically exceeds the system size by orders of magnitude. Thus, thermodynamic gradients can only be sustained between different flux surfaces [3]. Perpendicular to the flux surfaces, i.e. in minor radial direction, the thermodynamic gradients are determined by collisional and turbulent transport as well as sources and sinks, resulting in radially resolved thermodynamic profiles [1][3]. Usually, temperature and density have their maximum at the plasma center due to heat sources and inward particle transport, the "particle pinch", and monotonously decrease towards the last closed/confined flux surface (LCFS) [3].
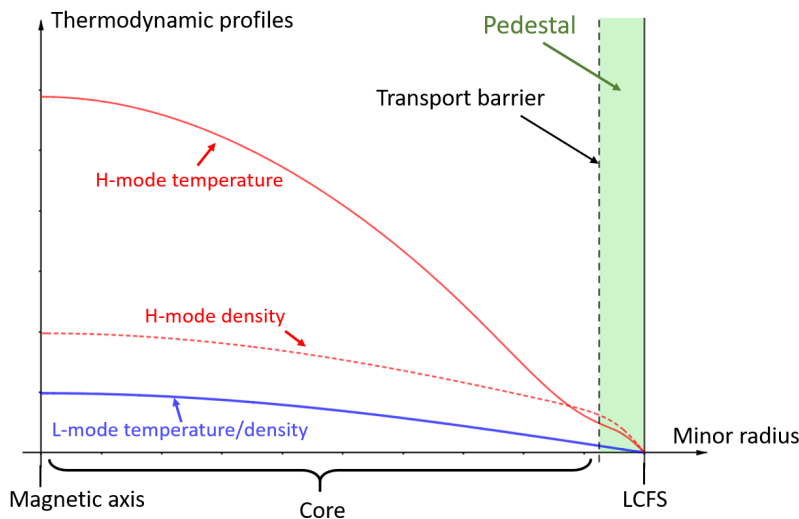
Figure 2: Thermodynamic profile structure for a L-mode (blue) and H-mode (red) plasma. The temperature profile obeys the stiffness relation $|\vec{\nabla}T|/T = $ const. . Based on [3][5].

Figure 2 (blue profile) shows the thermodynamic profile structure of a Tokamak plasma in low confinement mode (L-mode), where radial heat and particle transport is approximately uniform. The transport at the plasma edge is observed to be suppressed if exceeding a certain heating power threshold. Then, the plasma

transitions to a high confinement mode (H-mode), where a transport barrier near the LCFS builds up, resulting in steep thermodynamic gradients at the plasma edge [5][6]. During the transition from L-mode to H-mode, the temperature core gradient length $|\vec{\nabla}T|/T$ is typically preserved, which is known as profile stiffness, and the core profiles are lifted up as if they are on a growing pedestal [3][7]. For this reason, the edge region between the transport barrier and the LCFS is called the pedestal. Figure 2 (red profile) also outlines the typical thermodynamic profile structure for an H-mode plasma.

While the H-mode has significantly enhanced pressure, temperature and energy confinement, it also comes with a new type of major plasma instabilities called Edge Localized Modes (ELMs), which limit the possible pedestal height [5][6]. Large ELMs, more precisely Type I ELMs, strongly degrade the transport barrier and therefore lead to massive energy and particle loads on the vessel material which can cause severe damage in future fusion reactors [8]. On the contrary, ELMs usually clear the core plasma from impurities in present devices, which is advantageous as impurities dilute the hydrogen fuel and significantly increase radiation losses [1][5][9]. However, recent transport simulations predict that ELMs in ITER might lead to an increase in the impurity content of the core plasma [9]. Hence, for the operation of future reactors it is inevitable to understand the physics of ELMs.

The stability of the H-mode pedestal against type I ELMs, studied in this work, is well-described by the theory of ideal magnetohydrodynamics (MHD) [10]. From linearized ideal MHD, two classes of edge localized instabilities limiting the pedestal, namely high mode number peeling and (edge) ballooning modes, were theoretically derived and studied in detail previously [11][12]. However, the coupling of peeling and ballooning modes is still not completely understood. Furthermore, there are multiple stability codes that can numerically evaluate ideal MHD stability. A simple model creating thermodynamic profiles, called EPED, was developed in combination with a stability code, ELITE, to numerically study edge stability of H-mode plasmas [13][14]. The EPED-ELITE framework predicted an edge stability regime at significantly enhanced pedestal pressures that can only be experimentally accessed by varying the plasma density, the so-called Super H-mode [15]. Conversely, critically stable pedestal top pressures for negative triangularity scenarios are usually noticeably smaller compared to plasmas with positive triangularity, reducing the ELM energy content [16]. Recently, a different framework, IPED, combining EPED with the stability code MISHKA was developed by M. G. Dunne to achieve an independent analysis for the edge stability of H-mode plasmas [17][18].

In this thesis, the ideal MHD stability of H-mode Tokamak plasmas is studied for different operational scenarios, including negative triangularity, using an upgraded version of the predictive framework IPED. In particular, stability trends as well as the stability of separate mode numbers are analyzed in order to optimize the pedestal stability for ASDEX Upgrade (AUG). Furthermore, an attempt is made to reproduce the Super H solutions predicted in [15]. Firstly, the theoretical background of ideal MHD and the EPED and IPED frameworks is summarized in chapter 2. Then, the implementation details of the newly upgraded IPED code are described in chapter 3. Numerical results, including trends and scaling laws for pedestal stability, are presented in chapter 4. Finally, we interpret and discuss our findings in chapter 5.

2 Theoretical background

2.1 Ideal MHD

2.1.1 Stationary equilibrium

The theory of magnetohydrodynamics (MHD) describes the plasma as a combination of charged fluids. It is based on the fluid theory assumptions that there are sufficiently many particles in each fluid cell and that these particles are in thermodynamic equilibrium, i.e. that the mean free path length and the Larmor radius are much smaller than the system size. This allows, similar to conventional hydrodynamics, to describe the system in terms of the moments of the kinetic equation together with a closure assumption. While for a Tokamak plasma these assumptions usually hold perpendicular to the magnetic field, they are violated parallel to the magnetic field as the mean free path typically exceeds the system size. Thus, MHD is only a consistent description for dynamics perpendicular to the magnetic field. In addition, ideal MHD assumes that the plasma is ideally conducting, i.e. that the time scale of MHD events is much smaller than the time scale of resistive losses. The resulting one-fluid non-linear ideal MHD equations yield [4]:

$$\text{Continuity} \qquad \partial_t \rho + \vec{\nabla} \cdot (\rho \vec{v}) = 0 \tag{2}$$

$$\text{Force balance} \qquad \rho \left(\partial_t \vec{v} + \left(\vec{v} \cdot \vec{\nabla} \right) \vec{v} \right) = -\vec{\nabla} p + \vec{j} \times \vec{B} \tag{3}$$

$$\text{Ideal Ohm's law} \qquad \vec{E} + \vec{v} \times \vec{B} = 0 \tag{4}$$

combined with the Maxwell equations and a closure assumption

$$\text{Maxwell} \qquad \vec{\nabla} \cdot \vec{B} = \vec{\nabla} \cdot \vec{E} = 0 \ , \quad \partial_t \vec{B} = -\vec{\nabla} \times \vec{E} \ , \quad \mu_0 \vec{j} = \vec{\nabla} \times \vec{B} \tag{5}$$

$$\text{Adiabatic closure} \qquad \mathrm{d}_t \left(p \rho^{-\Gamma} \right) = 0 \quad \overset{(2)}{\Rightarrow} \quad \mathrm{d}_t p + p \Gamma (\vec{\nabla} \cdot \vec{v}) = 0 \tag{6}$$

where ρ is the mass density, $\vec{v}$ is the center-of-mass velocity, p is the isotropic pressure, $\vec{j}$ is the current density, $\vec{B}$ is the magnetic field, $\vec{E}$ is the electric field and Γ is the adiabatic index. In the following, we determine a stationary ideal MHD equilibrium for a Tokamak plasma and study its linear stability.

The geometry of an axisymmetric Tokamak plasma with nested flux-surfaces is displayed in figure 3, introducing the natural coordinate system. Using the Maxwell equations in toroidal symmetry and approximating $\left| \rho \left(\vec{v} \cdot \vec{\nabla} \right) \vec{v} \right| \ll \left| \vec{\nabla} p \right|$, the stationary force balance (equation 3) can be rewritten as [4]:

$$\boxed{F \cdot \mathrm{d}_{\widehat{\psi}} F + \mu_0 R^2 \cdot \mathrm{d}_{\widehat{\psi}} p = \mu_0 R j_{\text{tor}} = -\Delta^* \widehat{\psi}} \tag{7}$$

with

$$F(\widehat{\psi}) = R B_{\text{tor}} \quad \text{and} \quad \widehat{\psi}(R, Z) = \int_0^R B_Z(R, Z) R \, \mathrm{dR} - \int_0^{R_M} B_Z(R, Z_M) R \, \mathrm{dR} \tag{8}$$

where $\psi = 2\pi \widehat{\psi}$ is the poloidal flux (here defined with respect to the magnetic axis), B_{tor} is the toroidal magnetic field, j_{tor} is the toroidal current density and $\Delta^* \equiv R \partial_R (1/R \cdot \partial_R) + \partial_Z^2$ is the Stokes operator in cylindrical coordinates; the magnetic axis is located at (R_M, Z_M) and B_Z is the vertical component of the magnetic
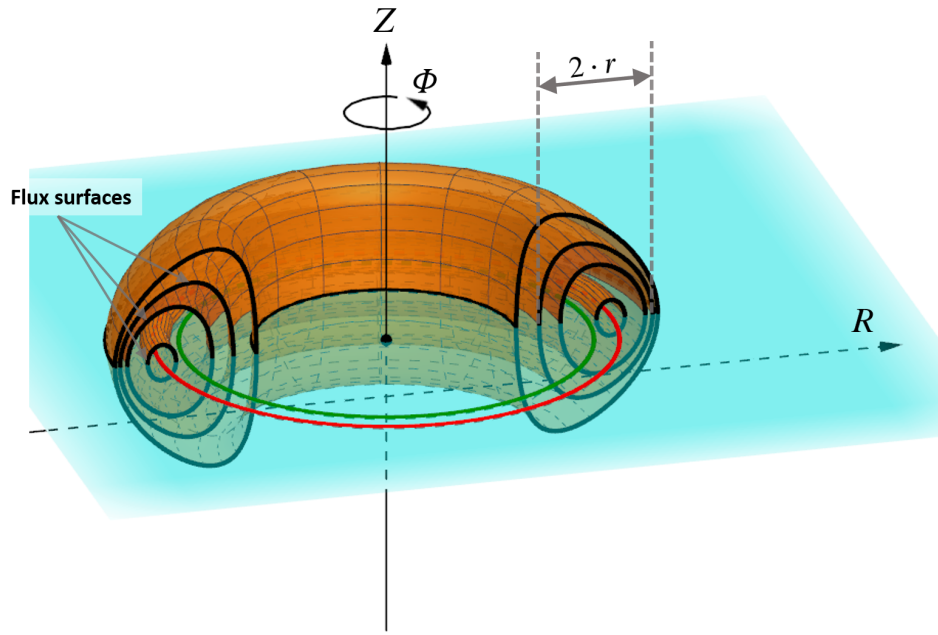
Figure 3: Geometry of an axisymmetric Tokamak plasma with nested flux surfaces. Global cylindrical coordinates (R, Φ, Z) and minor radius r of a flux surface. Blue: Midplane, Orange: Flux surfaces, Green: Center of the last closed flux surface, Red: Magnetic axis.

field. Equation 7 is known as the Grad-Shafranov equation. There are different numerical codes solving the Grad-Shafranov equation, one of them being HELENA, for a given pressure and current density profile as well as a plasma boundary $\mathcal{S}(R, Z)$ [19].

However, before continuing with the linear stability analysis of the obtained equilibrium, analytical investigations of equation 7 provide additional insights. For this reason, we introduce the minor radius r, the major radius or flux surface center R_0 and the vertical center Z_0 as

$$r = \frac{1}{2}\left(R^+ - R^-\right) \in [0, a] \,, \quad R_0 = \frac{1}{2}\left(R^+ + R^-\right) \,, \quad Z_0 = \frac{1}{2}\left(Z^+ + Z^-\right) \quad (9)$$

where $P_{\mathrm{FS}}^- = (R_{\mathrm{FS}}^-, Z_{\mathrm{FS}}^-)$ and $P_{\mathrm{FS}}^+ = (R_{\mathrm{FS}}^+, Z_{\mathrm{FS}}^+)$ are the radially innermost and outermost points for any flux surface FS, a is the minor radius of the last closed flux surface (LCFS) and the magnetic axis is defined to be at $R = R_M \equiv R_0(r = 0)$ and $Z = Z_M \equiv Z_0(r = 0)$ (compare to figure 3). In the following, we approximate that $Z_0(r) \approx Z_M$ for all flux-surfaces. Additionally, assuming circular flux surface cross-sections centered around $R_0(r) \equiv R_0(0)$, there would be a net force expanding the torus generated by both the larger pressure-driven force and the stronger magnetic field at the inner half of the torus. In equilibrium, this force is compensated by a strengthening of the magnetic field at the outer half of the torus due to an outward shift, i.e. a compression, of the flux-surfaces [4]. This shift is called the Shafranov shift $\Delta_s(r) \equiv R_0(r) - R_0(a)$. One can calculate that an external vertical magnetic field has to be applied in order to generate the Shafranov shift which balances the outward force [4]. Treating the shift as a small perturbation and for small inverse

aspect ratios $\epsilon = r/R_0(0) \ll 1$, the following differential equation can be derived [4]:

$$d_r \left(rB_{\mathrm{pol},0}^2 \cdot d_r \Delta_s \right) = \frac{r}{R_0(0)} \cdot \left(2\mu_0 r \cdot d_r p - B_{\mathrm{pol},0}^2 \right) \quad \mathrm{with} \quad \Delta_s(a) = 0 \qquad (10)$$

where $B_{\mathrm{pol},0}$ is the unperturbed poloidal magnetic field, i.e. the poloidal field for $R_0(r) \equiv R_0(0)$ and r is the radius of the (unperturbed) circular flux surfaces. This equation can be solved for a constant current density and quadratic pressure profile $p(r) \sim (1 - (r/a)^2)$:

$$\boxed{\Delta_s(r) = \Delta_{s,0} \cdot \left[1 - \left(\frac{r}{a} \right)^2 \right] \quad \mathrm{with} \quad \Delta_{s,0} = \left(\beta_{\mathrm{pol},0} + \frac{1}{4} \right) \cdot \frac{a^2}{2R_0(0)}} \qquad (11)$$

where $\beta_{\mathrm{pol},0}$ is the unperturbed poloidal beta. The estimate for the Shafranov shift given by equation 11 is used later to approximate the equilibrium flux surfaces in the IPED 2 framework.

2.1.2 Linear stability

The equilibrium obtained in the previous section obeys the force balance relation. However, it might be unstable with respect to small perturbations. For this reason, we linearize the MHD equations around the equilibrium solution. For a flow-free equilibrium, i.e. $\vec{v}_{\mathrm{eq.}} = 0$, one obtains [4]:

Force balance $\qquad \rho_0 \partial_t \vec{v}_1 = \frac{1}{\mu_0} \left((\vec{\nabla} \times \vec{B}_0) \times \vec{B}_1 + (\vec{\nabla} \times \vec{B}_1) \times \vec{B}_0 \right) - \vec{\nabla} p_1$ (12)

Ideal Ohm's law $\qquad \partial_t \vec{B}_1 = \vec{\nabla} \times (\vec{v}_1 \times \vec{B}_0)$ (13)

Adiabatic closure $\qquad \partial_t p_1 = -p_0 \Gamma (\vec{\nabla} \cdot \vec{v}_1) - (\vec{v}_1 \cdot \vec{\nabla}) p_0$ (14)

where we denote the equilibrium quantities with the index 0 and a small perturbation with the index 1. Introducing the perturbed quantity $\vec{\xi}$ with $\partial_t \vec{\xi} = \vec{v}_1$, we can integrate the linearized flow-free MHD equations and insert the integrated equations 13 and 14 into the linearized force balance [4]:

$$\boxed{\begin{array}{c} \rho_0 \partial_t^2 \vec{\xi} = \frac{1}{\mu_0} \left((\vec{\nabla} \times \vec{B}_0) \times \vec{B}_1 + (\vec{\nabla} \times \vec{B}_1) \times \vec{B}_0 \right) + \vec{\nabla} \left(p_0 \Gamma \vec{\nabla} \cdot \vec{\xi} + \vec{\xi} \cdot \vec{\nabla} p_0 \right) \\ \\ \mathrm{with} \ \vec{B}_1 = \vec{\nabla} \times (\vec{\xi} \times \vec{B}_0) \end{array}} \qquad (15)$$

where we set the integration bounds without loss of generality to

$$\vec{\xi}_1(\vec{x}, t=0) = \vec{B}_1(\vec{x}, t=0) = \rho_1(\vec{x}, t=0) = p_1(\vec{x}, t=0) = 0 \ , \quad \vec{v}_1(\vec{x}, t=0) \neq 0 \ .$$

Using an exponential Ansatz $\vec{\xi}(\vec{x}, t) = e^{-i\omega t} \vec{\xi}_{\mathrm{sp}}(\vec{x})$, where $\vec{\xi}_{\mathrm{sp}}$ is the spatial part of $\vec{\xi}$, this equation simplifies to a standard complex eigenvalue problem of the form

$$-\omega^2 \rho_0 \vec{\xi} = \mathcal{F} \vec{\xi} \quad \mathrm{with} \quad \omega^2 \in \mathbb{R} \qquad (16)$$

where $\mathcal{F}$ is the hermitian MHD force operator [4]. There are multiple numerical codes, one of them being MISHKA, that can solve this eigenvalue problem using a Fourier decomposition of the form $\vec{\xi}_{\mathrm{sp}}(\vec{x}) \sim e^{i\Phi n}$, which allows a growth rate ω and structure of the perturbation for every toroidal mode number n independently [18].

Moreover, equation 16 can be used to derive a variational formalism that grants analytical insight into linear MHD stability without calculating the detailed eigenvalues and eigenfunctions [4]:

$$\delta W(\vec{\xi}^*, \vec{\xi}) \equiv -\frac{1}{2} \int \vec{\xi}^* \cdot \mathcal{F}\vec{\xi} \; \mathrm{dV} = \frac{\omega^2}{2} \int \rho_0 |\vec{\xi}|^2 \; \mathrm{dV} \equiv \omega^2 K(\vec{\xi}^*, \vec{\xi})$$

$$\overset{K(\vec{\xi}^*, \vec{\xi}) \neq 0}{\Leftrightarrow} \omega^2 = \frac{\delta W(\vec{\xi}^*, \vec{\xi})}{K(\vec{\xi}^*, \vec{\xi})} \tag{17}$$

where a star denotes complex conjugation, $\delta W(\vec{\xi}^*, \vec{\xi})$ is the work done by the displacement $\vec{\xi}$ and $K(\vec{\xi}^*, \vec{\xi})$ is related to the kinetic energy of the perturbation. This equation is valid even if ω is not an eigenvalue of equation 16. However, following the variational principle of Ritz, the most negative eigenvalue ω is prescribed by minimizing the right-hand-side of equation 17, which is equivalent to minimizing $\delta W(\vec{\xi}^*, \vec{\xi})$ for an arbitrary normalization condition $|\vec{\xi}| = \mathrm{const.}$ [4][20]. Then, the system is stable if the $\underline{\delta W} > 0$ and unstable if $\underline{\delta W} < 0$, where $\underline{\delta W}$ refers to the minimized work functional. With this variational principle, which is called the energy principle, stability can be studied in the context of reasonable test functions $\vec{\xi}$, which may represent different classes of instabilities. Consequently, when restricting stability analysis to a certain set of test functions, the minimized work functional only describes stability with respect to the chosen set of perturbations. In this case, the obtained minimized frequency $\underline{\omega}$ is an upper bound to the most negative eigenvalue, meaning that there might be unconsidered classes of instabilities that destabilize the system.

For a magnetically confined fusion plasma where the plasma volume is surrounded by a vacuum region enclosed by a perfectly conducting wall, an explicit form of the work functional can be calculated using appropriate boundary conditions [4]:

$$\delta W = \delta W_F + \delta W_S + \delta W_V \tag{18}$$

with

$$\delta W_V = \frac{1}{2} \int_{\mathrm{Vacuum}} \frac{|\vec{B}_1|^2}{2\mu_0} \; \mathrm{dV} \tag{19}$$

$$\delta W_S = \frac{1}{2} \int_{\mathrm{Surface}} |\vec{n} \cdot \vec{\xi}_\perp|^2 \; \vec{n} \cdot \left\{ \vec{\nabla}\left(p_0 + \frac{|\vec{B}_0|^2}{2\mu_0} \right) \right\}_{\mathrm{jump}} \; \mathrm{d}\sigma \tag{20}$$

$$\delta W_F = \frac{1}{2} \int_{\mathrm{Fluid}} \left[\frac{|\vec{B}_{1,\perp}|^2}{2\mu_0} + \left(\frac{|\vec{B}_{0,\perp}|^2}{2\mu_0} \left| \vec{\nabla} \cdot \vec{\xi}_\perp + 2\vec{\xi}_\perp \cdot \vec{\kappa} \right|^2 \right) + \Gamma p_0 |\vec{\nabla} \cdot \vec{\xi}|^2 - \right.$$
$$\left. -2(\vec{\xi}_\perp \cdot \vec{\nabla} p_0)(\vec{\kappa} \cdot \vec{\xi}_\perp^*) - \frac{j_{0,\parallel}}{|\vec{B}_0|} (\vec{\xi}_\perp^* \times \vec{B}_0) \cdot \vec{B}_1 \right] \; \mathrm{dV} \tag{21}$$

where δW_V is the vacuum contribution, δW_S is the contribution from the plasma-vacuum interface, δW_F is the fluid/plasma contribution, $\{\dots\}_{\mathrm{jump}}$ refers to the jump of the enclosed quantities across the surface, $\vec{n}$ is the surface-normal vector, $\vec{\kappa} = \vec{b} \cdot \vec{\nabla}\vec{b}$ with $\vec{b} = \vec{B}_0/|\vec{B}_0|$ is the curvature vector and the indices $\perp$ and $\parallel$ denote the vector components perpendicular and parallel to $\vec{B}_0$.

Studying the different contributions, the first three terms of δW_F can be associated with energy of shear Alfvén waves, compressional Alfvén waves and sound waves, respectively, and are always positive and thus stabilizing [4]. Therefore, the destabilizing contributions of δW_F are given by the fourth and fifth term, representing pressure-gradient driven and current-density driven instabilities, respectively [4]. Because the contribution $-(\vec{\xi}_\perp \cdot \vec{\nabla} p_0)(\vec{\kappa} \cdot \vec{\xi}_\perp)$ is negative if $\vec{\nabla} p_0$ and $\vec{\kappa}$ are parallel and positive if they are anti-parallel, the curvature of the magnetic field is destabilizing at the outer half and stabilizing at the inner half of the torus [4]. Hence, we term the curvature "unfavorable" on the outer half of the torus and "favorable" on the inner half. The overall contribution of the pressure-gradient crucially depends on the average curvature along a field line [4]. Next, the vacuum part δW_V is generally positive and therefore always stabilizing. While the plasma-vacuum interface term δW_S is more complex, it does not contribute to the work functional if displacements leave the surface unchanged $\vec{n} \cdot \vec{\xi}_\perp = 0$ or if there is no jump in the pressure gradient $\vec{\nabla}\left(p_0 + |\vec{B}_0|^2/(2\mu_0)\right)$ [20]. To make further analytical progress, the contributions of the vacuum and the plasma surface can be ignored in the context of minimization, if we are only interested in modes that are localized inside the plasma edge, and we set $\delta W \equiv \delta W_F$ [20][11]. However, numerical codes are able to solve the full eigenproblem (equation 16) and calculate the complete work functional (equation 18).

2.1.3   Edge Localized Modes

As previously mentioned, a new type of instability located at the plasma edge (pedestal region), called Edge Localized Modes (ELMs), occurs if Tokamak plasmas transition to the high confinement state (H-mode). Since ELMs cause massive bursts of lost particles and energy ($\sim 5 - 10\%$ of the total content in $\leqslant 1$ms), it is crucial for larger fusion reactors to suppress or mitigate them in order to prevent damage to the plasma vessel [8][10].

Historically, ELMs can be classified into three different types; here, we exclude so-called dithering cycles that may be interpreted as repeated transitions between low and high confinement mode. Type III ELMs occur at heating powers close to the H-mode transition power $P_{L \to H}$ and are possibly described by coupled resistive MHD instabilities [10]. Consistently, as the edge temperature rises and resistive effects are suppressed, the type III ELM frequency decreases until this ELM type completely vanishes. At higher edge temperatures, i.e. for large H-mode pedestals, type I ELMs emerge and typically limit the pedestal height [10]. These ELMs are proposed to be caused by coupled ideal MHD instabilities. This is consistent with the observation that the type I ELM frequency increases with separatrix heating power, since the build up of the edge gradients up to a critical value is accelerated. A common model for this ELM-type is given by the peeling-ballooning theory, which describes the occurrence of type I ELMs by the coupling of ideal peeling and ballooning modes [10]. Thus, in the regime of sufficiently high edge temperatures, pedestal stability can be studied using ideal MHD and especially the peeling-ballooning theory. Finally, for completeness, type II ELMs are observed in strongly shaped plasmas, being more frequent and less severe compared to type I ELMs. [10].

Based on the variational formalism introduced in the previous section, peeling and ballooning instabilities can be analytically analyzed. We will first focus on the high

toroidal mode number (high-n) limit $n \to \infty$. In this limit, the work functional $\delta W = \delta W_F$ can be simplified for modes with a resonant surface $q(\psi) = m/n$ close to the plasma boundary, the so-called peeling modes, and minimization yields the peeling inequality [12]:

$$\sqrt{1 - 4D_M} > 1 + \frac{1}{\pi \partial_\psi q} \oint \frac{j_\parallel B}{B_{\mathrm{pol}}^3 R^2} \, \mathrm{dl} \quad \Leftrightarrow \quad \text{Stability} \tag{22}$$

where $\oint \ldots \, \mathrm{dl}$ denotes integration along the flux-surface in the (R, Z)-plane, q is the safety factor and D_M is the Mercier index, which can be interpreted as a measure of how favorable the field line curvature averaged along a field line is. In the case of weak shaping and small inverse aspect ratio $\epsilon \equiv r/R_0 \ll 1$ the Mercier index can be written as $D_M = (q^{-2} - 1)\epsilon \alpha s^{-2}$, where we define the normalized magnetic shear as $s \equiv (r/q) \cdot \partial_r q$ and the normalized pressure gradient as $\alpha = (2\mu_0 R_0)/B^2 \cdot q^2 \partial_r p$ [12]. Both the integral in equation 22 and the Mercier index are strongly dependent on shaping and aspect ratio. Thus, the effect of shaping on high-n peeling stability has to be analyzed carefully. While the peeling inequality is usually evaluated numerically, a simple relation for stability can be derived for small inverse aspect ratio and circular flux surfaces (see [12]):

$$(1 - q^{-2})\epsilon \cdot \frac{\alpha}{s^2} > \frac{1}{4\pi \partial_\psi q} \oint \frac{j_\parallel B}{B_{\mathrm{pol}}^3 R^2} \, \mathrm{dl} = \frac{\partial_\psi V}{4\pi \partial_\psi q} \left\langle \frac{j_\parallel B}{B_{\mathrm{pol}}^2 R^2} \right\rangle_V \underset{\uparrow}{\approx} \pi \frac{2 - s}{s} \tag{23}$$

with the simple equilibrium relation $\boxed{s = 2 - 2j_\parallel \cdot A(r = a)/I_P}$

$$\Rightarrow \text{ Marginal stability for:} \quad \alpha = \pi \frac{(2 - s)s}{(1 - q^{-2})\epsilon} \tag{24}$$

where I_P is the total plasma current, $A(r)$ is the area enclosed by a flux-surface and $\langle \ldots \rangle_V$ denotes the standard "flux-surface average", which is equivalent to the volume-average with respect to the volume $V(r)$ enclosed by a flux-surface; the precise definitions of A, V and $\langle \ldots \rangle_V$ are given in the appendix B.1 "Averages". One has to be careful, since equation 23 is only consistent if $|2 - s| \ll 1$, i.e. if assuming that the right hand side is a small quantity; this is the "small current density"-"small pressure gradient" limit. Finally, an example stability boundary for high-n peeling modes is displayed in figure 5 (page 11).

Furthermore, we discuss localized modes where multiple poloidal mode numbers from adjacent resonant surfaces couple at a single flux surface so that their amplitude is maximized in the region of unfavorable curvature [4][12]. These modes are called ballooning modes and the poloidal structure of such a mode is shown in figure 4a. While radial localization seems contradictory to poloidal mode number coupling, radial localization $\Delta r \approx \frac{\Delta m}{n \partial_r q}$ can still be satisfied for $\Delta m > 0$ in the high-n limit [4]. As for the peeling modes, the work functional is minimized using the Euler-Lagrange method. While there is no simple stability inequality, the equation for marginal stability can be simplified in the limit of large aspect ratio, circular flux surfaces and vanishing Shafranov shift [4]:

$$\mathrm{d}_\theta \left((1 + h^2) \mathrm{d}_\theta \hat{X} \right) + \alpha (h \cdot \sin \theta + \cos \theta) \cdot \hat{X} = 0 \text{ with } h \equiv s\theta - \alpha \sin \theta \tag{25}$$

where $\theta \in [-\infty, \infty]$ is the ballooning angle, generalizing the poloidal angle, and $\hat{X}$ represents the radial displacement. The solution of equation 25 as well as a modification including the effect of finite Shafranov shift are displayed in figure 4b. One can
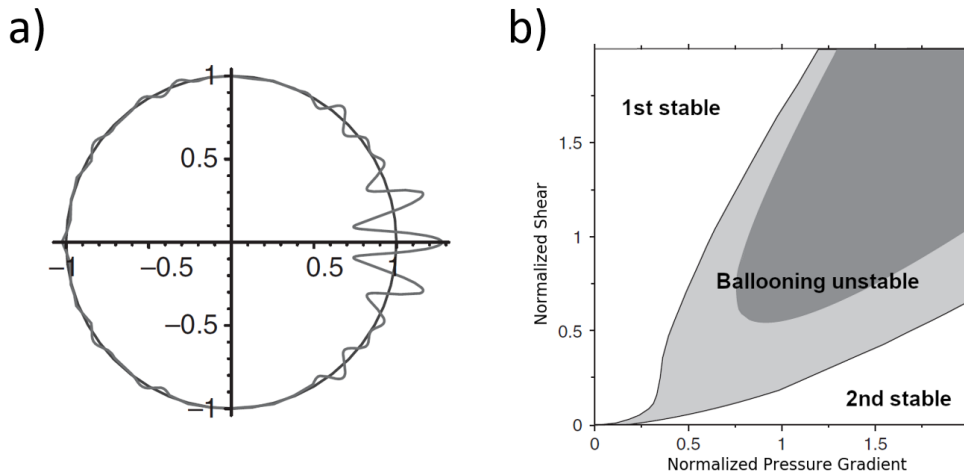
a)

b)

Figure 4: a) Structure of a ballooning mode with $m = 20$ to 30 (from [4]). b) Ballooning stability border for a large aspect ratio Tokamak with circular flux surfaces; the darker shaded region indicates ballooning instability if including the effect of the Shafranov shift (from [4], Author: H.-P. Zehrfeld, IPP).

see that there are two stable regions in the $s - \alpha$ diagram, which are disconnected for vanishing Shafranov shift. While, for fixed shear, the pressure gradient is limited in first-stable regime, there is no such limitation in the second-stable regime. This strange second stability regime might be explained by the stabilizing effect of the pressure gradient through the effective local shear h, similar to the "magnetic well" due to shaping [4]. The first and second stable regimes get connected if one considers finite Shafranov shift and the connection zone even increases when elongating the plasma cross-section [4]. Figure 5 (page 11) also displays a typical high-n ballooning boundary.

Finally, the coupling of finite-n ballooning and peeling modes was studied by Hegna and others, who developed a theoretical framework expressing the mode structure by a discrete set of poloidal harmonics. Assuming peeling modes with their rational surface being outside the plasma (but close to the plasma surface), the work functional for coupled modes δW_{PB} can be expressed to zeroth-order as [21]:

$$\delta W_{PB} \cong \delta W_P - \frac{I_0^2}{4\delta W_B} \quad \text{or} \quad \delta W_{PB} \cong \delta W_B - \frac{I_0^2}{4\delta W_P} \tag{26}$$

where the coupling/interaction integral I_0 acts generally destabilizing, $\delta W_P > 0$ is the peeling mode energy, $\delta W_B > 0$ is the ballooning mode energy and " $\cong$ " denotes that two expressions describe congruent stability diagrams. Therefore, coupled modes can be destabilized if both the pure peeling and pure ballooning work functional are small, which is close to the pure peeling and pure ballooning stability boundary [21]. If either $\delta W_P < 0$ or $\delta W_B < 0$, the system is pure peeling or ballooning unstable. The interaction integral usually has to be evaluated numerically. However, a strongly simplified analytical expression was derived for weak shaping and constant current density inside the edge region [21]:

$$I_0 = -\frac{\alpha}{s^2}(1 + s)\exp(-1/s)\ln(\Delta) \quad \text{with} \quad \Delta = M + 1 - n \cdot q|_{r=a} \ll 1 \tag{27}$$

where M is the number of resonant surfaces inside the plasma. Under the applied simplifications, the peeling energy scales as $\delta W_P \sim \Delta^{-1}$ [21]. Therefore, the peeling

energy term diverges stronger than the interaction integral as $\Delta \to 0$, meaning that coupling will be only important if δW_B is sufficiently small, i.e. close to the ballooning boundary [21]. Moreover, one can show that the coupling is maximized for modes with $\Delta = \exp(-2)$. For smaller values of Δ, the peeling mode energy becomes increasingly dominant [21]. The coupled peeling-ballooning modes are also displayed in figure 5, which summarizes the previous results.
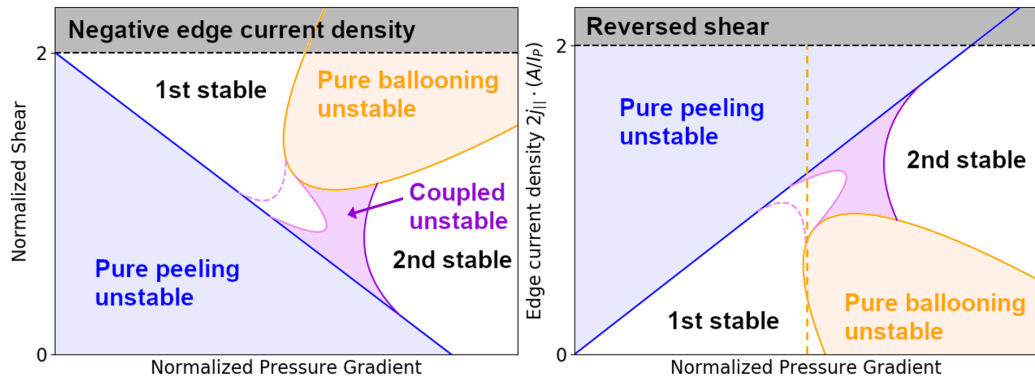

Figure 5: Sketch of the stability borders for pure high-n ballooning (orange) and peeling (blue) modes as well as lines to guide the eye for coupled peeling-ballooning stability borders (violet). Left: s-α space, based on [22], Right: j-α space using the transformation $s = 2 - 2j_{\parallel} \cdot A(r = a)/I_P$ (equation 23). The different shading of the coupled stability borders is to distinguish them. The violet dashed line is an artificially modified version of the coupled stability border, representing stronger coupling. The orange dashed line roughly approximates the ballooning boundary in the 1st stable regime for comparison with common j-α stability diagrams (see [12]).

From the above discussion, the dimensionless quantities s and α seem to be a natural choice for edge stability diagrams. However, their definitions given above are related to plasmas with circular cross-section. We define a more generalized definition for the normalized shear and the normalized pressure gradient for shaped plasmas following Miller and others [23]:

$$s \equiv \frac{2V}{q} \cdot \frac{\partial_\psi q}{\partial_\psi V} , \qquad \alpha \equiv -\mu_0 \frac{\partial_\psi V}{2\pi^2} \sqrt{\frac{V}{2\pi^2 R_0}} \cdot \partial_\psi p \tag{28}$$

2.2 Diamagnetic stabilization

In the ideal MHD model, any phenomena related to the finite Larmor radius (FLR) or the distinct gyro-motion of the different particle species (ions and electrons) were neglected [4][24]. While this assumption is usually fulfilled for MHD events with sufficiently long wavelength, FLR effects become important as the wavelength λ_{MHD} gets comparable to the ion Larmor radius $r_{L,i}$, i.e. $\lambda_{\mathrm{MHD}} \lesssim r_{L,i}$ [25][26]. The study of high-n MHD modes may be extended by kinetic corrections that treat the effect of FLR [25][26]. This results in a modified stability criterion [25][27]:

$$\gamma_{\mathrm{MHD}} < \frac{1}{2} \cdot \omega_{*,i} \quad \Leftrightarrow \quad \text{Stable} \tag{29}$$

with the ion diamagnetic drift frequency (DDF)

$$\omega_{*,i} = \frac{n}{Zen_i} \cdot \partial_\psi p_i \tag{30}$$

where $\gamma_{\mathrm{MHD}} = -i\omega$ is the ideal MHD growth rate, $\omega^2 < 0$ is an eigenvalue of equation 16, n is the toroidal mode number, Z is the ion charge number, n_i is the ion density and p_i is the ion pressure. Thus, modes that grow slowly compared to the ion DDF are suppressed. Because equation 29 is a local stability criterion and the ion DDF is in general not constant over the edge region, this criterion has either to be implemented directly in the numerical stability code as local stabilization mechanism or the variation of $\omega_{*,i}$ over the pedestal has to be treated effectively [27][28]. We follow the effective treatment of the ion DDF as described in [28]:

$$\omega_{*,i}^{\mathrm{eff1}} = 0.5 \cdot \omega_{*,i}^{\max} \tag{31}$$

$$\omega_{*,i}^{\mathrm{eff2}} = \begin{cases} 0.75 \cdot \omega_{*,i}^{\max} & \text{for } nq_{95} \leqslant 27.7 \\[2ex] \omega_{*,i}^{\mathrm{eff2}}\Big|_{nq_{95}=27.7} + 0.12 \cdot (\omega_{*,i}^{\max} - \omega_{*,i}^{\mathrm{eff2}}\Big|_{nq_{95}=27.7}) & \text{for } nq_{95} > 27.7 \end{cases} \tag{32}$$

where the dependence of the effective ion DDFs $\omega_{*,i}^{\mathrm{eff1}}$ and $\omega_{*,i}^{\mathrm{eff2}}$ on the poloidal mode number nq_{95} is displayed in figure 6, q_{95} is the safety factor at $\psi = 0.95 \cdot \psi(r = a)$ and $\omega_{*,i}^{\max} = \max(\omega_{*,i})$ is evaluated at the peak position of $\partial_\psi p_i$ in the pedestal. In order to obtain these effective DDFs, growth rates γ_{2F} calculated by the two-fluid code BOUT++ were compared to ideal growth rates γ_{MHD} [28][29]. Then, based on the eigenvalue relation $\omega \cdot (\omega - \omega_{*,i}) + \gamma_{\mathrm{MHD}}^2 = 0$, the effective diamagnetic drift frequency is defined as $\omega_{*,i}^{\mathrm{eff}} = 2\sqrt{\gamma_{\mathrm{MHD}}^2 - \gamma_{2F}^2}$ [28]. Subsequently, the effective DDFs $\omega_{*,i}^{\mathrm{eff1}}$ and $\omega_{*,i}^{\mathrm{eff2}}$ were obtained by a rough approximation and a bi-linear fit, respectively, of the effective DDFs $\omega_{*,i}^{\mathrm{eff}}$ from the BOUT++ simulations [28]. The newly introduced effective ion DDFs replace $\omega_{*,i}$ in equation 29 to include the effect of $\omega_{*,i}$ not being constant over the pedestal region.
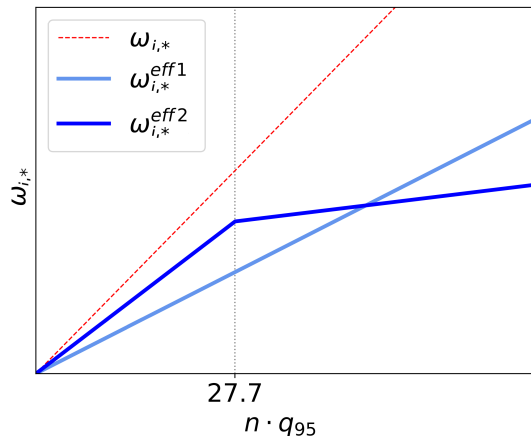

Figure 6: Dependence of the effective DDFs $\omega_{*,i}^{\mathrm{eff1}}$ and $\omega_{*,i}^{\mathrm{eff2}}$ on nq_{95} relative to $\omega_{*,i}$ as introduced in [28] based on a fit to BOUT++ simulations. As $\omega_{*,i} \sim n$ the ion DDF is a straight line.

To summarize, we introduced an effective diamagnetic stabilization mechanism for high toroidal mode numbers $n \gg 1$ modifying the ideal MHD growth rates. While the normalized ideal growth rates $\gamma_{\mathrm{MHD}} \cdot \tau_A$ are density independent, the normalized diamagnetic stability criterion $\omega_{*,i} \cdot \tau_A \sim 1/\sqrt{n_i}$ depends explicitly on density, where normalization is with respect to the Alfvén time $\tau_A \sim \sqrt{n_i}$, which will be important later.

2.3 Bootstrap current

From the previous sections we know that the ideal MHD equilibrium and its stability properties in Tokamak geometry are determined by a current density profile, a pressure profile and a plasma boundary. Consequently, for the study of instabilities localized at the pedestal, a good model for these quantities, especially at the plasma edge, is needed. Without additional external current drives, the area-averaged current density in the pedestal consists of two contributions, the Ohmic current and the bootstrap current [1]. The former is driven by the transformer coil and determined by the generated electric field and the electrical conductivity of the plasma, while the latter is driven by the thermodynamic gradients. The order of the edge Ohmic current can be estimated to $j_{\mathrm{Ohm}} \sim 1 \cdot 10^5 \, \frac{\mathrm{A}}{\mathrm{m}^2}$, where we assumed $T \approx 1$ keV, $R_0 \approx 1.5$ m, $a \approx 0.5$ m and a loop voltage of $U_{\mathrm{loop}} \approx 0.1$ V (see [1]). This is typically around one order of magnitude smaller than the edge bootstrap current. In the following, the processes generating the bootstrap current are discussed.

Because the magnetic field of a Tokamak $B \approx B_{\mathrm{tor}} \sim 1/R$ is radially decreasing, charged particles which have sufficiently low parallel velocity are trapped in the outer region of the Tokamak, since they are mirrored towards the low field side (LFS) at a certain critical radius R_{crit} [1]. Considering conservation of the magnetic moment, which is generated by the gyro-motion of the charges, and the kinetic energy for the movement along a magnetic field line, one can derive the trapping condition [30]:

$$\frac{v_\parallel}{v_\perp} \leqslant \sqrt{\frac{B_{\mathrm{max}}}{B_{\mathrm{min}}} - 1} = \sqrt{\frac{1 + \varepsilon}{1 - \varepsilon} - 1} \tag{33}$$
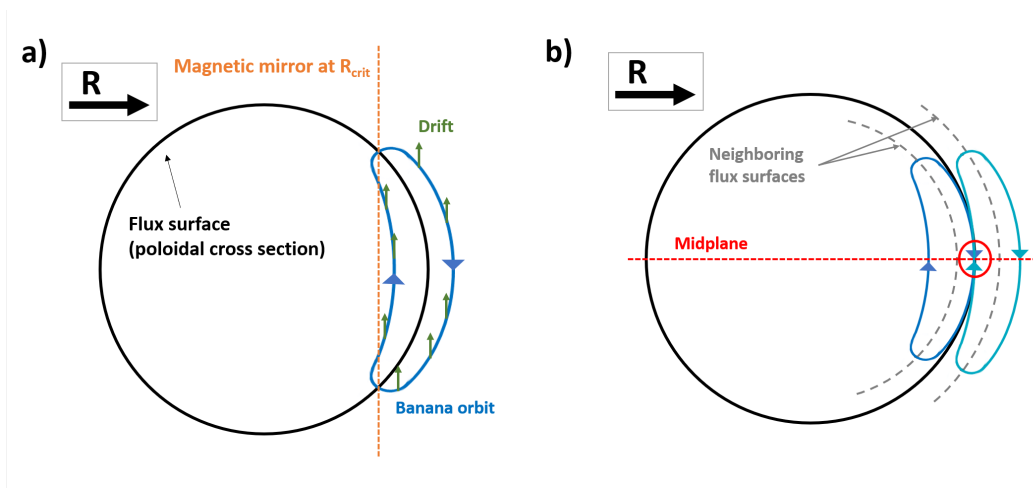

Figure 7: a) Trajectory / banana orbit (blue) of a charged particle. The particle is mirrored if the magnetic field $B \sim 1/R$ exceeds a critical value at a certain major radius R_{crit} (orange). The gradient and curvature drift (green) deflects the particle from its native flux surface (black), resulting in the banana motion. This is a projection to the (R, Z)-plane; the non-projected trajectories are mainly in the toroidal direction, because the particle motion is centered around the field lines $\vec{B} \approx \vec{B}_{\mathrm{tor}}$. The direction of the blue and green arrows is opposite for ions and electrons. b) Flux of trapped particles though the midplane at a certain flux surface (black) driven by banana orbits from neighboring flux surfaces (gray).

In addition to the reflection of trapped particles if the magnetic field exceeds a certain strength, the gradient and curvature drift $\vec{v}_D \sim \vec{B} \times \vec{\nabla}|\vec{B}|/q$, mentioned

in chapter 1, leads to a deflection of the particle trajectory from its native flux surface as displayed in figure 7a, resulting in so-called banana orbits [30]. Figure 7b shows two banana orbits that are centered at different flux surfaces but traverse the midplane in opposite directions at the same flux surface. Consequently, the flux of trapped particles though the midplane at a certain flux surface is determined by neighboring banana orbits [30]. This gives rise to the so-called banana current $j_B \sim d_r(n_e + n_i)$ if the banana orbits are differently populated, with contributions from both the electron density gradient $d_r n_e$ and the ion density gradient $d_r n_i$; here we also used the fact that the banana motion for ions and electrons is in the opposite direction. Note that a temperature gradient can also drive the banana current, as in this case the particle velocities of the distinct orbits differ [30].
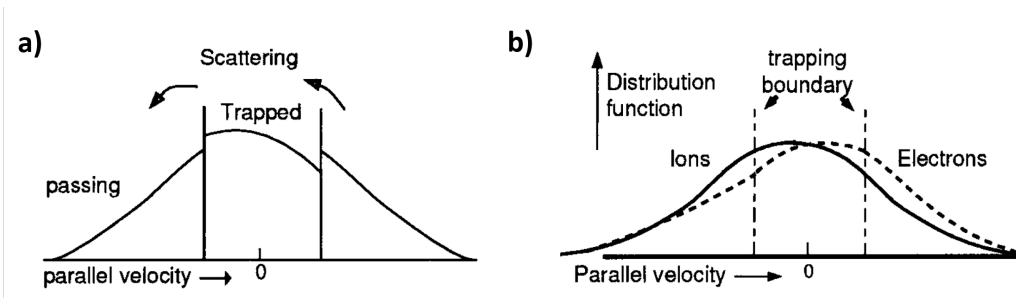

Figure 8: a) Parallel velocity distribution after modification by by trapped particles from neighboring flux surfaces, implying a discontinuity. b) Parallel velocity distribution smoothed by collisions/scattering.

Because the trapped particles visit neighboring flux surfaces as they follow the banana trajectory, the velocity distribution at a certain flux surface is influenced by the trapped particles of neighboring flux surfaces as shown in figure 8a [30]. Finally, collisions transfer momentum between trapped and passing particles, which removes the discontinuity in the velocity distribution. This results in a smooth but shifted velocity distribution, which is sketched in figure 8b [30]. The difference in the velocity distributions of electrons and ions (both passing and trapped particles) gives then rise to the bootstrap current [30]. For arbitrary magnetic equilibria and collisionalities, the averaged parallel current density, including both the Ohmic and the bootstrap current, can be expressed as [31]:

$$\langle j_\parallel \rangle_B = \sigma_{\text{neo}} \langle E_\parallel \rangle_B - \frac{F(\psi)}{B_T} \left[\mathcal{L}_{31} p \partial_\psi \ln p + \mathcal{L}_{32} p_e \partial_\psi \ln T_e + \mathcal{L}_{34} \tilde{\alpha} p_i \partial_\psi \ln T_i \right] \quad (34)$$

where σ_{neo} is the neoclassical conductivity, $E_\parallel$ is the parallel component of the applied electric field with respect to $\vec{B}$, $F(\psi)$ is defined as in equation 7 (page 4) and T_e and T_i are the electron and ion temperatures; the average is defined as $\langle \ldots \rangle_B \equiv \langle \ldots \cdot B \rangle_V / B_T$ with the toroidal magnetic field at the magnetic axis B_T and the coefficients $\mathcal{L}_{31}$, $\mathcal{L}_{32}$, $\mathcal{L}_{34}$ and $\tilde{\alpha}$ depend on the effective electron and ion collision frequencies as well as on the fraction of trapped particles. The bootstrap current as given by equation 34 contains contributions from the temperature and pressure gradients, as phenomenologically argued above. Moreover, using $p = nT$, the pressure gradients can be transformed to density gradient distributions as well. Then, comparing typical values of the bootstrap coefficients, one finds that density gradients are usually more efficient in driving the bootstrap current compared to temperature gradients [31].

2.3.1 Sauter model

In general, a complex set of transport equations has to be solved in order to obtain precise values for the neoclassical bootstrap transport coefficients. However, O. Sauter, C. Angioni and Y. R. Lin-Liu derived a simple set of fit formulas for these coefficients as well as for the neoclassical conductivity by fitting the numerical results computed by a Fokker–Planck solver, namely CQLP and CQL3D [31][32][33][34]. The resulting formulas, which fitted the numerical values of CQLP/CQL3D with an uncertainty of $\lesssim 5\%$ over a wide range of collision frequencies and magnetic equilibria, are summarized in the appendix A.1, with the trapped fraction f_t, effective charge Z_{eff} and collisionalities $\nu_{e,*}$ and $\nu_{i,*}$ defined as [31][32][35]:

$$f_t = 1 - \frac{3}{4} \left\langle B^2 \right\rangle_V \int_0^{1/B_{\max}} \frac{\lambda}{\left\langle \sqrt{1 - \lambda B} \right\rangle_V} \, \mathrm{d}\lambda \quad , \quad Z_{\text{eff}} = \frac{\sum Z_\alpha^2 n_\alpha}{\sum Z_\alpha n_\alpha} \tag{35}$$

$$\nu_{e,*} = 6.921 \cdot 10^{-18} \frac{q R_0 n_e Z_{\text{eff}} \ln(\Lambda_e)}{T_e^2 \varepsilon^{1.5}} \quad , \quad \nu_{i,*} = 4.90 \cdot 10^{-18} \frac{q R_0 n_i Z_{\text{main}}^4 \ln(\Lambda_{ii})}{T_i^2 \varepsilon^{1.5}} \tag{36}$$

where $B_{\max}$ is the largest value of the magnetic field for any flux surface, the sum $\sum$ is over all charge states of all ion species with Z_α their respective charge number and n_α their respective density, Z_{main} is the main ion charge number and the Coulomb logarithms are

$$\ln(\Lambda_e) = 31.3 - \ln\left(\frac{\sqrt{n_e[\mathrm{m}^{-3}]}}{T_e[\mathrm{eV}]}\right) \quad , \quad \ln(\Lambda_{ii}) = 30 - \ln\left(\frac{Z_i^3 \sqrt{n_i[\mathrm{m}^{-3}]}}{(T_i[\mathrm{eV}])^{1.5}}\right) . \tag{37}$$

Furthermore, O. Sauter derived an approximation for the trapped fraction as defined in equation 35, providing an analytical expression which includes the effect of triangularity [36]:

$$f_t = \min\left\{1; \quad 1 - \sqrt{\frac{1-\varepsilon}{1+\varepsilon}} \frac{1 - \varepsilon_{\text{eff}}}{1 + 2\sqrt{\varepsilon_{\text{eff}}}}\right\} \quad , \quad \varepsilon_{\text{eff}} = 0.67\varepsilon \cdot (1 - 1.4\delta |\delta|) \tag{38}$$

with the triangularity δ of the LCFS; the (average) triangularity is defined as $\delta(r) = \frac{1}{r} \cdot \left(R_0 - \frac{1}{2}(R^\uparrow + R^\downarrow)\right)$ where $P^\uparrow = (R^\uparrow, Z^\uparrow)$ and $P^\downarrow = (R^\downarrow, Z^\downarrow)$ are the vertically highest and lowest points for any flux surface.

2.3.2 Redl model

In comparison to calculations by the NEO code, which is a state-of-the-art drift-kinetic solver, the Sauter model usually predicts the bootstrap current for low to intermediate collisionalities with an error of ~ 10 to 20% in the pedestal [37][38]. However, the predicted current density is significantly overestimated compared to the NEO outcomes in the high collisionality regime, due to technical limitations in running the CQLP and CQL3D codes at high collisionalities back in 1999 when the Sauter model was developed [37][39]. In addition, the ion flow term $\tilde{\alpha}$ was calculated using the reduced electron-ion coupling in the CQLP and CQL3D codes, leading to additional differences in the high collisionality regime where electron-ion coupling becomes increasingly important, and the effect of multiple impurity species was approximated by varying the main ion charge [31][37]. Recently, the Sauter model

was improved by A. Redl to increase accuracy in the high collisionality regime and correctly include the effect of impurities by fitting the outcomes of the NEO code [39]. The resulting formulas of the Redl model are given in the appendix A.2, with the impurity strength $\tilde{\alpha}_I$ defined as [39]:

$$\tilde{\alpha}_I = \frac{\sum Z_\alpha^2 n_\alpha}{Z_{\text{main}}^2 n_{\text{main}}} \tag{39}$$

where n_{main} and Z_{main} are the main ion density and charge number, respectively, and the sum $\sum$ is over all impurity species α. Assuming only a single impurity species with density n_{imp} and charge number Z_{imp} as well as $Z_{\text{main}} = 1$, the impurity strength might be expressed as:

$$\tilde{\alpha}_I = \frac{Z_{\text{imp}}^2 \tilde{\eta}}{\eta - \tilde{\eta}} \tag{40}$$

where the density scale factors

$$\tilde{\eta} = \frac{Z_{\text{eff}} - 1}{Z_{\text{imp}} \cdot (Z_{\text{imp}} - 1)} \quad \text{and} \quad \eta = \left(Z_{\text{eff}} - \tilde{\eta} \cdot Z_{\text{imp}}^2 \right) + \tilde{\eta} \tag{41}$$

are defined such that $n_{\text{imp}} = \tilde{\eta} \cdot n_e$ and $n_i = \eta \cdot n_e$. Finally, comparing the Redl model to outcomes from the NEO code results in errors of $\lesssim 5\%$ over a large range of magnetic equilibria and collisionalities [39].

2.4 EPED1 model for density and temperature profiles

EPED1 is a framework predicting pedestal stability that defines model density and temperature profiles for a set of global parameters and combines MHD stability calculations with a pedestal width-height relation [13]. The input parameters for EPED1 are:

- Shaping parameters for the LCFS: Major radius $R_{\text{maj}} \equiv R_0(a)$, minor radius a, elongation κ and triangularity δ

- Plasma parameters: Vacuum toroidal magnetic field at the magnetic axis B_T, plasma current I_P, normalized beta β_N, effective charge Z_{eff} and impurity charge Z_{imp}.

- Pedestal parameters: Pedestal width scale w_{pre}.

- Scan parameters: Electron pedestal top density $n_{\text{e,ped}}$ and pedestal top temperature T_{ped} or pressure p_{ped}.

In addition, information on the equilibrium volume profile $V(\psi)$ is required. Moreover, it is assumed that electron and ion temperature are equal [13]. In principle, temperature, density and pressure are connected via the ideal gas law and thus equivalent input parameters. We will for the following assume that we are given the pedestal top pressure p_{ped}.

The dimensions of the pedestal, namely height, width and gradient, are connected via the relation "gradient $= \frac{\text{height}}{\text{width}}$". Therefore, there are two independent dimensions, which have to be determined. As discussed in section 2.1, ideal MHD yields a critical pressure gradient, but provides no relation for the independent pedestal dimensions. For EPED1, the required relation is given by a simple empirical scaling law [13][41]:

$$\Delta = w_{\text{pre}} \cdot \beta_{\text{pol,ped}}^{\alpha_w} \quad , \qquad \alpha_w = 0.5 \tag{42}$$

with

$$\beta_{\text{pol,ped}} = \frac{2\mu_0 \cdot p_{\text{ped}}}{\langle B_{\text{pol}} \rangle^2} \quad , \qquad \langle B_{\text{pol}} \rangle = \frac{\mu_0 \cdot I_P}{L(a)} \tag{43}$$

where Δ is the pedestal width defined as the average pedestal width of temperature and density profiles, w_{pre} is a prefactor that is assumed to stay roughly constant for fixed aspect ratio, $\beta_{\text{pol,ped}}$ is the pedestal poloidal beta, α_w is the width scaling exponent, $\langle B_{\text{pol}} \rangle$ is the flux surface averaged poloidal magnetic field and $L(a)$ is the circumference of the LCFS. This relation now reduces the amount of independent pedestal dimensions to 1, allowing the study of MHD edge stability in terms of only a single pedestal dimension. The width relation, which prescribes a path in the Δ-p_{ped} space, and results from ideal MHD, which yield growth rates at every point in the Δ-p_{ped} space, are shown in figure 10 (page 19).

For some data sets, the correlation of the introduced width scaling is observed to be of the order $Corr \sim 0.68$ with a standard deviation of $\sigma_{\text{std}} \sim 0.20$, indicating significant scatter of experimental data with respect to the scaling [41]. This scatter can be seen as an uncertainty of w_{pre} for fixed α_w. In addition, for some data sets, the scaling exponent α_w seems to deviate from its proposed value of 0.5 [41]. These uncertainties have to be considered when determining the prediction error of the model.

The empirical width scaling in equation 42 might be interpreted as a transport constraint. P. Snyder and others argue that the constraint is linked to the onset kinetic ballooning modes (KBM) investigating similarities in the respective scaling laws [13]. This idea is further developed in EPED1.6 where the prefactor w_{pre}, which has to be determined experimentally, is replaced by a function G of shaping, collisionality and further influences that can be obtained from KBM stability evaluation using the "ballooning critical pedestal" technique [42]. Moreover, T. Luda and others suggest a different empirical pedestal width scaling, originally discovered by P. A. Schneider, that is proposed to be related to electron temperature gradient modes (ETG), given by $T_{\text{e,ped}}/|\vec{\nabla} T_e| = 2.0$ cm [43][44]. Their recently developed predictive framework couples core and pedestal transport models and considers, in contrast to EPED1, differences in electron and ion temperatures $T_e \neq T_i$, distinct temperature and density pedestal widths as well as influences of gas puff on the pedestal width [44].

To continue with EPED1, model density and temperature profiles, resulting in a model pressure profile required for MHD stability calculations, are defined as [13]:

$$n_e(\tilde{\psi}) = n_{\text{e,edge}}(\tilde{\psi}) + a_{n1} \cdot n_{\text{e,core}}(\tilde{\psi})$$
$$T(\tilde{\psi}) = T_{\text{edge}}(\tilde{\psi}) + a_{T1} \cdot T_{\text{core}}(\tilde{\psi}) \tag{44}$$

---

with

$$n_{\mathrm{e,edge}}(\tilde{\psi}) = n_{\mathrm{e,sep}} + a_{n0}\left[\tanh\left(\frac{2(1-\tilde{\psi}_{\mathrm{mid}})}{\Delta}\right) - \tanh\left(\frac{2(\tilde{\psi}-\tilde{\psi}_{\mathrm{mid}})}{\Delta}\right)\right]$$

$$T_{\mathrm{edge}}(\tilde{\psi}) = T_{\mathrm{sep}} + a_{T0}\left[\tanh\left(\frac{2(1-\tilde{\psi}_{\mathrm{mid}})}{\Delta}\right) - \tanh\left(\frac{2(\tilde{\psi}-\tilde{\psi}_{\mathrm{mid}})}{\Delta}\right)\right]$$

$$n_{\mathrm{e,core}}(\tilde{\psi}) = \Theta\left(1 - \frac{\tilde{\psi}}{\tilde{\psi}_{\mathrm{ped}}}\right) \cdot \left[1 - \left(\frac{\tilde{\psi}}{\tilde{\psi}_{\mathrm{ped}}}\right)^{\alpha_{n1}}\right]^{\alpha_{n2}}$$

$$T_{\mathrm{core}}(\tilde{\psi}) = \Theta\left(1 - \frac{\tilde{\psi}}{\tilde{\psi}_{\mathrm{ped}}}\right) \cdot \left[1 - \left(\frac{\tilde{\psi}}{\tilde{\psi}_{\mathrm{ped}}}\right)^{\alpha_{T1}}\right]^{\alpha_{T2}} \tag{45}$$

and

$$\tilde{\psi}_{\mathrm{mid}} = 1 - \frac{\Delta}{2} \quad, \qquad \tilde{\psi}_{\mathrm{ped}} = 1 - \Delta$$

$$\alpha_{n1} = \alpha_{n2} = 1.1 \quad, \qquad \alpha_{T1} = 1.2 \quad, \qquad \alpha_{T2} = 1.4 \tag{46}$$

where $\tilde{\psi}$ is the normalized poloidal flux, $n_{\mathrm{e,sep}}$ and T_{sep} are the separatrix density and temperature, a_{n0} and a_{T0} are linked to the pedestal top density and temperature, a_{n1} is linked to the density at the magnetic axis, a_{T1} has to be determined from the normalized beta β_N and $\Theta(\dots)$ denotes the Heaviside function. As the normalized beta is a boundary condition to be fulfilled by the pressure profile, either a_{n1} or a_{T1} is a free parameter that weakly influences the shape of the core pressure profile. We choose a slightly increasing density profile towards the magnetic axis by

$$a_{n1} = 1 \cdot 10^{19} \text{ m}^{-3} \ .$$

In EPED1 the separatrix values are fixed to

$$n_{\mathrm{e,sep}} = \alpha_{n0} \cdot n_{\mathrm{e,ped}} \quad, \qquad T_{\mathrm{sep}} = 75 \text{ eV} \tag{47}$$

where $\alpha_{n0} = 1/4$ is chosen as a typical scaling relation [13]. We retain this scaling, but adjust the factor to be $\alpha_{n0} = 1/3$ for AUG scans. Next, the factors a_{n0} and a_{T0} are defined so that the profiles approximately match their specified pedestal values

$$a_{n0} = \frac{n_{\mathrm{e,ped}} - n_{\mathrm{e,sep}}}{1.75} \quad, \qquad a_{T0} = \frac{T_{\mathrm{ped}} - T_{\mathrm{sep}}}{1.75} \tag{48}$$

with T_{ped} calculated using the ideal gas law

$$T_{\mathrm{ped}} = \frac{p_{\mathrm{ped}}}{k_B n_{\mathrm{ped}}} \quad, \qquad n_{\mathrm{ped}} = n_{\mathrm{e,ped}} + n_{\mathrm{i,ped}} = n_{\mathrm{e,ped}} \cdot (1 + \eta)$$

where k_B is the Boltzmann constant, $n_{\mathrm{i,ped}}$ is the ion pedestal density and η is the density scale factor defined in section 2.3.2.

Lastly, from the specified normalized beta, we can calculate the volume averaged pressure

$$p_{\mathrm{av}} = \beta \cdot \frac{B_T^2 + \langle B_{\mathrm{pol}}\rangle^2}{2\mu_0} \quad, \qquad \beta = \frac{\beta_N}{100} \cdot \frac{I_P[\mathrm{MA}]}{a[\mathrm{m}] \cdot B_T[\mathrm{T}]} \tag{49}$$

where β is the total plasma beta. Subsequently, a_{T1} is determined such that the volume average of the resulting pressure profile equals p_{av}:

$$a_{T1} = \frac{1}{\left\langle n_e(\tilde\psi) \cdot T_{\mathrm{core}}(\tilde\psi) \right\rangle_V} \cdot \left[\frac{p_{\mathrm{av}}}{k_B \cdot (1+\eta)} - \left\langle n_e(\tilde\psi) \cdot T_{\mathrm{edge}}(\tilde\psi) \right\rangle_V \right] \qquad (50)$$

where the volume-average $\langle \dots \rangle_V$ is evaluated with respect to the equilibrium volume profile $V(\psi)$. Example EPED1 profiles are shown in figure 9.
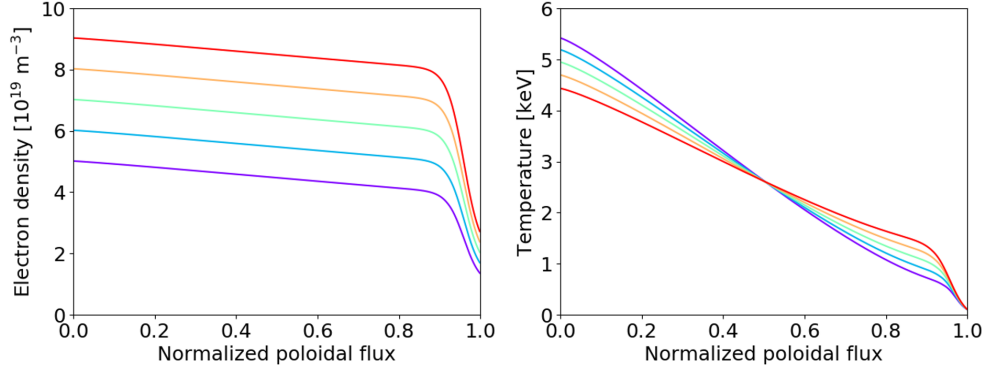

Figure 9: EPED1 profiles created with IPED 2 for an AUG-like plasma (see appendix B.2 "Parameter sets"). Left: Density profiles where pedestal top densities from purple to red are $n_{\mathrm{e,ped}} = 4,\ 5,\ 6,\ 7,\ 8\ [10^{19}\ \mathrm{m}^{-3}]$. Right: Temperature profiles with $\beta_N = 1.8$ and $n_{\mathrm{e,ped}} = 5 \cdot 10^{19}\ \mathrm{m}^{-3}$ where pedestal top pressures from purple to red are $p_{\mathrm{ped}} = 10,\ 13,\ 16,\ 19,\ 22$ kPa.
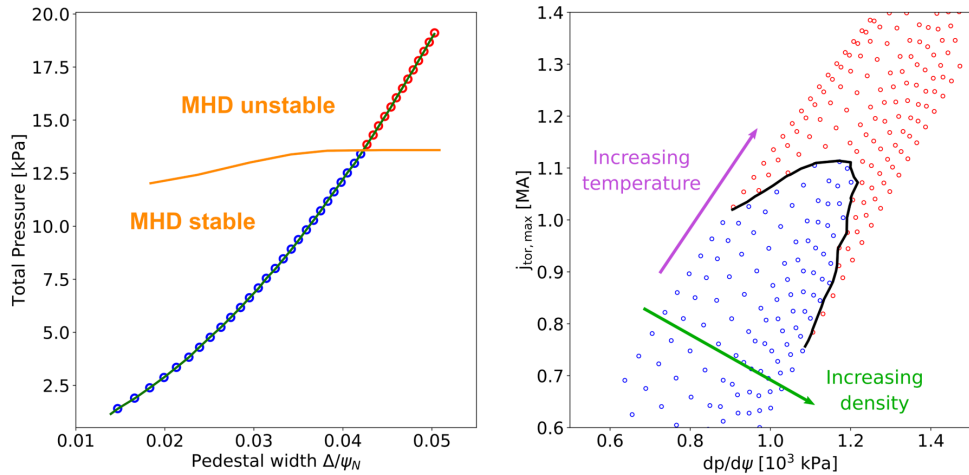

Figure 10: Left: EPED height-width constraint (green; equation 42) fixing the path in the Δ-p_{ped} diagram as well as MHD stable (blue) and unstable (red) points for a single density $n_{\mathrm{e,ped}}$; sketch of the MHD stability boundary (orange) separating Δ-p_{ped} space; the predicted critical pressure is given by the crossing of the orange and the green line. Right: Stability scans for multiple densities in edge-current-density vs pressure-gradient space; the critical pressures for the different densities create a stability boundary (black).

After creation of the temperature and density profiles according to equation 44, EPED1 creates a current density profile using the bootstrap current calculated from the Sauter model (see section 2.3.1) for the pedestal region defined by Δ and a simple polynomial core current profile that obeys the boundary conditions of $q_0 = 1.05$ and an integrated current of I_P [13]. The use of a simple polynomial core current profile is based on the assumption that "details of the [core] current profile are relatively unimportant" [13]. We will discuss the effect of the core current density later in this work.

Finally, the EPED1 framework is directly integrated into an equilibrium code that generates the EPED1 model profiles simultaneously to solving the Grad-Shafranov equation and uses the stability code ELITE to calculate ideal MHD growth rates [13]. This is done for a range of pedestal top densities and pressures, which results in a prediction of the stability boundary [13]. Figure 10 shows such a stability scan; here performed by the IPED 2 framework, which is based on the EPED1 model, instead of the EPED1 framework.

2.5 Density dependence and the Super-H mode

A natural space to analyze the results from the EPED model is the p_{ped}-$n_{\text{e,ped}}$ space, i.e. the space of scan parameters, which for the remaining work will be shortly called p-n space. While, in principle, one would not expect a density dependence of the normalized growth rates $\gamma_{\text{MHD}} \cdot \tau_A$ for ideal MHD (as already mentioned in section 2.2), explicit density dependencies enter though both the edge current density, given mainly by the bootstrap current, and the normalized effective DDFs $\omega_{*,i}^{\text{eff1}} \cdot \tau_A$ and $\omega_{*,i}^{\text{eff2}} \cdot \tau_A$. Thus, because of the integrated bootstrap model and also because of the effective diamagnetic stabilization, ideal as well as diamagnetically stabilized normalized growth rates that are calculated using the EPED model are expected to be density dependent. The relation between the p-n space and the s-α space, which according to section 2.1 seems to be a natural space for ideal MHD stability, is further discussed in chapter 5.
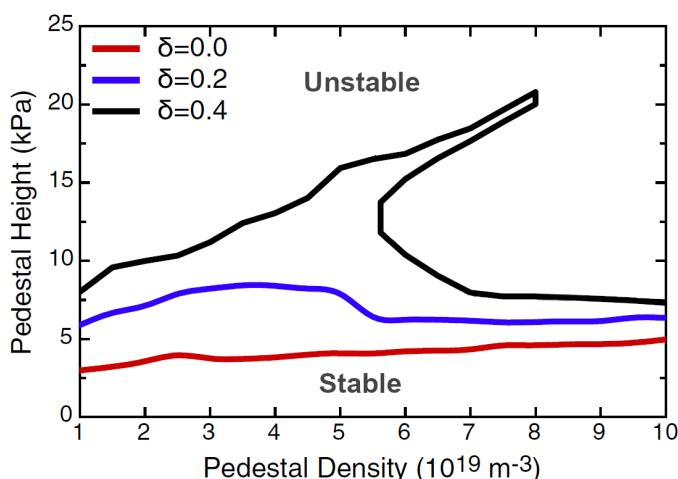

Figure 11: Marginal stability calculated by the EPED1 framework for a DIII-D scenario (see appendix B.2 "Parameter sets") with $\kappa = 1.89$ and different triangularities. At high plasma shaping a stable "branch" forms that is only accessible if the density is varied. Adapted from [15].

In 2015, P. B. Snyder and others discovered that the EPED framework in some cases, especially for strongly shaped flux surfaces, predicts more than one critical pressure for a fixed density [15]. This results in a regime of significantly enhanced stable pedestal pressures, called the Super H-mode, that is only experimentally accessible if the density is increased while remaining on the peeling mode limited boundary. The marginal stability as predicted by the EPED framework is shown for different triangularities in figure 11, where for $\delta > 0.4$ a stable "channel", the Super H branch, opens [15]. The reproduction of the Super H solution within the IPED 2 framework has been attempted and results are discussed in chapter 4.

2.6 The IPED 1 framework

IPED 1 is a predictive framework written by M. G. Dunne which creates model equilibria, current density and pressure profiles from the same set of input parameters as EPED and then uses HELENA and MISHKA to compute ideal growth rates [17][18][19]. Moreover, the framework is organized in a modularized form and can be easily expanded by further models for the bootstrap current or temperature and density profiles. The code part creating the model equilibria, current density and pressure profiles is called Profile Creator.

In order to create the model equilibria, firstly, the LCFS is either parametrized as

$$\vec{\gamma_r}(t) = \begin{pmatrix} R_a(t) \\ Z_a(t) \end{pmatrix} = \begin{pmatrix} R_0(a) + a\cos\left(t + \delta\sin(t)\right) \\ a\kappa\sin(t) \end{pmatrix}, \ t \in [0, 2\pi] \qquad (51)$$

or identified with a prescribed separatrix. From this, the length $L_a \equiv L(a)$ as well as the area A_a of the LCFS can be calculated by integration of the parametrization. The volume of the LCFS is estimated by $V_a = 2\pi\overline{R}A_a$, where $\overline{R}$ is the average radius of the LCFS. Then, the volume profile is approximated based on power law fits of several equilibria to:

$$V(\tilde{\psi}) = V_a \cdot \tilde{\psi}^{\alpha_V} \quad , \qquad \alpha_V \approx 1.5 \qquad (52)$$

Subsequently, the equilibrium area, minor radius and safety factor profiles are determined to:

$$A(\tilde{\psi}) = V(\tilde{\psi})/(2\pi\overline{R}) \qquad (53)$$

$$r(\tilde{\psi}) = \sqrt{A(\tilde{\psi})/\pi} \quad \text{with} \quad \psi(r = a) = -\frac{\mu_0 I_P \overline{R} a}{2\pi L(a)} \qquad (54)$$

$$q(\tilde{\psi}) = (q_{\max} - 1) \cdot \left[\exp(\tilde{\psi}^2) - 1\right] + 1 \quad \text{with} \quad q_{\max} = \frac{2\pi a^2 B_T}{\mu_0 I_P \overline{R}} \cdot \frac{1 + \kappa^2}{2} \qquad (55)$$

Secondly, the generated model equilibria are used to calculate the EPED profiles and the Sauter bootstrap current $\langle j_{\text{BS}}\rangle_B$ according to sections 2.3.1 and 2.4. Then, the area-averaged current density is created by truncating the bootstrap current density $j_{\text{ped}} = \langle j_{\text{BS}}\rangle_B$ at $\tilde{\psi} = \tilde{\psi}_{\text{cut}} \equiv 1 - 2\Delta$ and adding a simple current density profile for the core plasma similar to the EPED framework:

$$\langle j_{\text{tor}}\rangle_A (\tilde{\psi}) = \begin{cases} c_1 + c_2\tilde{A}(\tilde{\psi}) + c_3\tilde{A}(\tilde{\psi})^2 + j_{\text{ped}}(\tilde{\psi}_{\text{cut}}) & \text{for } \tilde{\psi} \leqslant \tilde{\psi}_{\text{cut}} \\ \\ j_{\text{ped}}(\tilde{\psi}) & \text{for } \tilde{\psi} > \tilde{\psi}_{\text{cut}} \end{cases} \qquad (56)$$

with

$$\tilde{A}(\tilde{\psi}) = A(\tilde{\psi})/A(\tilde{\psi}_{\text{cut}}) \qquad , \qquad c_1 = j_0 - j_{\text{ped}}(\tilde{\psi}_{\text{cut}})$$

$$c_2 = j_{\text{ped}}(\tilde{\psi}_{\text{cut}}) - j_0 - c_3 \qquad , \qquad c_3 = 6\left[0.5\left(j_0 - j_{\text{ped}}(\tilde{\psi}_{\text{cut}})\right) - j_{\text{av}}\right]$$

and

$$j_0 = \frac{2B_T}{1.3\mu_0\overline{\overline{R}}} \qquad , \qquad j_{\text{av}} = \frac{I_P - I_{\text{ped}} - I_0}{A(\tilde{\psi}_{\text{cut}})}$$

$$I_{\text{ped}} = \int_{\tilde{\psi}_{\text{cut}}}^1 j_{\text{ped}} \cdot \partial_{\tilde{\psi}} A \, d\tilde{\psi} \qquad , \qquad I_0 = j_{\text{ped}}(\tilde{\psi}_{\text{cut}}) \cdot A(\tilde{\psi}_{\text{cut}})$$

where $\langle\ldots\rangle_A$ denotes the area-average, precisely defined in the appendix B.1 "Averages". The area-average fulfills the equality

$$\int_0^{\tilde{\psi}_0} \langle\ldots\rangle_A \cdot \partial_{\tilde{\psi}} A \, d\tilde{\psi} = \int_{\mathcal{A}(\tilde{\psi}_0)} \ldots \, d\vec{x}^2 \quad \text{for all} \quad \tilde{\psi}_0 \in [0,1]$$

where $\mathcal{A} \in \mathbb{R}^2$ is the area enclosed by a flux-surface in the (R, Z)-plane and $A = \text{area}(\mathcal{A})$.

Finally, the resulting pressure and current density profiles as well as the plasma boundary (equation 51) are then processed by HELENA and MISHKA to calculate ideal MHD growth rates.

3 Implementation of IPED 2.0

3.1 Structural overview and code development

As part of this thesis, the IPED 1 framework was upgraded to IPED 2. The changes of this upgrade are discussed in the following. Figure 12 shows the structure of the Profile Creator code for both IPED versions. There are two major structural changes from IPED 1 to IPED 2. Firstly, using IPED 1, we experienced that the current density and pressure profiles were sometimes scaled by HELENA, indicating a difference between the ad-hoc equilibrium estimate of IPED 1 (equations 51 to 55) and the HELENA equilibrium. Thus, the equilibrium model of IPED 1 was replaced by a more precise equilibrium estimation procedure based on a fixed set of flux surfaces. Secondly, since the new equilibrium estimate takes the current density profile into account to calculate flux coordinates, it is possible to iterate until the current profile is self-consistent with respect to the set of flux surfaces. This means that the converged current profile creates flux coordinates resulting in an equal current density profile again. In addition, a new bootstrap current model (Redl, see section 2.3.2) as well as new core current profile shapes were implemented. Lastly, minor corrections, including $\langle j_{\mathrm{tor}} \rangle_A \neq \langle j_{\mathrm{tor}} \rangle_B$, were applied and the code was translated from IDL to Python 3.

(a) Profile Creator of IPED 1
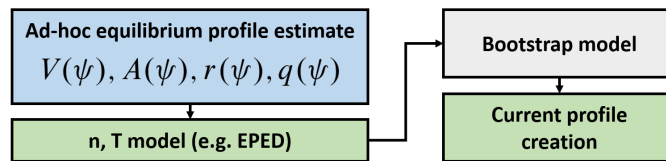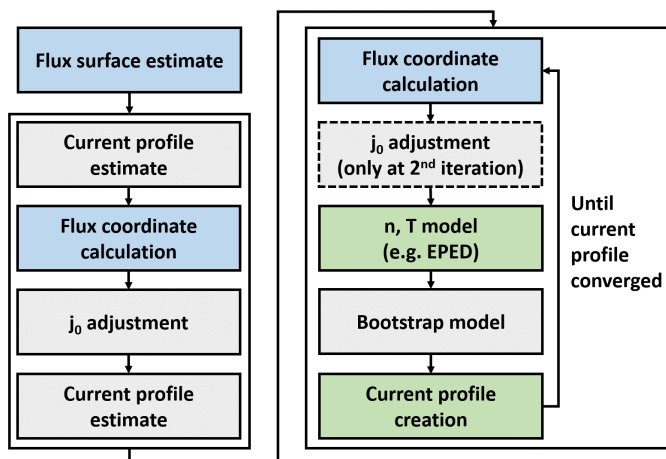
(b) Profile Creator of IPED 2

Figure 12: Code structure of the Profile Creator of IPED for a single pedestal top density and temperature. Blue: equilibrium model, Green: pressure and current profile output.

In principle, IPED 2 takes the same input parameters as EPED and IPED 1. However, it is also possible to pass the ratio of global and pedestal beta, i.e. $c_\beta \equiv \frac{p_{\mathrm{av}}}{p_{\mathrm{ped}}}$, instead of the normalized beta, which roughly accounts for the effect of profile stiffness. These inputs are connected by equation 49 (page 18). As for IPED 1, the

equilibrium estimation was generalized to process a prescribed input separatrix, overriding the shaping parameters, which is further discussed in section 3.2.2.
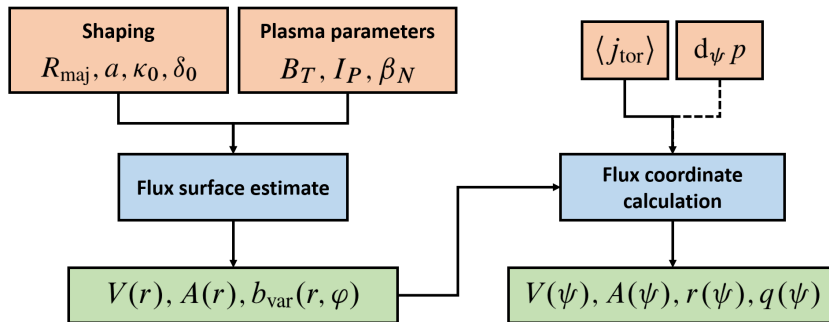

Figure 13: Dependencies of the equilibrium estimation. Blue: Procedure, Red: Input, Green: Output. Dashed arrow: Only if available.

Figure 13 shows the dependencies of the new equilibrium estimation procedure, which is divided in "flux surface estimation" and "flux coordinate calculation"; the detailed structure of the equilibrium profile creation is illustrated in figure 12b. At first, the shape of the equilibrium flux surfaces is parametrized based on an analytical solution of the Grad-Shafranov equation and approximate shaping profiles $\kappa(r)$ and $\delta(r)$. This yields volume $V(r)$ and area $A(r)$ profiles as well as the poloidal variation of the poloidal magnetic field (section 3.2). In order to calculate the poloidal flux and the safety factor profile, information on the current density profile is needed. However, since flux coordinates are required for the EPED and bootstrap current models, an initial edge current density has to be estimated (section 3.3). From this estimated edge current density, a current density profile is created (section 3.4). Subsequently, the poloidal flux $\psi(r)$ and safety factor $q(r)$ are calculated with respect to the estimated flux surface geometry (section 3.5). To guarantee a certain safety factor at the magnetic axis, the axis current density j_0 is adjusted twice during the equilibrium estimation procedure (section 3.5). Then, using the equilibrium profiles in flux coordinates, EPED profiles and the bootstrap current can be determined and the resulting current profile is used to recalculate the poloidal flux. This is repeated until the current profile is self-consistent, which means that it generates flux coordinates resulting in an equal current density profile again. While the iterative loop estimates the equilibrium profiles, it is not a proper solution of the Grad-Shafranov equation. A comparison between the obtained estimate and the proper Grad-Shafranov solution calculated by HELENA is given in section 3.6.

3.2 Flux surface estimate

3.2.1 Flux surface geometry from shaping parameters

In this section, we derive estimates for equilibrium profiles in spatial coordinates independent from the details of pressure and current density profiles. Results that are used for the calculation of equilibrium profiles in flux coordinates are boxed. As basis for the equilibrium profile estimation, we use the analytical set of flux surfaces from Miller and others [23]:

$$\vec{\gamma_r}(t) = \begin{pmatrix} R(r,t) \\ Z(r,t) \end{pmatrix} = \begin{pmatrix} R_0(r) + r\cos\left(t + \sin^{-1}(\delta(r))\sin(t)\right) \\ Z_M + r\kappa(r)\sin(t) \end{pmatrix}, \; t \in [0, 2\pi] \quad (57)$$

where r is the minor radius, $\kappa(r)$ is the elongation, $\delta(r)$ is the triangularity, $R_0(r) = R_{\mathrm{maj}} + \Delta_s(r)$ is the major radius, Z_M is the vertical position of the magnetic axis and the Shafranov shift $\Delta_s(r)$ is calculated using equation 11 (page 6). The choice of Z_M is free, since the Grad-Shafranov equation is translation invariant in the Z-direction. In general, the profiles $\kappa(r)$, $\delta(r)$ and $R_0(r)$ are given by the solution of the Grad-Shafranov equation for a specific safety factor and pressure gradient profile [23]. We estimate the shaping profiles independently from pressure and current density profiles following Chen and others (see [45]):

$$\delta(r) = \delta_0 \cdot \left(\frac{r}{a}\right)^2 \quad , \quad \kappa(r) = \kappa_0 - 0.3 + 0.3\left(\frac{r}{a}\right)^4 \tag{58}$$

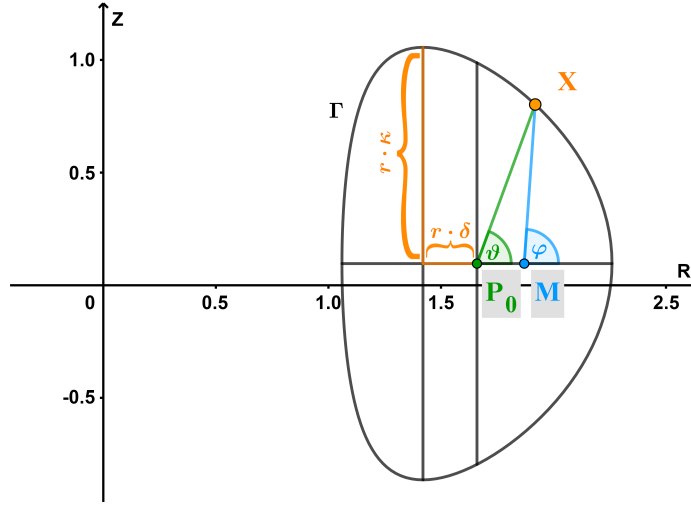where κ_0 is the elongation at the LCFS and δ_0 is the triangularity at the LCFS.

Figure 14: Miller flux surface Γ_r with $R_0 = 1.66$, $r = 0.6$, $\kappa = 1.6$, $\delta = 0.4$ and $Z_M = 0.1$. $M = (R_M, Z_M)$ is the magnetic axis and $P_0 = (R_0, Z_M)$ is the flux surface center. φ and ϑ are poloidal angles with respect to M and P_0, respectively.

The set of equations 57 and 58 defines our estimate of equilibrium flux surfaces. A single Miller flux surface $\Gamma_r = \gamma_r([0, 2\pi])$ is shown in figure 14. To ensure that the area enclosed by Γ_r is convex and that the set of flux surfaces is nested, we require $\Delta_s < \frac{a}{2}$ and $|\delta_0| < 0.8$. Moreover, we define a general poloidal coordinate τ such that there is a diffeomorphism between t and τ for every r, i.e. there is a smooth coordinate transform. Hence, the angle to the magnetic axis φ and the angle to the flux surface center ϑ are general poloidal coordinates. The formulation in a general poloidal coordinate τ can be useful, since it ensures that the equations can be directly applied to entities that are not given on a regular grid in t, φ or ϑ. It is remarked that the curve parameter t is in general not equal to the poloidal angles φ and ϑ.

Subsequently, using $V = \int_V \mathrm{div}\,(z\vec{e_z})\,\mathrm{dV} = \int_{\partial V} z\vec{e_z}\cdot\mathrm{d}\vec{\sigma}$ and equation 57, volume and area profiles can be reduced to:

$$V(r) = -2\pi \int_{\tau(0)}^{\tau(2\pi)} R(r,\tau)Z(r,\tau)\partial_\tau R(r,\tau)\mathrm{d}\tau \;,\; A(r) = -\int_{\tau(0)}^{\tau(2\pi)} Z(r,\tau)\partial_\tau R(r,\tau)\mathrm{d}\tau \tag{59}$$

Additionally, one can determine the poloidal dependence of the poloidal magnetic field B_{pol}. For this purpose, we define a poloidal surface as a surface that is toroidally symmetric and transverse to the poloidal magnetic field:

$$\mathcal{A}_{\mathrm{pol}}(r,\varphi) = \left\{ \begin{pmatrix} R(\tilde{r},\varphi) \cdot \cos(\Phi) \\ R(\tilde{r},\varphi) \cdot \sin(\Phi) \\ Z(\tilde{r},\varphi) \end{pmatrix} \,\middle|\, \tilde{r} \in [0,r],\, \Phi \in [0,2\pi] \right\}, \qquad (60)$$

where $\vec{\mathcal{A}}_{\mathrm{pol}}(r,\varphi)\|\vec{e_\varphi}$ is the surface normal vector, $A_{\mathrm{pol}} = \mathrm{area}(\mathcal{A}_{\mathrm{pol}})$ is the surface area and Φ is the toroidal angle. The poloidal cross section of such a poloidal surface, spanning from the magnetic axis to a flux surface Γ_r, is represented by the blue line in figure 14. Consider a volume bounded by two poloidal surfaces $\mathcal{A}_{\mathrm{pol}}(r,\varphi_1)$ and $\mathcal{A}_{\mathrm{pol}}(r,\varphi_2)$ as well as the flux surface described by Γ_r. Then, according to $\vec{\nabla} \cdot \vec{B} = 0$, the flux through $\mathcal{A}_{\mathrm{pol}}(r,\varphi_1)$ must be equal to the flux through $\mathcal{A}_{\mathrm{pol}}(r,\varphi_2)$ for every $r \in [0,a]$. Thus, we can derive an expression for the differential poloidal flux:

$$\mathrm{d}\psi = \underbrace{B_{\mathrm{pol}} \cdot \cos\left(\angle(\vec{B}_{\mathrm{pol}}, \vec{\mathcal{A}}_{\mathrm{pol}})\right) \cdot \partial_r A_{\mathrm{pol}}}_{\text{Functions of } \varphi} \mathrm{dr} = \mathrm{const.} \text{ in } \varphi \qquad (61)$$

To generalize, the equations 60 and 61 also hold when exchanging φ by τ. This might be useful to reduce computational costs significantly if including these calculations in a loop, because no interpolations are needed if $\tau = t$. Next, the upper expression can be solved for the normalized poloidal variation $b_{\mathrm{var}}(r,\tau)$ of the poloidal magnetic field $B_{\mathrm{pol}}(r,\tau) = b_0(r) \cdot b_{\mathrm{var}}(r,\tau)$, where $b_0(r)$ will be determined in section 3.5:

$$\boxed{b_{\mathrm{var}}(r,\tau) = \widetilde{b_{\mathrm{var}}}(r,\tau) \cdot \left(\int_{\tau(0)}^{\tau(2\pi)} \widetilde{b_{\mathrm{var}}}(r,\tau) \cdot \|\partial_\tau \vec{\gamma_r}(\tau)\|_2 \mathrm{d}\tau \right)^{-1}} \qquad (62)$$

where

$$\boxed{\begin{aligned} \widetilde{b_{\mathrm{var}}}(r,\tau) &= \left\{ \left| \cos\left[\tan^{-1}\left(\tfrac{\partial_\tau Z(r,\tau)}{\partial_\tau R(r,\tau)} \right) + \tan^{-1}\left(\tfrac{\partial_r R(r,\tau)}{\partial_r Z(r,\tau)} \right) \right] \right| \cdot \partial_r A_{\mathrm{pol}}(r,\tau) \right\}^{-1} \\ \partial_r A_{\mathrm{pol}}(r,\tau) &= 2\pi \cdot R(r,\tau) \cdot \sqrt{(\partial_r R(r,\tau))^2 + (\partial_r Z(r,\tau))^2} \end{aligned}} \qquad (63)$$

For $\tau = \varphi$, equation 63 can be reduced to the form implemented in IPED 2:

$$\widetilde{b_{\mathrm{var}}}(r,\varphi) = \left\{ \left| \sin\left[\tan^{-1}\left(\tfrac{\partial_\varphi Z(r,\varphi)}{\partial_\varphi R(r,\varphi)} \right) - \varphi \right] \right| \cdot \partial_r A_{\mathrm{pol}}(r,\varphi) \right\}^{-1}$$

$$A_{\mathrm{pol}}(r,\varphi) = \pi \cdot (R(r,\varphi) + R_M) \cdot \sqrt{(R(r,\varphi) - R_M)^2 + (Z(r,\varphi) - Z_M)^2} \qquad (64)$$

It is remarked that the poloidal areas in equation 64 need to be evaluated numerically, as the transformation $\varphi(t)$ is in general a complicated function. We also define a circumference coordinate, which is used to determine the safety factor later:

$$C_r(\varphi) = \int_0^\varphi \|\partial_\varphi \vec{\gamma_r}(\varphi)\|_2 \mathrm{d}\varphi \qquad (65)$$

3.2.2 Flux surface geometry from a prescribed separatrix

Instead of supplying shaping parameters R_{maj}, a, κ_0 and δ_0 (see figure 13), it is also possible to pass an experimentally determined separatrix $\vec{\gamma}^{\mathrm{SEP}}(\tau) = (R_s(\tau), Z_s(\tau))$ to the Profile Creator code. Then, the shaping parameters can be calculated from the input separatrix:

$$R_{\mathrm{maj}} = \tfrac{1}{2} \cdot (\max (R_s) + \min (R_s)) \qquad\qquad \kappa_0 = \tfrac{1}{2} \cdot (\kappa_\downarrow + \kappa_\uparrow)$$

$$a = \tfrac{1}{2} \cdot (\max (R_s) - \min (R_s)) \qquad\qquad \delta_0 = \tfrac{1}{2} \cdot (\delta_\downarrow + \delta_\uparrow) \qquad (66)$$

$$Z_M = \tfrac{1}{2} \cdot [Z_s (\mathrm{amax} (R_s)) + Z_s (\mathrm{amin} (R_s))]$$

where

$$\kappa_\downarrow = \tfrac{1}{a} \cdot (Z_M - \min (Z_s)) \qquad \delta_\downarrow = \tfrac{1}{a} \cdot (R_{\mathrm{maj}} - R_s (\mathrm{amin} (Z_s)))$$

$$\kappa_\uparrow = \tfrac{1}{a} \cdot (\max (Z_s) - Z_M) \qquad \delta_\uparrow = \tfrac{1}{a} \cdot (R_{\mathrm{maj}} - R_s (\mathrm{amax} (Z_s))) \qquad (67)$$

In the upper equations *amax* and *amin* are the argument maximum and argument minimum, respectively. We assume that the area enclosed by the input separatrix is convex and that the separatrix is nearly untilted, i.e.

$$|Z_s (\mathrm{amax} (R_s)) - Z_s (\mathrm{amin} (R_s))| \ll 2a \; .$$

For the following, we want to define an assimilated set of flux surfaces that estimates the true equilibrium well while keeping computational cost low. For this purpose, we reshape the Miller flux surfaces so that they approach the input separatrix for $r \to a$ in a purely geometrical manner. As the geometric profiles are integrated quantities, it is assumed that the estimated equilibrium profiles are not strongly influenced by the detailed geometry of the flux surfaces. At first, we redefine the shaping parameters κ_0 and δ_0 from equations 58 and 66 to be step functions of t:

$$\kappa_0(t) = \begin{cases} \kappa_\uparrow & \text{for } t \leqslant \pi \\[2mm] \kappa_\downarrow & \text{for } t > \pi \end{cases} \; , \qquad \delta_0(t) = \begin{cases} \delta_\uparrow & \text{for } t \leqslant \pi \\[2mm] \delta_\downarrow & \text{for } t > \pi \end{cases} \qquad (68)$$

Then, the set of equations 57 and 58 together with 68 defines a set of up-down asymmetric Miller flux surfaces $\vec{\gamma_r}^{\mathrm{AMS}}(t) = (R_m(r, t), Z_m(r, t))$, which is used as the basis for reshaping. Subsequently, we introduce a reshape cut-off parameter ξ that will be discussed later in this section. For $r \leqslant \xi \cdot a$, the assimilated flux surfaces are given by the up-down asymmetric Miller flux surfaces. For $r > \xi \cdot a$, a linear distance assimilation with respect to the input separatrix is performed:

$$\vec{\gamma_r}(\vartheta) = \alpha_L(r, \vartheta) \cdot \left[\begin{pmatrix} R_m(r, \vartheta) \\ Z_m(r, \vartheta) \end{pmatrix} - \begin{pmatrix} R_0(r) \\ Z_M \end{pmatrix} \right] + \begin{pmatrix} R_0(r) \\ Z_M \end{pmatrix} \qquad (69)$$

$$\alpha_L(r, \vartheta) = \frac{1}{l(r, \vartheta)} \left[l_c(\vartheta) + \left(\frac{l_s(\vartheta) - l_c(\vartheta)}{l_m(\vartheta) - l_c(\vartheta)} \right) \cdot (l(r, \vartheta) - l_c(\vartheta)) \right] \qquad (70)$$

with

$$l(r, \vartheta) = \left\| \begin{pmatrix} R_m(r, \vartheta) \\ Z_m(r, \vartheta) \end{pmatrix} - \begin{pmatrix} R_0(r) \\ Z_M \end{pmatrix} \right\|_2 \; , \quad l_s(\vartheta) = \left\| \begin{pmatrix} R_s(\vartheta) \\ Z_s(\vartheta) \end{pmatrix} - \begin{pmatrix} R_{\mathrm{maj}} \\ Z_M \end{pmatrix} \right\|_2$$

$$l_c(\vartheta) = l(\xi \cdot a, \vartheta) \; , \qquad l_m(\vartheta) = l(a, \vartheta) \qquad (71)$$

where $\alpha_L(r, \vartheta)$ is the length rescale factor that adjusts the distances between the geometric middle point and the flux surface so that the shape of the separatrix is assimilated as $r \to a$. The reshaping is centered around the geometric middle point $(R_0(r), Z_M)$, which directly implies a reshaping independent of the shift of $R_0(r)$. Moreover, the distance-based assimilation for fixed ϑ is the most basic choice for a pure geometric assimilation. Finally, the cut-off parameter has to be small enough so that the flux surfaces are nested; at least the area enclosed by $\vec{\gamma}^{\mathrm{SEP}}$ has to contain $\vec{\gamma}_{\xi \cdot a}^{\mathrm{AMS}}$. However, choosing ξ too low will result in strangely shaped flux surfaces near the magnetic axis, while choosing ξ too large will result in a vanishing assimilation zone and therefore in diverging magnetic fields. The default choice in the Profile Creator code is $\xi = 0.6$. In addition, the constant assimilation factor could be replaced by a polynomial of degree greater 0, which would also allow to set $\xi = 0$:

$$\alpha_L(r, \vartheta)|_{\xi=0} = \left(\frac{l_s(\vartheta) - l_m(\vartheta)}{l_m(\vartheta)^{n+1}} \right) \cdot l(r, \vartheta)^n + 1 \tag{72}$$

where $n \geqslant 0$ is the degree of the assimilation polynomial. One can directly see that equation 70 is equivalent to an assimilation polynomial of degree 0. While $\xi = 0$ implies smooth transitions, the higher order assimilation polynomials might squeeze the flux surfaces near the separatrix. However, $\xi = 0$ with $n = 1$ might also be a considerable geometric assimilation.
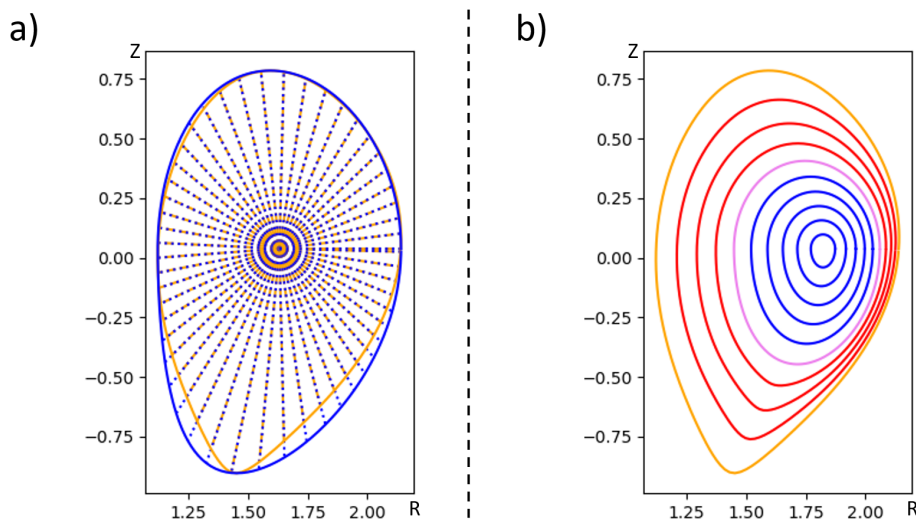
a)   b)

Figure 15: Assimilated flux surfaces for shot AUG33173 created from equation 70 with $\xi = 0.6$. Orange: Input separatrix, Blue: Up-down asymmetric Miller flux surfaces, Violet: Surface at $r = \xi \cdot a$, Red: Assimilated flux surfaces. Dashed/Dotted: Distances from geometric middle point $(R_0(r), Z_M)$. a) Comparison of up-down asymmetric Miller separatrix and input separatrix showing distance deviations, b) Set of assimilated flux surfaces.

Figure 15 shows the set of flux surfaces created from equation 70. To summarize, we defined a fast simple geometric assimilation procedure based on Miller flux surfaces that preserves area and volume of the input separatrix in addition to the shaping moments δ and κ. Hence, the resulting set of flux surfaces is replacing the equations 57 and 58 in the section 3.2.1.

3.3 Edge current density profile

3.3.1 Initial edge current density estimate

In order to calculate the poloidal flux, information on the current density profile is needed. However, the EPED and bootstrap models already require equilibrium profiles in poloidal flux coordinates $\psi(r)$. Thus, the initial current density profile $j(r)$ has to be estimated. At first, we use the pedestal width scaling from the EPED model and translate the width in normalized flux coordinates w to a half-width in spatial coordinates w_r to be used in a Gaussian peak later:

$$w_r \approx \frac{a}{2} \cdot \left[1 - \sqrt{1 - 2w}\right] \tag{73}$$

In the above estimate, we assumed that the peak width is $2w$ and that $r \sim \sqrt{\psi_N}$. The bootstrap current peak density is roughly estimated by the low collisionality limit [1]:

$$j_{\mathrm{BS}} \approx \sqrt{\frac{a}{R_{\mathrm{maj}}}} \cdot \frac{1}{\langle B_{\mathrm{pol}} \rangle} \cdot \frac{\Delta p}{\Delta r} \tag{74}$$

with the pressure gradient $\frac{\Delta p}{\Delta r}$ approximated by

$$\left.\frac{\Delta p}{\Delta r}\right|_{\mathrm{ped,mid}} \approx \frac{p_{\mathrm{ped}}}{1.5 \cdot w_r} \quad , \quad \left.\frac{\Delta p}{\Delta r}\right|_{\mathrm{ped,top}} \approx \frac{p_{\mathrm{av}} - p_{\mathrm{ped}}}{a} \tag{75}$$

where p_{ped} is the pedestal top pressure, given as input to IPED, and p_{av} is the average pressure, determined by equation 49 (page 18). Then, we define the edge current estimate as

$$\langle j_{\mathrm{tor,ped}} \rangle_A (r) \equiv j_{\mathrm{BS,top}} + j_{\mathrm{BS,peak}} \cdot \exp\left(-\frac{(r - (a - w_r))^2}{w_r^2}\right) \tag{76}$$

with

$$j_{\mathrm{BS,top}} = \max\left\{0, \left. j_{\mathrm{BS}}\right|_{\mathrm{ped,top}}\right\}$$

$$j_{\mathrm{BS,peak}} = \max\left\{0, \left. j_{\mathrm{BS}}\right|_{\mathrm{ped,mid}} - \left. j_{\mathrm{BS}}\right|_{\mathrm{ped,top}}\right\} \ .$$

Finally, the edge current cutoff is set to $r_{\mathrm{ped}} \equiv a - 2w_r$.

3.3.2 Edge current density from bootstrap current models

For an edge current density obtained from the Sauter or Redl model $\langle j_\parallel \rangle_B = \sigma_{\mathrm{neo}} \langle E_\parallel \rangle_B + \langle j_{\parallel,\mathrm{BS}} \rangle_B$, the area-averaged edge current density is given by:

$$\boxed{\langle j_{\mathrm{tor,ped}} \rangle_A = \frac{\sigma_{\mathrm{neo}} U_{\mathrm{loop}}}{2\pi \langle R \rangle_A} + \frac{\langle R \rangle_A}{R_M} \cdot \langle j_{\parallel,\mathrm{BS}} \rangle_B \quad , \quad \langle R \rangle_A = \frac{\partial_A V}{2\pi}} \tag{77}$$

where U_{loop} is the applied loop voltage and we used

$$\langle \ldots \rangle_B = \frac{1}{B_T} \partial_V \int \ldots \cdot B \ 2\pi R \mathrm{dA} \approx 2\pi R_M \ \partial_V A \ \partial_A \int \ldots \mathrm{dA} = \frac{R_M}{\langle R \rangle_A} \langle \ldots \rangle_A \tag{78}$$

In addition, we approximated $\langle 1/R \rangle_A \approx 1/\langle R \rangle_A$ for the Ohmic current density as well as $\langle j_\parallel \rangle_A \approx \langle j_{\mathrm{tor}} \rangle_A$ and $E_\parallel = U_{\mathrm{loop}}/(2\pi R)$.

The obtained edge current density (equation 77) usually has a peak near the pedestal top. The onset of this peak, being equivalent to the edge current cutoff r_{ped}, is defined to be at $\tilde{\psi}_{\mathrm{ped}} = 2\tilde{\psi}_{\mathrm{peak}} - 1$ with the peak localized at $\tilde{\psi} = \tilde{\psi}_{\mathrm{peak}}$.

3.4 Current density profile creation

In this section, we create a current density profile $\langle j_{\text{tor}} \rangle_A$ based on a prescribed edge current density $\langle j_{\text{tor,ped}} \rangle_A$ that is either given by the edge current estimate (equation 76) or calculated from a bootstrap current model (equation 77). Analogously to the EPED framework, this is done by using simple model functions for the core current density profiles. While the edge current density is well described by the combination of bootstrap and Ohmic current, the core current density is significantly affected by further phenomena like current diffusion and current driving heating sources. However, the direct influence of the precise core current density shape on the pedestal stability is assumed to be small, because ELMs are almost edge localized. For this reason, instead of rigorously calculating the core current density, the core current density might be modeled with simple functions that obey certain boundary conditions. Nevertheless, we will show that there is an indirect influence of the core current density shape on the pedestal stability caused by the change in total poloidal flux.

Four different core current shapes were implemented in IPED 2. The core current shapes $\widehat{j}_{\text{tor,core}}^{\widehat{j}_0, \widehat{j}_{\text{av}}}$ are defined in normalized area coordinates $x \in [0, 1]$ and obey the following boundary conditions

$$\widehat{j}_{\text{tor,core}}^{\widehat{j}_0, \widehat{j}_{\text{av}}}(0) = \widehat{j}_0 \ , \quad \widehat{j}_{\text{tor,core}}^{\widehat{j}_0, \widehat{j}_{\text{av}}}(1) = 0 \quad \text{as well as} \quad \int_0^1 \widehat{j}_{\text{tor,core}}^{\widehat{j}_0, \widehat{j}_{\text{av}}}(x) \mathrm{d}x = \widehat{j}_{\text{av}} \ .$$

The choice of coordinates directly implies that the core model functions and thus the core flux are stable with respect to the iteration loop, since x is current-independent, meaning that there is no need of convergence for the core current profile. In the following, the implemented core current shapes are introduced:

- **Parabolic model**: No additional boundary conditions

$$\widehat{j}_{\text{tor,core}}^{\widehat{j}_0, \widehat{j}_{\text{av}}}(x) = \left(3\widehat{j}_0 - 6\widehat{j}_{\text{av}} \right) \cdot x^2 - \left(4\widehat{j}_0 - 6\widehat{j}_{\text{av}} \right) \cdot x + \widehat{j}_0 \tag{79}$$

- **Quartic model**: Flattened at $x = 1$

$$\widehat{j}_{\text{tor,core}}^{\widehat{j}_0, \widehat{j}_{\text{av}}}(x) = \left(2.5\widehat{j}_0 - 7.5\widehat{j}_{\text{av}} \right) \cdot (1 - x)^4 - \left(1.5\widehat{j}_0 - 7.5\widehat{j}_{\text{av}} \right) \cdot (1 - x)^2 \tag{80}$$

- **Power model**: Positive and monotonously decreasing, Flattened at $x = 0$

$$\widehat{j}_{\text{tor,core}}^{\widehat{j}_0, \widehat{j}_{\text{av}}}(x) = -\widehat{j}_0 \cdot (x^s - 1) \ , \quad s = \left[1 - \frac{\widehat{j}_{\text{av}}}{\widehat{j}_0} \right]^{-1} - 1 \tag{81}$$

- **Double power model**: Positive and monotonously decreasing, Flattened at $x \in \{0, 1\}$

$$\widehat{j}_{\text{tor,core}}^{\widehat{j}_0, \widehat{j}_{\text{av}}}(x) = \widehat{j}_0 \cdot (x^{2s} - 2x^s + 1) \tag{82}$$

$$s = -\frac{3\widetilde{s} + 3 + \sqrt{(3\widetilde{s} + 3)^2 - 8\widetilde{s} \cdot (\widetilde{s} + 1)}}{4\widetilde{s}} \ , \quad \widetilde{s} = \frac{\widehat{j}_{\text{av}}}{\widehat{j}_0} - 1$$
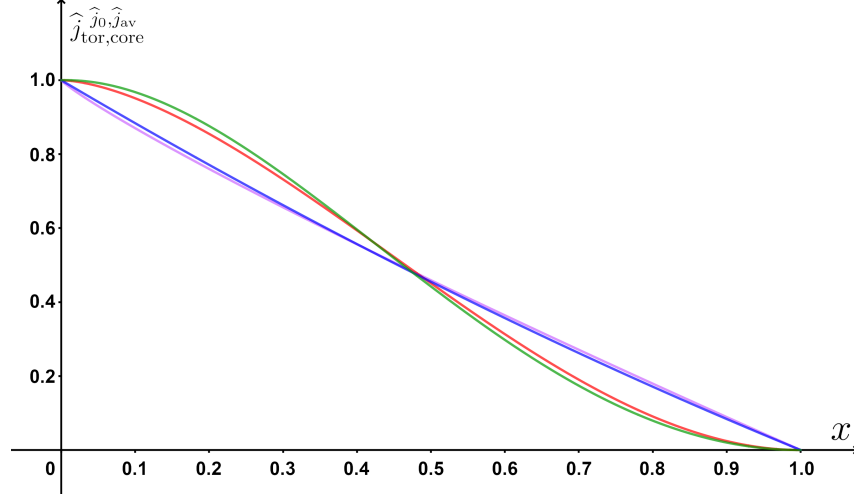
Figure 16: Core current shapes for $\widehat{j}_0 = 1$ and $\widehat{j}_{av} = 0.47$. Blue: Parabolic, Green: Quartic, Violet: Power, Red: Double Power.

The parabolic core current profile is equivalent to the core current density used by IPED 1 (see equation 56 on page 21). Figure 16 shows the different core current shapes. While they behave similar for intermediate ratios $\widehat{j}_{av}/\widehat{j}_0 \sim 0.5$, their behavior differs for $\widehat{j}_{av}/\widehat{j}_0 \to \{0 \text{ or } 1\}$. It has to be remarked that the power and double power profiles are only valid for $\widehat{j}_{av}/\widehat{j}_0 \in (0, 1)$, which limits their usability.

Finally, the total current profile can be assembled from the pedestal and core current densities:

$$\langle j_{tor} \rangle_A (r) = \begin{cases} \widehat{j}^{\,\widehat{j}_0, \widehat{j}_{av}}_{tor,core} \left(\frac{A(r)}{A(r=r_{ped})} \right) + j_{ped}(r = r_{ped}) & \text{for } r < r_{ped} \\[2ex] j_{ped}(r) & \text{for } r \geqslant r_{ped} \end{cases} \tag{83}$$

with

$$\widehat{j}_0 = j_0 - j_{ped}(r = r_{ped}) \quad , \qquad \widehat{j}_{av} = \frac{I_P - I_{ped} - I_0}{A(r = r_{ped})}$$

$$I_{ped} = \int_{r_{ped}}^{a} j_{ped} \cdot \partial_r A \, dr \quad , \qquad I_0 = j_{ped}(r = r_{ped}) \cdot A(r = r_{ped})$$

where $j_{ped} \equiv \langle j_{tor,ped} \rangle_A$ and the edge current density is truncated at r_{ped}. The axis current density is initially given by

$$j_0 = \frac{2B_T}{\mu_0 q_0 R_0(0)} \tag{84}$$

but adjusted twice during the equilibrium profile estimation as described in the following section, where the default axis safety factor is set to the value used by the EPED framework of $q_0 = 1.05$ [13]. To summarize, the resulting total current density profile retains the prescribed pedestal current while satisfying $\langle j_{tor} \rangle_A (0) = j_0$ as well as an integrated total current of $I_{tot} = I_P$ for a set of core current shapes.

3.5 Poloidal flux and safety factor calculations

The area-averaged current density profile generates a poloidal flux within the estimated flux surface geometry (section 3.2). Using Ampère's law and equation 62, the

poloidal magnetic field and flux are given by:

$$B_{\text{pol}}(r, \varphi) = \mu_0 \cdot I(r) \cdot b_{\text{var}}(r, \varphi) \ , \quad I(r) = \int_0^r \langle j_{\text{tor}} \rangle_A \cdot \partial_r A \ \mathrm{d}r \tag{85}$$

$$\psi(r) = \int_0^r B_{\text{pol}}(r, \varphi) \cdot \partial_r A_{\text{pol}}(r, \varphi) \ \mathrm{d}r \quad \forall \varphi \in [0, 2\pi] \tag{86}$$

By construction (see equation 61), the poloidal flux in equation 86 is well-defined. The flux profile is bijective only if the current profile $I(r)$ has no zeros, which is usually fulfilled. Then, r and ψ can be used to describe the radial variations equivalently. With the results from equation 59, this directly grants the geometrical profiles $V(\psi)$, $A(\psi)$ and $r(\psi)$. Interpolating the magnetic field to polar coordinates, it is also possible to calculate the spatially resolved current density:

$$j_{\text{tor}} = \frac{1}{\mu_0} \cdot \left(\vec{\nabla}_{2D} \times \vec{B}_{\text{pol}} \right) \ , \quad \frac{\vec{B}_{\text{pol}}}{B_{\text{pol}}} = \frac{\partial_\varphi \vec{\gamma}_r(\varphi)}{\|\partial_\varphi \vec{\gamma}_r(\varphi)\|_2} \tag{87}$$

For estimation of the toroidal magnetic field $B_{\text{tor}} = F(\psi) \cdot R^{-1}$, we roughly approximate $F(\psi)$ from the Grad-Shafranov equation:

$$\frac{\mathrm{d}F^2}{\mathrm{d}\psi} = \mathrm{d}_\psi \langle F^2 \rangle \approx 2\mu_0 \left(\frac{\langle R \rangle \langle j_{\text{tor}} \rangle}{2\pi} - \langle R \rangle^2 \, \mathrm{d}_\psi p \right) \ , \quad F(\psi(a)) = R_M B_T \tag{88}$$

Since there is no information on $\mathrm{d}_\psi p$ before the second loop iteration (see figure 12b), the toroidal magnetic field is approximated by the vacuum toroidal magnetic field in these cases, i.e. $F(\psi) \equiv R_M B_T$. Two different approaches were implemented to calculate the safety factor profile q as IPED 2 developed. The first is based on a flux derivative, the second approach tracks the field line for one poloidal turn and counts the number of toroidal turns:

$$q(\psi) = \frac{\mathrm{d}\phi}{\mathrm{d}\psi} \qquad\qquad , \phi = \int_0^r B_{\text{tor}}(r) \cdot \partial_r A(r) \ \mathrm{d}r \tag{89}$$

$$q(r) = \frac{1}{2\pi} \int_0^{2\pi} \partial_{C_r} \Phi \cdot \partial_\varphi C_r(\varphi) \ \mathrm{d}\varphi \qquad , \partial_{C_r} \Phi = \frac{1}{R(r, \varphi)} \cdot \frac{B_{\text{tor}}(r, \varphi)}{B_{\text{pol}}(r, \varphi)} \tag{90}$$

both yielding equivalent results. Moreover, assuming sufficiently smooth profiles, we can approximate the axis safety factor by:

$$q(0) = \lim_{\psi \to 0} \frac{\phi(\psi)}{\psi} = \lim_{r \to 0} \frac{\phi(r)}{\psi(r)} \approx \frac{B_{\text{tor}}(0)}{j_0} \cdot \text{const.} \tag{91}$$

where $j_0 = \langle j_{\text{tor}} \rangle_A (0)$ and *const.* is a constant depending on the fixed set of flux surfaces only. The axis current density j_0 is a free parameter in the current profile creation and might be chosen so that $q(0)$ equals a given fixed value q_0. As mentioned in the previous section, the initial current density is estimated by the circular flux surface case $j_0 = (2B_T) \cdot (\mu_0 q_0 R_0(0))^{-1}$. However, shaping and the Shafranov shift can influence this relation. For this reason, we define the axis current scale:

$$C_j = \frac{q(0)}{q_0} \tag{92}$$

Therefore, following approximation 91, we can adjust $j_0 \overset{\text{adjust}}{\to} C_j \cdot j_0$ so that $q(0) = q_0$, where C_j only depends on shaping. This is called "j_0 adjustment" in figure 12b and performed twice during profile creation. Initially, after the first calculation of $q(\psi)$ using the current profile estimate, and secondly, after the first adjustment of the toroidal field B_{tor} using equation 88. The second adjustment is usually small. Nevertheless, it is necessary since the axis current adjustment is based on the assumption that $B_{\text{tor}}(0)$ is constant, which is significantly violated at this step. Both determined axis current scales are indexed as $C_j^{(i)}$ where $i = 1, 2$ is their respective index. Finally, the corrected axis current j_0 granting $q(0) = q_0$ is given by

$$j_0 = \left(\prod_i C_j^{(i)} \right) \cdot \frac{2 B_T}{q_0 \mu_0 R_0(0)} \tag{93}$$

where the product is over all previously determined axis current adjustments $C_j^{(i)}$. The empty product is set to 1.

After calculation of the safety factor and poloidal flux profiles, temperature and density profiles are generated by the EPED1 model and edge current densities are obtained from the bootstrap current models. Subsequently, the resulting current density profile is used to recalculate the poloidal flux and safety factor profiles. This is repeated until the current profile has converged.

3.6 Convergence and verification

In the previous sections of this chapter, we defined an iterative process to obtain a self-consistent current density profile with respect to a fixed flux surface geometry that embeds both the EPED model and a model for the bootstrap current. However, it remains to define and discuss convergence of the current density profile and to compare the equilibrium estimate to the equilibrium profiles calculated by the HELENA code.

To define convergence, we have to measure differences between current density profiles and thus introduce an appropriate metric. Firstly, it is natural to compare the profiles on a fixed domain. Since spatial coordinates are independent of other quantities, we will define convergence for current density profiles in spatial coordinates, which are in this section simply referenced as j. An established measure for local differences between bounded functions is the L^∞-norm $\| \cdot \|_\infty$. To get a scale-independent metric, we define a normalized distance between j and $\tilde{j}$ as:

$$d_\infty(j, \tilde{j}) = \frac{\| j - \tilde{j} \|_\infty}{I_P / A |_{r=a}} \tag{94}$$

A rigorous proof of convergence for the defined iteration procedure would require to show that the loop, represented by a non-linear operator mapping the current profile at iteration step n to the next current profile at step $n + 1$, converges to fix point. However, properly defining the loop operator or rigorously proofing convergence to a fix point is challenging. For this reason, we will instead discuss the observed convergence properties based on performed runs.
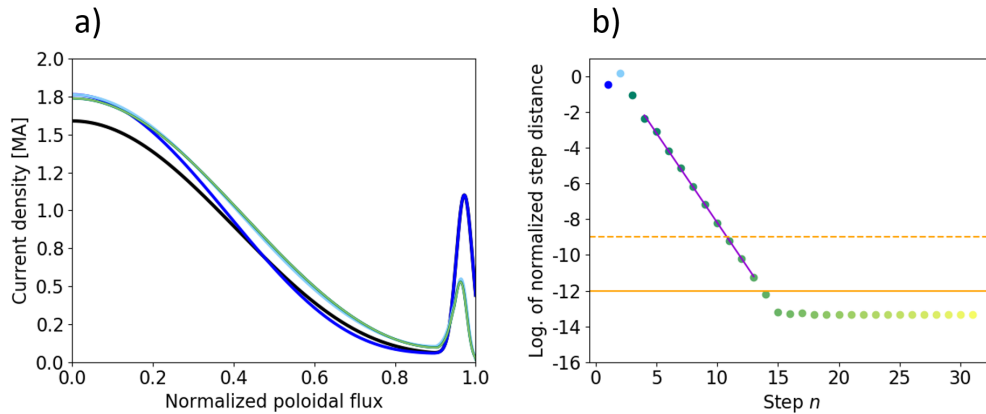
Figure 17: Typical convergence process of the iterative equilibrium estimation procedure. Black: Initial current density estimate with low collisionality bootstrap current (1st "Current density estimate" in figure 12b on page 23), Dark blue: Current density estimate after the first "j_0 adjustment" with low collisionality bootstrap current (2nd "Current density estimate" in figure 12b), Light blue: Current density before the second "j_0 adjustment" with Sauter or Redl model bootstrap current (1st iteration in figure 12b), Green: Current density profiles of the further iterations, where a brighter color indicates a higher iteration step n (visually nearly indistinguishable). a) Convergence of the current profile. b) Decadic logarithm of the normalized step distance $d_\infty(j^{(n)}, j^{(n-1)})$ for the n-th iteration step. The dashed horizontal line marks the numerical convergence threshold, the solid horizontal line marks the numerical resolution limit. The purple line is a linear fit to the iteration steps $n > 3$ up to the numerical resolution limit, indicating exponential convergence.

The convergence process of a current density profile is illustrated in figure 17a and figure 17b shows the decadic logarithm of the normalized step distance $d_\infty(j^{(n)}, j^{(n-1)})$ for the n-th iteration step. For a broad range of parameter sets, the normalized step distance is observed to decrease roughly exponentially after the toroidal field correction (equation 88), i.e. for $n > 3$. Nevertheless, rare exceptions from this behavior were observed, where for high core pressures, the EPED model might create a "spike" in the derivative of the temperature profile (see figure 18a) which implies a disturbance of the bootstrap current at the position of the spike. This disturbance of the edge current is sometimes observed to prohibit convergence with respect to the comparably strict convergence norm $\| \cdot \|_\infty$ because the "spike" (numerically) trembles around the edge cutoff at $r = r_{\text{ped}}$. The "spike" is a direct consequence of the analytical definition of $T_{\text{core}}(\tilde{\psi})$ (equation 45 on page 18). Finally, one can see that a numerical precision limit is reached around $d_\infty(j^{(n)}, j^{(n-1)}) \sim 10^{-12}$.

We assume a profile to be converged after $N \geqslant 3$ steps if:

$$\boxed{d_\infty(j^{(N)}, j^{(N-1)}) < 10^{-9} \Leftrightarrow \text{Converged}} \tag{95}$$

Assuming that the exponential decrease of the normalized step distance, as shown in figure 17b, holds for $n \to \infty$, we can estimate the relative approximation error
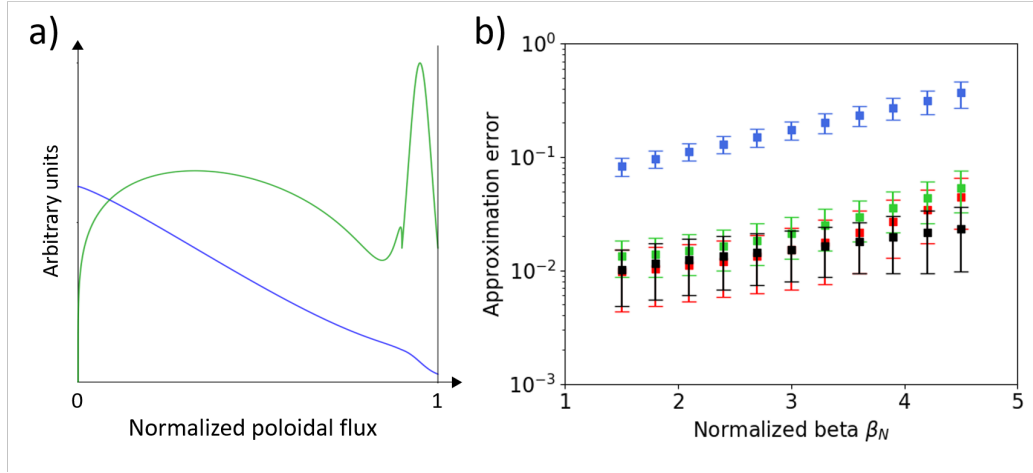
Figure 18: a) EPED temperature profile (blue) created using equation 44 (page 17) and its derivative $\partial_{\tilde{\psi}}T$ (green) for the parameters $a_{T1} = 1$, $a_{T0} = 0.1$ and $\Delta = 0.1$, showing a "spike" at the pedestal top location.

b) Approximation error as defined in equation 98 of the minor radius profile $r(\tilde{\psi})$ (black), area profile $A(\tilde{\psi})$ (green), volume profile $V(\tilde{\psi})$ (red) and safety factor profile $q(\tilde{\psi})|_{0.8a \leqslant r \leqslant a}$ (blue). Every data point represents approximation errors for AUG, DIII-D and ITER like equilibrium estimates by IPED 2 (see appendix B.2 "Parameter sets") for densities $n_{\mathrm{e,ped}} = 2,\ 6,\ 10\ [10^{19}\ \mathrm{m}^{-3}]$ and pressures from 10 to 35 kPa or 30 to 150 kPa for the AUG/DIII-D or ITER like case, respectively; the error bars display the standard deviation of the approximation error.

of the converged solution $j^{(N)}$ relative to the true limit $j^* = \lim\limits_{n \to \infty} j^{(n)}$, which is the true self-consistent solution, by:

$$\|j^{(N)} - j^*\|_\infty \leqslant \sum_{n \geqslant N} \|j^{(n+1)} - j^{(n)}\|_\infty \approx \sum_{n \geqslant N} c_1 \cdot e^{-c_2 n} \leqslant$$

$$\leqslant \int_{N-1}^{\infty} c_1 \cdot e^{-c_2 n} \mathrm{dn} \approx \frac{\|j^{(N)} - j^{(N-1)}\|_\infty}{c_2}$$

$$\Rightarrow \boxed{d_\infty(j^{(N)}, j^*) < \frac{10^{-9}}{c_2}} \tag{96}$$

with the approximation

$$\|j^{(n+1)} - j^{(n)}\|_\infty \approx c_1 \cdot e^{-c_2 n} \tag{97}$$

where c_1 can be interpreted as a measure for the quality of initial estimate and c_2 is an approximation speed that, for the observed parameter space, is roughly bounded by $0.5 \leqslant c_2 \leqslant 3$. Thus, in the limits of the approximation error, the converged solution is self-consistent with respect to the fixed flux surface geometry.

Equally important, a benchmark that rates the converged equilibrium estimate of IPED 2, i.e. $V(\psi)$, $A(\psi)$, $r(\psi)$ and $q(\psi)$, against the Grad-Shafranov solution given by the HELENA code has to be performed. For this reason, we introduce a new approximation error $\delta_2 f$ measuring a normalized global deviation between the IPED

2 estimated profile f_{IPED} and its respective HELENA solution f_{HEL} based on the L^2-norm $\|\cdot\|_2$ in normalized poloidal flux coordinates

$$\delta_2 f = \frac{\|f_{\text{HEL}} - f_{\text{IPED}}\|_2}{\|f_{\text{HEL}}\|_2} \tag{98}$$

where $f \equiv V, A, r, q$. Here, the global L^2-norm was chosen over the local L^∞-norm, because we are interested in the global deviation of the equilibrium profiles, especially for the area and volume profiles which are used to normalize the pressure profile and the current density profile. The approximation error of the safety factor profile is restricted to the pedestal, here roughly defined as $0.8a \leqslant r \leqslant a$, since the safety factor only influences the equilibrium estimate through the bootstrap model, i.e. through the edge current density.

Figure 18b shows the approximation error of the equilibrium profiles over a range of normalized betas, where each data point represents approximation errors for AUG, DIII-D as well as ITER like equilibrium estimates generated by IPED 2. One can see that the approximation error increases with increasing normalized beta. However, while the errors for the geometric profiles are below 3% for $\beta_N \leqslant 3$, the error of the safety factor is roughly one order of magnitude larger. Typical safety factor profiles generated by IPED 2 and their respective HELENA solutions are displayed in figure 19. It is supposed that the relatively large error of the safety factor is related to the rough approximation in equation 88 (page 32), which is not a proper solution of the force balance. Furthermore, because $\delta_2 q \not\ll 1$, the effect of deviations of the safety factor on the equilibrium estimate was examined numerically and analytically. Firstly, the numerical analysis was performed for AUG and DIII-D like scenarios by substitution of $q \to (1 + \delta q) \cdot q$ into equation 36 (page 15), where δq is the uniform/local deviation of the safety factor, and covered (unperturbed) collisionalities up to $\nu_{e,*} \approx 30$. As a result, deviations of $\delta q = \pm 20\%$ implied changes to the bootstrap current peak value of $\leqslant 0.1\%$ at low collisionalities up to $\sim 18\%$ at the highest collisionalities. In contrast, the effect on the total poloidal flux was generally less than 1%. It is proposed that the effect on the poloidal flux is low, because deviations of q mainly affect the relatively small high-collisionality edge current density, which
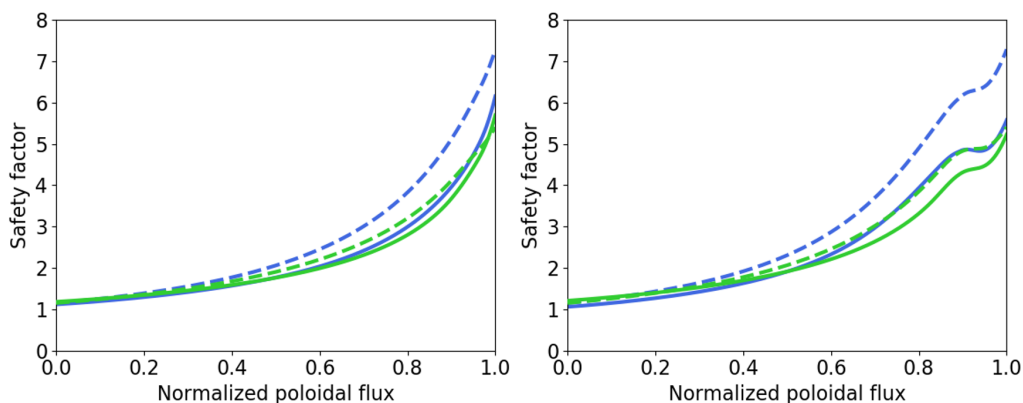

Figure 19: Safety factor profiles generated by IPED 2 (dashed) and their respective HELENA solutions (solid) for an AUG like scenario with $\kappa = 1.6$, $\delta = 0.4$ and $n_{\text{e,ped}} = 6 \cdot 10^{19}$ m^{-3} (see B.2 "Parameter sets"). Green: $\beta_N = 1.8$, Blue: $\beta_N = 3.6$. Left: $p_{ped} = 10$ kPa, Right: $p_{ped} = 35$ kPa.

3.6 Convergence and verification

has little influence on the integrated core current $I_{\text{core}} = I_P - I_{\text{ped}}$ and thus on the total poloidal flux. Secondly, to make analytical progress, the bootstrap current is roughly approximated by $j_{\text{BS}} \sim 1/(1 + \sqrt{\nu_{e,*}} + c_Z \nu_{e,*})$ with $c_Z \equiv (2Z_{\text{eff}})^{-2}$ (see [46]). Then, using $\delta\nu_{e,*} = \delta q$, the non-linear error propagation yields:

$$|\delta j_{\text{BS}}| = \frac{|\sqrt{\nu_{e,*}}(1 - \sqrt{1 + \delta q}) - c_Z \nu_{e,*}\, \delta q|}{1 + \sqrt{\nu_{e,*}(1 + \delta q)} + c_Z \nu_{e,*}(1 + \delta q)} \rightarrow \begin{cases} |\delta q|/(1 + \delta q) & \text{for } \nu_{e,*} \to \infty \\ \\ 0 & \text{for } \nu_{e,*} \to 0 \end{cases} \tag{99}$$

From this, one can see that in general the non-linear error propagation decreases with increasing effective charge or decreasing collisionality. Inserting the parameters of the most liming case that was numerically analyzed ($Z_{\text{eff}} = 1.3$ and $\nu_{e,*} = 30$) results in $|\delta j_{\text{BS}}| \approx 16\%$, which is close to the result obtained from the numerical analysis of $|\delta j_{\text{BS}}| \approx 18\%$. In conclusion, the error of the safety factor profile might be treated as an error of the edge current density that is roughly described by equation 99, whereas the effect on the total poloidal flux and thus on the gradients ∂_ψ is generally small.

Finally, to rate the flux surface assimilation procedure introduced in section 3.2.2, the approximation errors using the separatrix and plasma parameters from AUG Shot 33173 were determined. The resulting approximation errors, comparing IPED 2 and HELENA in the case of a prescribed input separatrix, are $\delta_2 V \approx 0.9\%$, $\delta_2 A \approx 1.5\%$, $\delta_2 r \approx 1.6\%$ and $\delta_2 q \approx 15\%$, where $\beta_N = 2.2$, which aligns with the results presented in figure 18b.

4 Results from IPED 2.0

In this chapter, the newly implemented IPED 2 framework is used to study MHD stability in both the p-n space as well as the s-α space. Firstly, in section 4.1, an attempt is made to reproduce the DIII-D Super H solution predicted by the EPED-ELITE framework (see [15]). Moreover, the influence of the core current density, the bootstrap current and certain EPED model parameters on the stability boundary was examined. Then, in section 4.2, trends of the stability boundary as well as a scaling for the critically stable pedestal top pressure are presented, where we used AUG like plasma parameters including negative triangularity scenarios.

This paragraph shortly summarizes the creation procedure of the stability diagrams. Following sections 2.1 and 2.2, we define a single IPED 2 scanned point or profile set, identified by its pedestal top pressure and density, to be MHD stable if (see [17]):

$$\gamma_{\mathrm{MHD}} \leqslant \gamma_{\mathrm{thr}} \qquad\qquad \Leftrightarrow \quad \text{Ideally stable} \qquad\qquad (100)$$

$$\gamma_{\mathrm{MHD}} \leqslant \gamma_{\mathrm{thr}} \ \& \ \gamma_{\mathrm{MHD}} < \frac{1}{2} \cdot \omega_{*,i}^{\mathrm{eff}} \quad \Leftrightarrow \quad \text{Diamagnetically stable} \qquad (101)$$

where γ_{thr} is a numerical threshold for the normalized growth rate and $\omega_{*,i}^{\mathrm{eff}}$ is either $\omega_{*,i}^{\mathrm{eff1}}$ or $\omega_{*,i}^{\mathrm{eff2}}$ as defined in section 2.2. Following M. G. Dunne and others (see [17]), we set $\gamma_{\mathrm{thr}} \equiv 0.04/\tau_A$ if not otherwise specified, identifying growth rates $\gamma_{\mathrm{MHD}} \leqslant \gamma_{\mathrm{thr}}$ as negligibly small. Then, for $\gamma_{\mathrm{thr}} \equiv 0.04/\tau_A$, the stability boundary $\gamma_{\mathrm{MHD}}(p_{\mathrm{ped}}, n_{\mathrm{e,ped}}) = \gamma_{\mathrm{thr}}$ is created using triangular interpolation between the data points. However, since triangular interpolation yields rough grid-like boundaries for $\gamma_{\mathrm{thr}} \equiv 0$, we create the stability boundaries in this case by connecting the critically stable pressures $\gamma_{\mathrm{MHD}}(p_{\mathrm{ped}}) = \gamma_{\mathrm{thr}}$ for each density. Finally, for all IPED 2 scans, growth rates were calculated for the toroidal mode numbers $n = 1, 3, 5, 6, 8, 10, 15, 20, 25, 30, 35, 40$, where a finer resolution was chosen for the low mode numbers and we included all mode number used in [15]. It can be seen later that the selection of mode numbers is sufficiently dense, meaning that the differences between stability boundaries corresponding to two "adjacent" mode numbers are generally small.

4.1 DIII-D: Search for a Super H mode solution

At first, we try to reproduce the Super H solution predicted by the EPED-ELITE framework (see [15]). For this purpose, all stability boundaries in this section are created using the same input parameters as specified in [15], which are also listed as "DIII-D" in the appendix B.2 "Parameter sets", as well as the Sauter model for calculating the bootstrap current and the parabolic core current model.

Figure 20 shows IPED 2 scans for triangularities $\delta = 0.4$ and $\delta = 0.5$ with $\gamma_{\mathrm{thr}} \equiv 0$ (black boundary) and $\gamma_{\mathrm{thr}} \equiv 0.04/\tau_A$ (blue boundary) in comparison to the Super H solution from EPED-ELITE (green boundary). The "standard" H solution, i.e. the lowest critical pressures, of the EPED-ELITE boundary is well reproduced by the $\gamma_{\mathrm{thr}} \equiv 0$ case. However, although there are multiple IPED 2 scanned points (circles) within the predicted Super H mode region, such a Super H solution is not found with IPED 2. Instead, we observe a "pressure drop" region at intermediate densities connecting the low mode number limited and high mode number limited critical
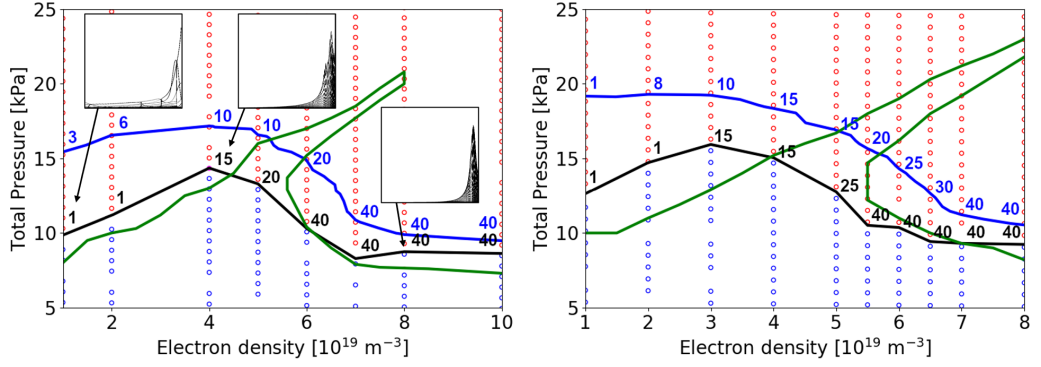
Figure 20: Ideal stability boundaries using DIII-D parameters with $\kappa = 1.89$. Left: $\delta = 0.4$, Right: $\delta = 0.5$. Black boundary: $\gamma_{\text{thr}} \equiv 0$, Blue boundary: $\gamma_{\text{thr}} \equiv 0.04/\tau_A$, Green: Super H mode solution predicted by the EPED-ELITE framework (from [15]). Blue circles: Single IPED2 scanned point with $\gamma_{\text{MHD}} \leqslant 0$, Red circles: Single IPED2 scanned point with $\gamma_{\text{MHD}} > 0$. The numbers denote the most destabilizing toroidal mode numbers at the equally colored stability boundary. For three destabilizing modes, the corresponding mode structure is displayed, where the domain was restricted to $0.8 \leqslant \tilde{\psi} \leqslant 1$.
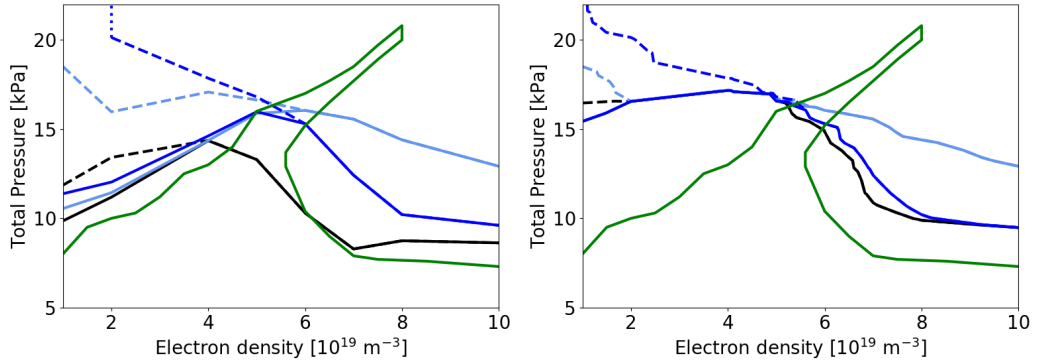

Figure 21: Stability boundaries using DIII-D parameters with $\kappa = 1.89$ and $\delta = 0.4$. Left: $\gamma_{\text{thr}} \equiv 0$, Right: $\gamma_{\text{thr}} \equiv 0.04/\tau_A$. Black: Ideally stable, Light Blue: Diamagnetically stable using $\omega_{*,i}^{\text{eff1}}$, Dark Blue: Diamagnetically stable using $\omega_{*,i}^{\text{eff2}}$, Green: Super H mode boundary from [15]. Solid: All toroidal mode numbers. Dashed: Only $n \geqslant 5$ considered for comparison to [15].

pressures, in the following called "low-n limited boundary" and "high-n limited boundary", respectively. We will conclude later that the high-n limited boundary is destabilized by ballooning modes while the low-n boundary is destabilized by low mode number coupled peeling-ballooning modes or kink/peeling modes (see chapter 5). Consequently, they might also be referred to as the "ballooning" and the "peeling" boundary, respectively. In general, the most destabilizing mode numbers increase with increasing density, where the transition from low to high limiting mode numbers seems to be smoother for $\gamma_{\text{thr}} \equiv 0.04/\tau_A$. Examples for mode structures at the stability boundary are also displayed in figure 20. Furthermore, one can see that there are some gaps between the IPED 2 scanned points. For these equilibria, the corresponding growth rates were identified as numerical defects since MISHKA

failed to calculate real eigenvalues ω^2. Finally, the criterion $\gamma_{\text{thr}} \equiv 0.04/\tau_A$ results in noticeably higher pressures but retains the qualitative shape of the stability boundary.

Next, as shown in figure 21, the effects of different stability conditions on the stability boundary are examined. Diamagnetic stability increases the critical pressures at the high-n limited boundary, whereas the low-n limited boundary is nearly unaffected by diamagnetic stabilization. It is remarked that applying diamagnetic stabilization to low mode numbers is inconsistent anyway, because the diamagnetic stability criterion is only valid for $n \gg 1$ (see section 2.2). For high mode numbers, the linear criterion $\omega_{*,i}^{\text{eff1}}$ has a stronger stabilizing effect compared to the bi-linear criterion $\omega_{*,i}^{\text{eff2}}$, since the latter saturates for $n \cdot q_{95} \geqslant 27.7$ (section 2.2). Furthermore, restricting mode numbers to $n \geqslant 5$ (dashed boundaries) as in [15] implies a small change to the low-n limited boundary for ideal stability. A strong combined stabilization of diamagnetic stability and the restriction to $n \geqslant 5$ is observed at low to intermediate densities n_e, where the high mode numbers n are strongly diamagnetically stabilized $\omega_{*,i} \sim n/n_e$ and the lowest mode numbers are completely ignored. The restriction to $n \geqslant 5$ is inappropriate if it affects the stability boundary, i.e. if the dashed and solid lines in figure 21 split up, which is usually the case at low densities, especially in combination with diamagnetic stabilization. Finally, the qualitative effects of the different stability conditions are equivalent for $\gamma_{\text{thr}} \equiv 0$ and $\gamma_{\text{thr}} \equiv 0.04/\tau_A$. In conclusion, the ideal stability criterion seems to be the best choice for reproducing the "standard" H solution of [15] and we observed no tendencies towards a Super H solution for any of the applied stability criteria.
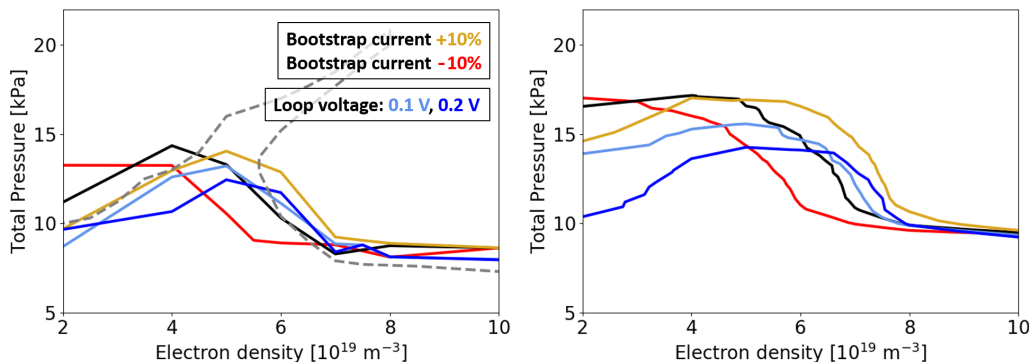

Figure 22: Ideal stability boundaries using DIII-D parameters with $\kappa = 1.89$ and $\delta = 0.4$. Left: $\gamma_{\text{thr}} \equiv 0$, Right: $\gamma_{\text{thr}} \equiv 0.04/\tau_A$. Black: $U_{\text{loop}} = 0$ V, Light Blue: $U_{\text{loop}} = 0.1$ V, Dark Blue: $U_{\text{loop}} = 0.2$ V, Red: Decreased bootstrap current $j_{BS} \to 0.9 \cdot j_{BS}$, Yellow: Increased bootstrap current $j_{BS} \to 1.1 \cdot j_{BS}$, Dashed gray: Super H mode boundary from [15].

As already discussed in section 3.6, there might be differences in the edge current densities between EPED-ELITE and IPED 2 implied by the error of the predicted safety factor δq. For this reason, we will test if this deviation can prevent the prediction of a Super H solution. Assuming that the parameter region of interest, i.e. the region where we expect a Super solution, is $p_{\text{ped}} \geqslant 10$ kPa and $n_{\text{e,ped}} \leqslant 7 \cdot 10^{19}$ m^{-3}, IPED 2 calculates unperturbed collisionalities $\nu_{e,*} \leqslant 1.6$. Then, inserting $|\delta q| \approx 10\%$ for $\beta_N = 1.8$ (see figure 18b on page 35) into equation 99 yields an error propagation to the bootstrap current of $|\delta j_{\text{BS}}| \leqslant 3.1\%$. It is remarked that the largest deviation $|\delta j_{\text{BS}}| = 3.1\%$ is reached only at the lowest pressure and highest den-

sity value considered. The stability boundaries for the most pessimistic scenario $\nu_{e,*} \to \infty \Rightarrow |\delta j_{BS}| \approx 10\%$ are displayed in figure 22, where the bootstrap current (equation 34 on page 14) was modified by a prefactor of 0.9 or 1.1. One can see that the bootstrap current has nearly no effect on the high-n boundary but an increased bootstrap current shifts the "pressure drop" to higher pressures and decreases stability at the low-n boundary. Finally, the effect of applied loop voltage was tested. As a result, increasing loop voltage mainly affects the low-n boundary, where increasing voltage decreases stability, as expected because this region is mainly kink/peeling limited.
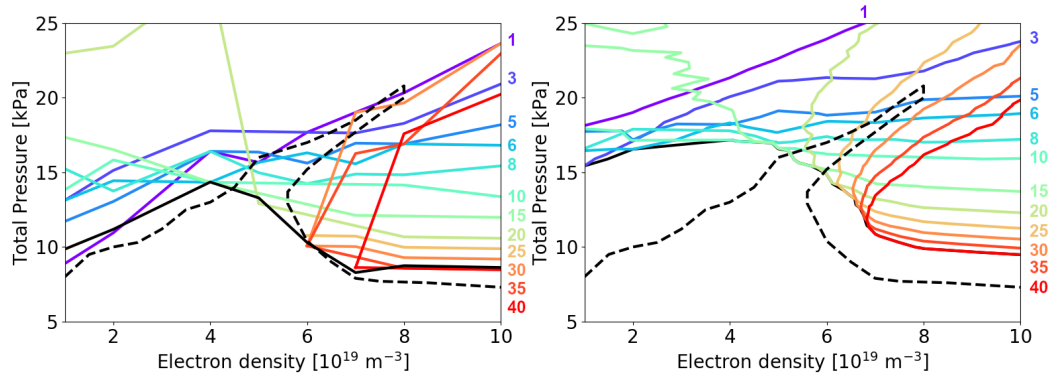

Figure 23: Ideal stability boundaries using DIII-D parameters with $\kappa = 1.89$ and $\delta = 0.4$. Left: $\gamma_{thr} \equiv 0$, Right: $\gamma_{thr} \equiv 0.04/\tau_A$. Colored: Stability boundaries considering only a single toroidal mode number n (see labels in the plot). Solid black: Stability boundary, Dashed black: Super H mode boundary from [15].
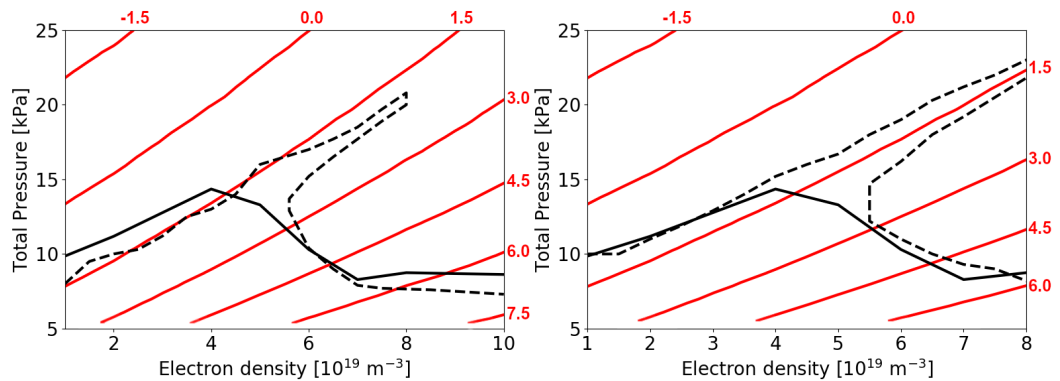

Figure 24: Ideal stability boundaries using DIII-D parameters with $\kappa = 1.89$. Left: $\delta = 0.4$, Right: $\delta = 0.5$. Black boundary: $\gamma_{thr} \equiv 0$, Dashed black: Super H mode boundaries from [15], Red: Lines of constant shear s (see labels) calculated by IPED2-HELENA.

In order to understand why there is no Super H solution using the IPED2-HELENA-MISHKA framework, we look at the stability of every toroidal mode number separately. Figure 23 displays the stability boundaries for every mode number (colored) as well as their envelope (solid black) in comparison to the EPED-ELITE Super H solution (dashed black). Remarkably, the high mode numbers $n \geqslant 30$ perfectly reproduce the lower part of Super H solution and mode number $n = 1$ aligns with the upper part of the Super H solution. However, using the IPED2-HELENA-MISHKA

framework, intermediate mode numbers $n = 8 \sim 20$ block access to the Super H regime. Thus, it would be necessary to strongly stabilize intermediate mode numbers while leaving high mode numbers unaffected to enable the Super H regime described in [15]. Furthermore, in p-n space, low mode number boundaries $n = 1 \sim 8$ are usually nearly straight lines, high mode number boundaries $n \geqslant 30$ form "parabola-like" curves and intermediate mode numbers seem to smoothly transition from the straight line to the parabolic boundary shape. The shapes of the different mode number boundaries are discussed in chapter 5. Both ideal stability criteria $\gamma_{\mathrm{thr}} \equiv 0$ and $\gamma_{\mathrm{thr}} \equiv 0.04/\tau_A$ qualitatively yield the same mode number boundaries, while the triangular interpolation for $\gamma_{\mathrm{thr}} \equiv 0.04/\tau_A$ results in smoother boundaries. Finally, we observed that the Super H solutions from [15] are aligned with the lines of constant shear as shown in figure 24. However, it is remarked that the precise shear values might differ between the EPED and IPED2-HELENA frameworks.
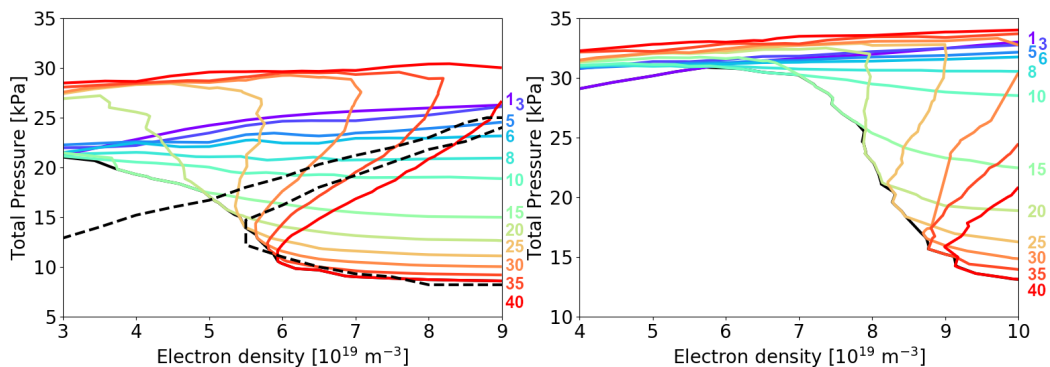

Figure 25: Ideal stability boundaries using DIII-D parameters with $\kappa = 1.89$, $\delta = 0.4$ and $c_\beta = 3$ overriding β_N. Left: $B_T = 1.9$ T and $\delta = 0.5$, Right: $B_T = 2.17$ T and $\delta = 0.6$. Colored: Stability boundaries considering only a single toroidal mode number n (see labels in the plot). Solid black: Stability boundary, Dashed black: Super H mode boundary from [15].

While the Super H solution from EPED-ELITE was not directly reproducible using IPED2, we next try to access the Super H regime deviating from the precise set of input parameters given in [15]. In order to "decouple" high and low mode number boundaries, we used higher triangularities, magnetic fields and "stiff" core pressure profiles, where we fixed c_β instead of β_N. The mode number boundaries for $c_\beta = 3$ and $\delta = 0.5$ as well as for $c_\beta = 3$, $\delta = 0.6$ and $B_T = 2.17$ T are shown in figure 25. Here, the "bunch" of mode number boundaries at $p_{\mathrm{ped}} \approx 30$ kPa is limited by global instabilities, probably caused by the high beta values $\beta_N > 4$ at $p_{\mathrm{ped}} \gtrsim 30$ kPa. However, the stability boundary below $p_{\mathrm{ped}} \approx 30$ kPa is limited by purely edge localized modes. As a result, even for high shaping and magnetic field we observe no "decoupling" of the low and high mode numbers. Finally, the $\delta = 0.6$ and $B_T = 2.17$ T case (figure 25, right) is stable at significantly higher pressures compared to the $\delta = 0.5$ and $B_T = 1.9$ T case (figure 25, left). The stabilizing effect of the magnetic field and triangularity as well as other stability trends are further discussed in the section 4.2.

In the following, we will examine the effects of model details on the stability boundary. Figure 26 shows the dependence of the stability boundary on the different core current profile shapes introduced in section 3.4. While the stability boundaries in the s-α space deviate only noticeably for the different core current models, there are
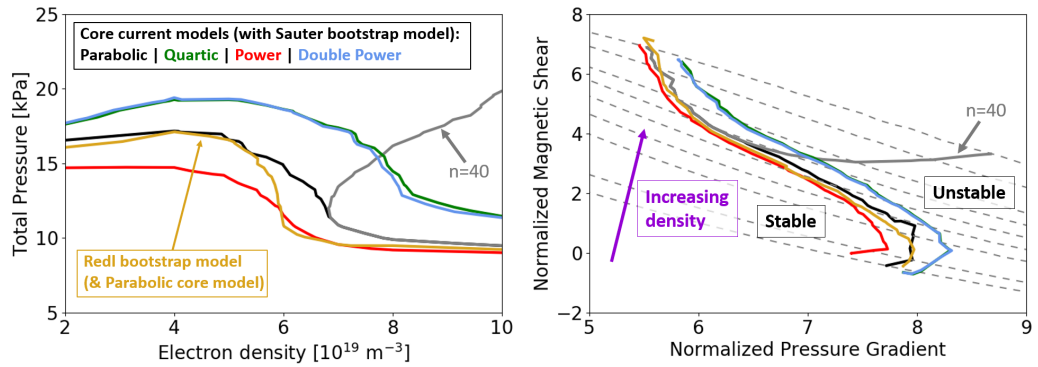
Figure 26: Ideal stability boundaries using DIII-D parameters with $\kappa = 1.89$ and $\delta = 0.4$. Left: p-n space, Right: s-α space. Black: Parabolic core current model, Green: Quartic core current model, Blue: Double power core current model, Red: Power Core current model, Yellow: Parabolic core model with Redl bootstrap current, Solid Gray: Stability boundary for the parabolic core current model considering only $n = 40$, Dashed Gray: Lines of constant density corresponding to the black stability boundary. Note that the lines of constant density might vary for the different stability boundaries but can be seen as a guide for the eye.
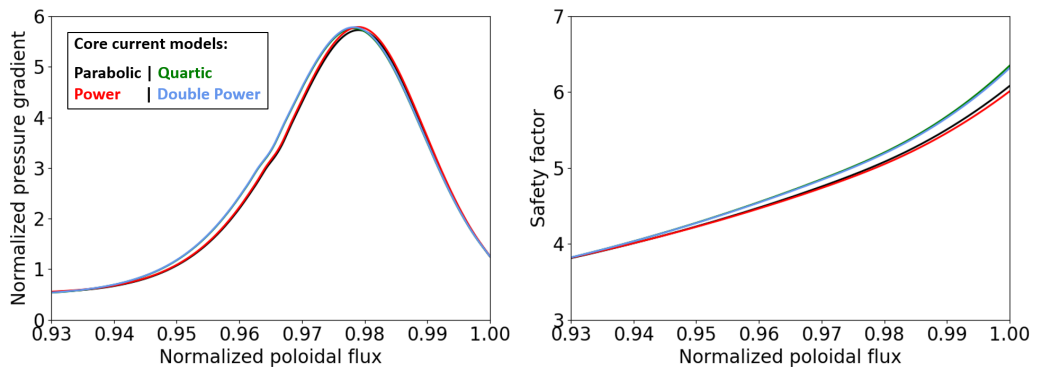

Figure 27: Normalized pressure profiles (left) and safety factor profiles (right) using DIII-D parameters with $\kappa = 1.89$ and $\delta = 0.4$. The profiles belong to a single IPED 2 scanned point and were selected at roughly the same location in s-α space, $s = 5.98 \pm 0.11$ and $\alpha = 5.76 \pm 0.04$, near the stability boundaries. Black: Parabolic core model, Green: Quartic core model, Blue: Double power core model, Red: Power core model. The blue and green profiles are visually nearly indistinguishable.

significant differences between the critical pressures in the p-n space. Normalized pressure and safety factor profiles at equal normalized shear and pressure gradient, $s = 5.98 \pm 0.11$ and $\alpha = 5.76 \pm 0.04$, for the different core current models are presented in figure 27. It is assumed that the differences in the s-α stability boundaries for the different core current models are related to the effective shift of the maximum of the normalized pressure gradient and to the differences in the safety factor profiles. Furthermore, figure 26 also shows a comparison of the Redl and Sauter bootstrap current models. As a result, differences between the Sauter and Redl model vanish for low and high densities, while the "pressure drop" is steeper for the Redl model. Finally, for the parabolic core current model, the stability boundary

considering only the toroidal mode number $n = 40$ is displayed. Comparison to the stability diagrams discussed in section 2.1 (figure 5 on page 11) indicates that the high-n boundary is associated with high-n ballooning mode stability.
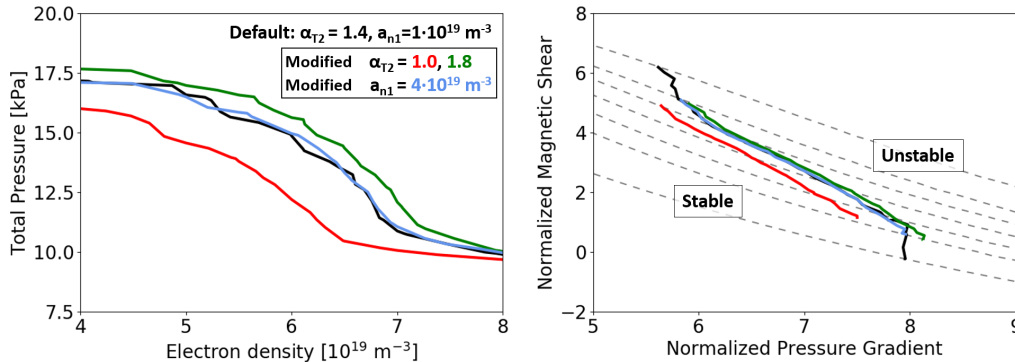

Figure 28: Ideal stability boundaries using DIII-D parameters with $\kappa = 1.89$ and $\delta = 0.4$. Left: p-n space, Right: s-α space. Black: Default EPED parameters $a_{n1} = 1 \cdot 10^{19}$ m^{-3} and $\alpha_{T2} = 1.4$, Blue: $a_{n1} = 4 \cdot 10^{19}$ m^{-3}, Red: $\alpha_{T2} = 1.0$, Green: $\alpha_{T2} = 1.8$.

Finally, we also tested the influence of two fixed EPED model parameters, defining the shape of the core pressure profile, namely a_{n1} and α_{T1}. As shown in figure 28, changing the core density gradient a_{n1} has nearly no effect on the stability. However, there is a significant difference related to changes of the core temperature profile shape α_{T2}. This is probably because α_{T2} strongly affects the "spike" located at the pedestal top of the temperature gradient profile (see figure 18a page 35). Moreover as $\alpha_{T2} \to 1$ the "spike" transforms to a discontinuity of the temperature gradient profile, which might explain the stronger effect of "$\alpha_{T2} = 1.4 \to 1.0$" compared to "$\alpha_{T2} = 1.4 \to 1.8$".

4.2 AUG: Trends and scaling laws

In the following section we study the influences of the model input parameters on ideal edge stability in detail. Firstly, three major trends of the stability boundaries with model input parameters are presented in p-n and s-α space. Secondly, several scaling laws are developed from a data set created with IPED 2. Finally, example stability boundaries for negative triangularity are shown. If not otherwise specified, the standard "AUG" parameters, as specified in the appendix B.2 "Parameter sets", with $\kappa = 1.6$ are used. The current profiles are created from the parabolic core model and the Redl bootstrap model.

From the last section, it is already known that we generally observe a low-n boundary at low densities and a high-n boundary at high densities, which are connected by a transition region limited by intermediate mode numbers that we have called the "pressure drop" boundary. The mode number boundaries are, for the observed parameter sets, always qualitatively equal to the mode boundaries shown in figure 23, having straight low mode number boundaries and "parabola shaped" high mode number boundaries in p-n space. However, when looking at a fixed density interval, one might not be able to see all three regimes of stability boundaries at once, as the high-n or low-n boundaries are maybe located outside of the fixed density frame.
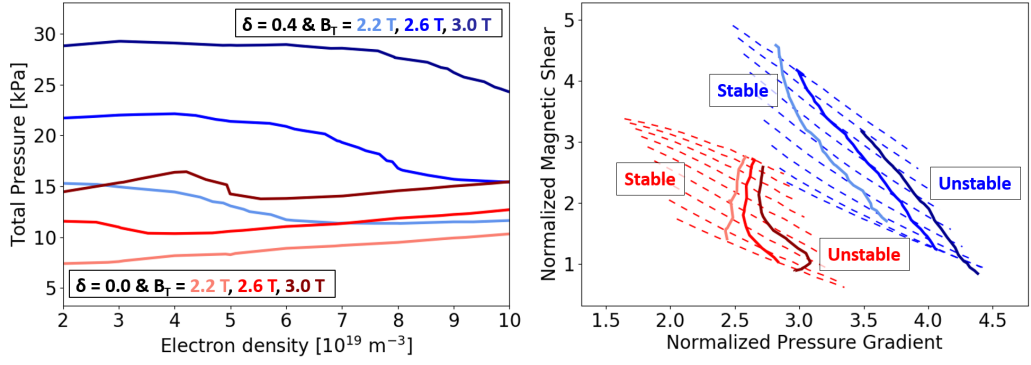
Figure 29: Ideal stability boundaries for $\delta = 0.0$ (red boundaries) and $\delta = 0.4$ (blue boundaries) in p-n (left) and s-α (right) space. Toroidal magnetic fields at the magnetic axis are $B_T = 2.2$ T (bright), $B_T = 2.6$ T (medium) and $B_T = 3.0$ T (dark). Solid: Stability boundaries, Dashed: Lines of constant density. Note that the lines of constant density might vary for the different stability boundaries but can be seen as a guide for the eye.

Firstly, as shown in figure 29, we observe strong trends of the edge stability with the toroidal magnetic field B_T and the triangularity δ in both the p-n and s-α space, where we kept all other model input parameters fixed. Variations of the toroidal magnetic field are related to variations of the edge safety factor $q_a \sim B_T/I_P$. Increasing the toroidal magnetic field B_T or the triangularity δ increases the critically stable pedestal top pressure and shifts the pressure drop boundary to higher densities. Moreover, the height of the drop Δp_{ped} increases with increasing toroidal magnetic field B_T or the triangularity δ, indicating a stronger trend for the low-n boundary compared to the high-n boundary. In s-α space, the high-n boundary at high normalized shear is transverse to the lines of constant density, the pressure drop is more parallel to the lines of constant density and the low-n boundary is transverse to the lines of constant density again, as indicated in figure 29. The different boundaries are especially pronounced for the $\delta = 0$ case in both the p-n and s-α space.
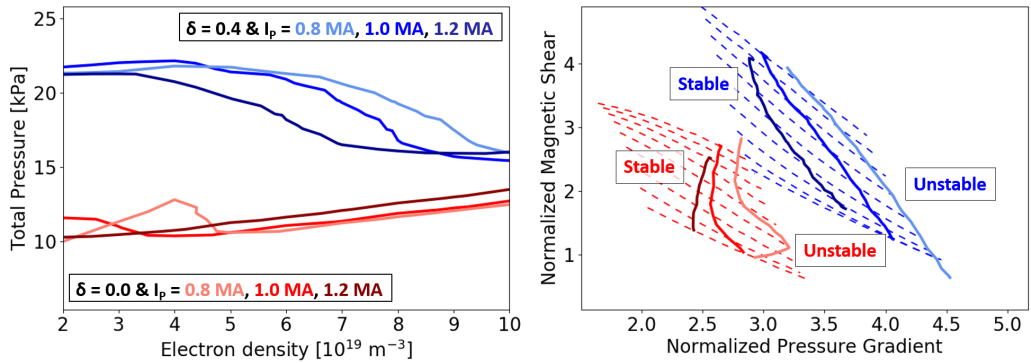
Figure 30: Ideal stability boundaries for $\delta = 0.0$ (red boundaries) and $\delta = 0.4$ (blue boundaries) in p-n (left) and s-α (right) space. Plasma currents are $I_P = 0.8$ MA (bright), $I_P = 1.0$ MA (medium) and $I_P = 1.2$ MA (dark). Solid: Stability boundaries, Dashed: Lines of constant density. Note that the lines of constant density might vary for the different stability boundaries but can be seen as a guide for the eye.

Figure 30 shows the trend of the stability boundary with increasing plasma current for $\delta = 0$ and $\delta = 0.4$. While there is a strong trend in the s-α space, where increasing plasma current decreases stability, there is nearly no influence on the critical pedestal top pressure in the p-n space. However, increasing plasma current shifts the pressure drop boundary to lower densities. This allows modest control over the position of the pressure drop boundary. Furthermore, the trends with B_T and $1/I_P$, i.e. with the edge safety factor, are nearly equal in the s-α space (see figures 29 and 30), while the trends in the p-n space are significantly different. The differences between the B_T and I_P trends in p-n space are due to the dimensionality of the pressure and the density and vanish for dimensionless pressure and density coordinates, which can be seen from the dimensionless scaling laws presented later in this section. Finally, it is remarkable that for increasing plasma current the shift of the pressure drop might results in an average decrease of the critical pressure at a fixed density if all other input parameters are kept constant.

In order to understand the observed trends quantitatively, scaling laws describing the pedestal stability were developed. Initially, our data set included IPED 2 scans covering all combinations of

$$B_T[\mathrm{T}] \in \{2.2, 2.6, 3.0\} \quad , \quad I_P[\mathrm{MA}] \in \{0.8, 1.0, 1.2\} \quad , \quad \beta_N \in \{1.4, 1.8, 2.3\} \quad (102)$$

$$\delta \in \{0.0, 0.4\} \quad , \quad n_{\mathrm{e,ped}}[10^{19}\mathrm{m}^{-3}] \in \{2, 4, 6, 8, 10\} \quad (103)$$

As the number of combinations of this rigorous grid-like parameter scan quickly increases with additional varied input parameters, not every parameter combination is included in the following extensions of the data set, where we also aimed to scan more triangularities and get variation in κ, w_{pre} and the aspect ratio. With the first extension, we included $\kappa = 1.8$, where we fixed $\beta_N = 1.8$ but varied the remaining parameters as in equations 102 and 103. For the second extension, we randomly chose 30 parameter combinations of equation 102 combined with

$$\delta \in \{-0.2, 0.0, 0.2\} \quad , \quad \kappa \in \{1.4, 1.7, 1.8\} \quad , \quad w_{\mathrm{pre}} \in \{0.08, 0.11, 0.15\} \quad (104)$$

where, in addition, for the last 20 combinations the minor and major radius were chosen from $(R_{\mathrm{maj}}, a) \in \{(1.62, 0.6), (1.35, 0.5)\}$ resulting in an aspect ratio of 2.7 instead of the default AUG aspect ratio of 3.3; each of the randomly chosen parameter combinations was scanned for $n_{\mathrm{e,ped}}[10^{19}\mathrm{m}^{-3}] \in \{2, 4, 6, 8, 10\}$, resulting in 150 scans. The final data set excluding failed runs contains $N = 402$ scans, i.e. data points. The pedestal top pressure was scanned in steps of $\Delta p_{\mathrm{ped}} = 1$ kPa. Note that every of the 402 scans results from ~ 180 stability calculations, where it was assumed that on average stability has to be determined for ~ 15 pedestal top pressures.

The correlations between the parameters of the final data set are presented in figure 31. Except from major and minor radius, there is nearly no correlation between the input parameters. To obtain dimensionless scaling laws, we introduce dimensionless scaling quantities: The normalized density $\widehat{n}_e = n_{\mathrm{e,ped}}/n_{\mathrm{GW}}$ normalized with respect to the Greenwald density $n_{\mathrm{GW}} = I_P/(\pi a^2)$, the edge safety factor $\widehat{q} = (2\pi a^2 B_T)/(\mu_0 I_P R_{\mathrm{maj}}) \cdot (1 + \kappa^2)/2$ for elongated plasma cross-sections (similar to equation 55 on page 21) and the modified triangularity of the LCFS $\widehat{\delta} = 1 + \delta > 0$. Note that the Greenwald density is an empirical quantity that cannot be derived from the dimensionless MHD equations. For the scaling laws, the inverse aspect
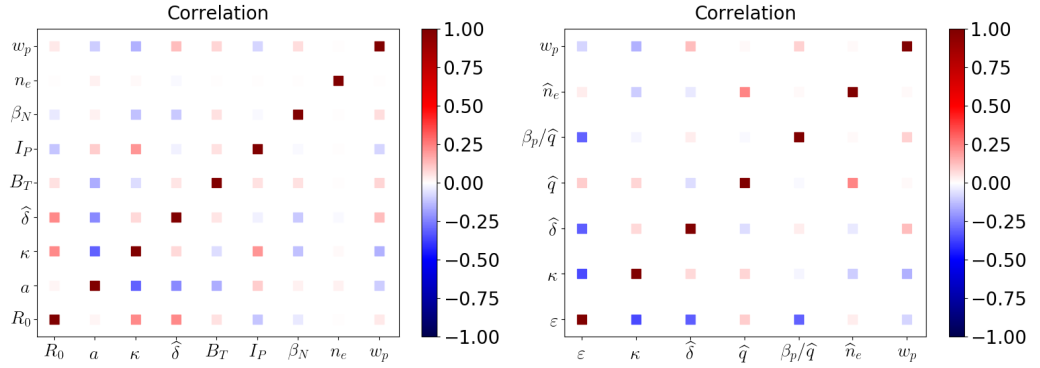
Figure 31: Parameter correlations of the final data set used as a basis for the scaling laws including $N = 402$ scans. Left: Model input parameters, Right: Normalized parameters used for the scaling laws.

ratio ϵ and the elongation κ are evaluated at the LCFS. Furthermore, we abbreviate the poloidal beta by $\beta_p = \beta_{\text{pol}}$ and the "KBM/transport" prefactor by $w_p = w_{\text{pre}}$. Because both $\widehat{q}$ and β_p are proportional to B_T/I_P, they are intrinsically correlated. For this reason, instead of fitting a quantity f directly with the dimensionless quantities $\widehat{q}$ and β_p, we fit with the less correlated parameters $\widehat{q}$ and $\beta_p/\widehat{q}$. Then, the total scaling exponent of $\widehat{q}$ can be determined using the identity

$$f \sim \widehat{q}^{c_1} \beta_p^{c_2} = \widehat{q}^{c_1+c_2} (\beta_p/\widehat{q})^{c_2} \ .$$

This method allows the exponents to be determined from a less correlated data set by disentangling the correlated quantities $\widehat{q}$ and β_p. The correlations of the normalized or dimensionless input parameters are displayed in figure 31. Except from the inverse aspect ratio, there are nearly no correlations between the scaling parameters. However, as none of the scaling laws that will be presented in this chapter are dependent on the aspect ratio, this correlation has no impact. There is a small correlation of $\widehat{n}_e$ and $\widehat{q}$ as both quantities are proportional to $1/I_P$, which might be avoided by directly using $\widehat{n}_e$ as an IPED 2 input replacing $n_{\text{e,ped}}$.

The scaling exponents are determined by linear regression on the logarithm of the dimensionless data set using the method of ordinary least squares. For all scaling laws, the standard deviations σ_{std} of every scaling exponent and the variance inflation factors VIF of every scaling parameter are provided in the appendix A.3, where the latter is a common measure for multicollinearity of a quantity with respect to the underlying data set. Moreover, as $\sigma_{\text{std}} \sim \sqrt{\text{VIF}}$, the VIF $\geqslant 1$ might be interpreted as the increase of standard deviation caused purely by multicollinearity of the data.

Firstly, a scaling for the critically stable poloidal pedestal beta β_{pp} was determined including all $N = 402$ data points, which yields:

$$\boxed{\beta_{pp} = 0.686 \cdot \kappa^{0.50} \ \widehat{\delta}^{1.68} \ \widehat{q}^{1.61} \ \beta_p^{0.33} \ \widehat{n}_e^{0.06} \ w_p^{1.29}} \tag{105}$$

with a fit determination of $R^2 = 90.8\%$ and a root mean squared error of RMSE $= 0.076$. The scaling and the parameter correlations are shown in figure 32. This scaling is based on nearly uncorrelated data and provides a good description of the average critical poloidal beta in p-n space. However, because the density dependence varies strongly over the high-n, low-n and pressure drop boundaries,
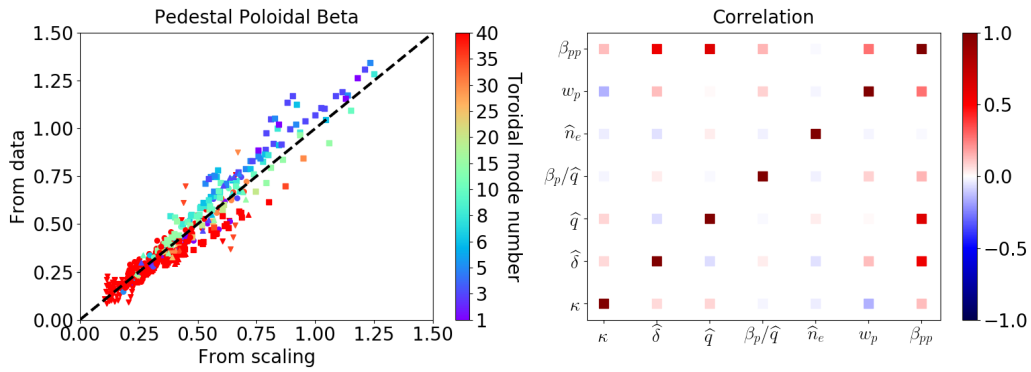
Figure 32: Scaling of the critically stable poloidal pedestal beta β_{pp} (left) and correlations between the scaling parameters (right) including all $N = 402$ data points. Symbols (left): $\delta = -0.2$ (▼), $\delta = 0.0$ (●), $\delta = 0.2$ (▲) and $\delta = 0.4$ (■).

this dependence cannot be covered by a single scaling. Consequently, there is a significant split between the high-n and low-n limited points in the scaling displayed in figure 32. Finally, there are some negative triangularity scans (▼ symbols) which appear as vertical groups in the scaling plot. These scans are characterized by high-n limited critical pressures that strongly depend on the density. The strong density dependence of these scans, which is poorly described by $\beta_{pp} \sim \widehat{n}_e^{0.06}$, is discussed in the "negative triangularity" part at the end of this section.

Because of the splitting of high-n and low-n limited critical pressures in figure 32 and to obtain quantitative information on the pressure drop, we determined separate scaling laws for both the high-n and low-n boundaries, where we restricted data points to destabilizing toroidal mode numbers of $30 \leqslant n \leqslant 40$ and $1 \leqslant n \leqslant 8$, respectively. The resulting scaling law for the high-n boundary yields:

$$\boxed{\beta_{pp}^{n \geqslant 30} = 1.894 \cdot \widehat{\delta}^{1.03}\ \widehat{q}^{1.03}\ \beta_p^{0.31}\ \widehat{n}_e^{0.28}\ w_p^{1.33}} \tag{106}$$

with $N = 227$, $R^2 = 91.2\%$ and RMSE $= 0.042$. Figure 33 shows the scaling as well as the correlations between the scaling parameters. In the data set restricted
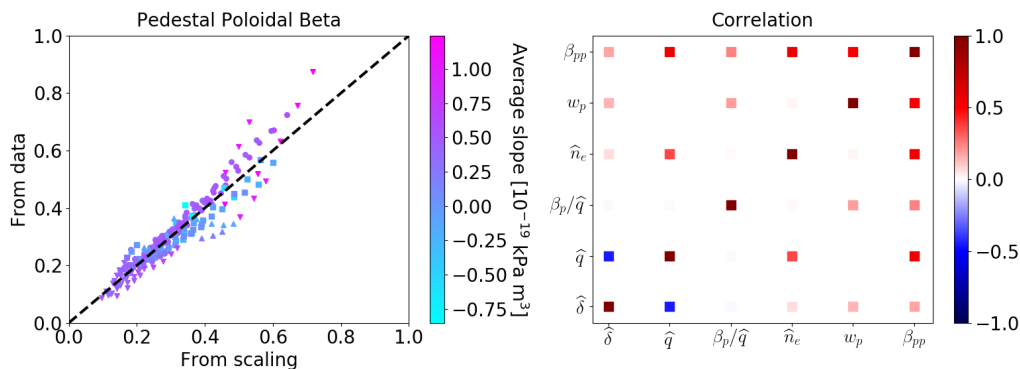

Figure 33: Scaling of the critically stable poloidal pedestal beta β_{pp} (left) and correlations between the scaling parameters (right) restricted to the high-n limited data points $n \geqslant 30$. Symbols (left): $\delta = -0.2$ (▼), $\delta = 0.0$ (●), $\delta = 0.2$ (▲) and $\delta = 0.4$ (■).

to $n \geqslant 30$, there are two major correlations: $\widehat{\delta} \rightleftharpoons \widehat{q}$ and $\widehat{q} \rightleftharpoons \widehat{n}_e$, where we denote correlations between two quantities by " $\rightleftharpoons$ ". These are caused by the restriction to $n \geqslant 30$, which creates a dependence of the densities contained in the data set on the parameters that influence the location of the pressure drop. We will discuss these correlations later in this section, when a scaling for the density at which the pressure drop is located is shown. Furthermore, the coloring of the data points in figure 33 (left) refers to the average slope $\Delta p / \Delta n$ of their respective high-n stability boundary in p-n space. This means that critical pressures belonging to the same stability boundary have equal color. Typically the high-n boundary has a positive slope for $n_{\mathrm{e,ped}} \gg n_D$, where n_D is the density at which the pressure drop is located. However, there are few data points with a negative average slope of the high-n boundary, which usually indicates that their respective stability boundary is close to the pressure drop. An example for a high-n boundary with negative average slope is given by the blue boundary in figure 20 (right) on page 39. Moreover, the negative triangularity scans which were poorly described by the weak density dependence $\beta_{pp} \sim \widehat{n}_e^{0.06}$ in equation 105 also show significant deviations from the high-n scaling law $\beta_{pp} \sim \widehat{n}_e^{0.28}$ (magenta ▼-symbols in figure 33). This indicates that it is challenging to describe the density dependence of β_{pp} with a simple scaling in $\widehat{n}_e$.

Next, the scaling law for the low-n boundary is determined to:

$$\boxed{\beta_{pp}^{n \leqslant 8} = 0.766 \cdot \kappa^{1.27} \; \widehat{\delta}^{1.98} \; \widehat{q}^{1.40} \; \beta_p^{0.25} \; \widehat{n}_e^{0.09} \; w_p^{1.41}} \tag{107}$$

with $N = 88$, $R^2 = 97.2\%$ and RMSE $= 0.037$. The scaling as well as the correlations between the scaling parameters are displayed in figure 34. As for the high-n scaling, there are significant correlations $\widehat{\delta} \rightleftharpoons \widehat{q}$ and $\widehat{q} \rightleftharpoons \widehat{n}_e$ caused by the restriction to $n \leqslant 8$, which are discussed later. The correlation $\kappa \rightleftharpoons \widehat{q}$ is caused by the small amount of the randomly generated samples with varying κ and might be avoided by a larger sample size. However, fixing the elongation to $\kappa = 1.6$ resulted in equal scaling exponents within the uncertainties of the regression. Furthermore, the low-n stability boundaries seem to be steeper at lower triangularities, which is similar to the trend observed for the high-n boundaries. Finally, there are no pressure drops for $\delta = -0.2$, as we observe only high-n limited critical pressures for
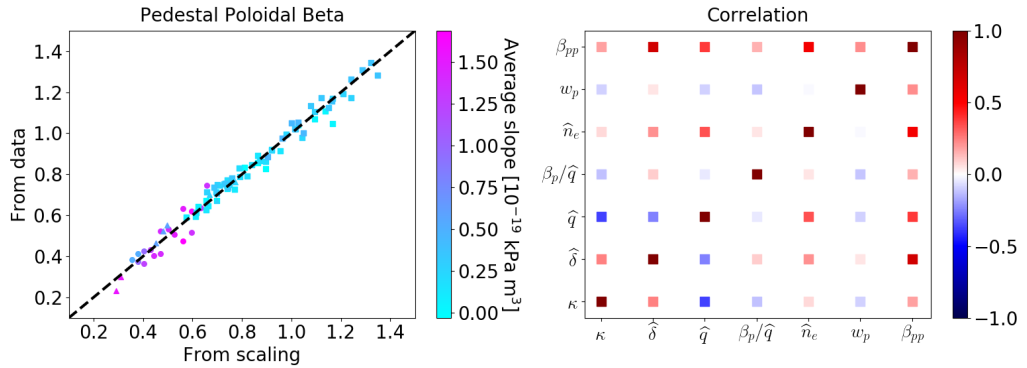

Figure 34: Scaling of the critically stable poloidal pedestal beta β_{pp} (left) and correlations between the scaling parameters (right) restricted to the low-n limited data points $n \leqslant 8$. Symbols (left): $\delta = 0.0$ (●), $\delta = 0.2$ (▲) and $\delta = 0.4$ (■).

negative triangularity. Comparing equations 106 and 107, the major differences at fixed density $\widehat{n}_e$ are

$$\frac{\beta_{pp}^{n\leqslant 8}}{\beta_{pp}^{n\geqslant 30}} \sim \kappa^{1.27} \, \widehat{\delta}^{0.95} \, \widehat{q}^{0.37} \tag{108}$$

indicating that the pressure drop, i.e the difference between the low-n and high-n boundaries, increases mainly with shaping, which is consistent with our observations of p-n diagrams.

Finally, a scaling for the location of the pressure drop is determined, which provides a method to control the limiting stability boundary at a fixed density. For this purpose, we define the location of the pressure drop as

$$\widehat{n}_D \equiv \frac{1}{2} \cdot \left[\max_{n\leqslant 10}\{\widehat{n}_e\} + \min_{n\geqslant 30}\{\widehat{n}_e\} \right] \, .$$

Then, the drop scaling for fixed inverse aspect ratio $\varepsilon = 0.3$ yields:

$$\boxed{\widehat{n}_D = 0.022 \cdot \widehat{\delta}^{2.14} \, \widehat{q}^{1.98} \, \beta_p^{0.24}} \tag{109}$$

with $N = 39$, $R^2 = 91.9\%$ and RMSE $= 0.055$. Figure 35 shows the scaling and the correlations between the scaling parameters. We restricted the scaling to fixed inverse aspect ratio because only 3 pressure drops were observed for $\varepsilon = 0.37$. The pressure drop strongly varies with both $\widehat{\delta}$ and $\widehat{q}$. Therefore, simultaneously increasing or decreasing these quantities shifts pressure drop strongly to high or low densities, preventing observation of the high-n or low-n boundary, respectively. Thus, the restrictions to either the high-n or low-n boundary imply a negative correlation of $\widehat{\delta}$ and $\widehat{q}$ in the restricted data set. This explains the correlations $\widehat{\delta} \rightleftharpoons \widehat{q}$ and $\widehat{q} \rightleftharpoons \widehat{n}_e$ which we observed previously (see figures 33 and 34). Furthermore, the coloring in figure 35 indicates the width of the pressure drop

$$\Delta\widehat{n}_D \equiv \min_{n\geqslant 30}\{\widehat{n}_e\} - \max_{n\leqslant 10}\{\widehat{n}_e\}$$

where larger widths of the pressure drop $\Delta n_D \geqslant 2 \cdot 10^{19}\text{m}^{-3}$ were only observed for $\delta = 0.4$. To summarize the scaling laws, we find enhanced pedestal stability
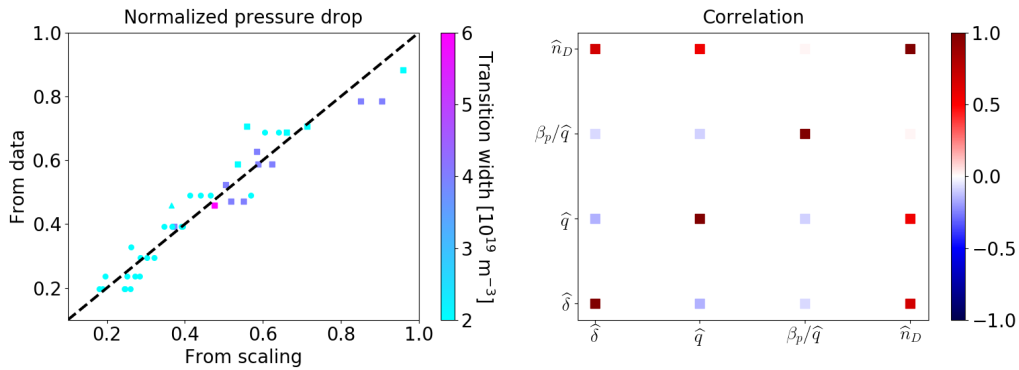

Figure 35: Scaling of the pressure drop location $\widehat{n}_D$ (left) and correlations between the scaling parameters (right). Symbols (left): $\delta = 0.0$ (●), $\delta = 0.2$ (▲) and $\delta = 0.4$ (■).

(equation 108) for high triangularities and safety factors (equation 109), which is limited by low mode numbers. While this is similar to the observations of [15], no Super H solutions were observed. Fixing all IPED 2 input parameters except I_P and B_T, equations 106 and 107 yield $p_{\text{ped}}^{n\geqslant 30} \sim I_P^{0.38}\, B_T^{1.34}$ and $p_{\text{ped}}^{n\leqslant 8} \sim I_P^{0.26}\, B_T^{1.65}$, respectively. This agrees well with the trends observed in figures 29 and 30.
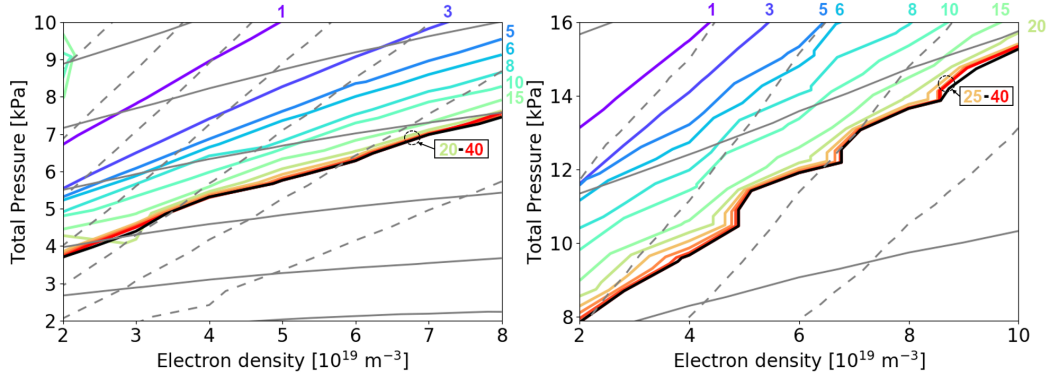

Figure 36: Ideal stability boundaries using AUG parameters with $\kappa = 1.7$ and $\delta = -0.2$. Left: $I_P = 0.6$ MA, $B_T = 2.0$ T, $w_{\text{pre}} = 0.11$, Right: $I_P = 0.8$ MA, $B_T = 2.2$ T, $w_{\text{pre}} = 0.15$. Colored: Stability boundaries considering only a single toroidal mode number n (see labels in the plot). Black: Stability boundary, Solid Gray: Lines of constant α with spacing $\Delta\alpha = 0.5$, Dashed Gray: Lines of constant s with spacing $\Delta s = 0.5$.

Finally, stability boundaries for negative triangularity $\delta = -0.2$ were determined over a large range of input parameters, where two example boundaries are shown in figure 36. At $\delta = -0.2$, all observed stability boundaries are purely high-n limited. While the critically stable pedestal pressures are typically small compared to positive triangularity cases, there are parameter sets which create exceptionally steep stability boundaries in p-n space (see figure 36, right). However, their steepness is mainly caused by the steep lines of constant normalized pressure gradient α, which "stretch" the stability boundary in p-n space. We will discuss the p-n to s-α mapping in detail in the next chapter. To summarize, the steepest stability boundaries are observed for broad pedestals $w_{\text{pre}} = 0.15$ and large elongations $\kappa \geqslant 1.7$.

5 Discussion

In order to understand the relation between stability boundaries in p-n space and in s-α space, we will derive a simplified analytical mapping $(s, \alpha) \mapsto (p, n)$. Using the EPED constraint and estimating the pressure gradient peak value by $(\partial_{\tilde{\psi}} p)_{\text{peak}} \sim p_{\text{ped}}/\Delta$, the peak value of α is estimated as:

$$\alpha \sim \frac{\sqrt{V}}{\psi_a^2} \cdot \partial_{\tilde{\psi}} V \frac{I_P \sqrt{p_{\text{ped}}}}{w_{\text{pre}}} \tag{110}$$

where $\partial_{\tilde{\psi}} V$ and V are evaluated at the peak position $\tilde{\psi}_{\text{peak}} = 1 - \frac{\Delta}{2}$. If $\Delta \ll 1$, the pressure dependence of $\partial_{\tilde{\psi}} V$ and V can be neglected and the mapping $\alpha \mapsto p$ is given by:

$$\boxed{\alpha \sim \frac{I_P \sqrt{p_{\text{ped}}}}{\psi_a^2 \cdot w_{\text{pre}}} \overset{\psi_a \sim I_P}{\Longrightarrow} p_{\text{ped}} \sim (w_{\text{pre}} I_P \alpha)^2} \tag{111}$$

This relation approximately describes the lines of constant normalized pressure gradient α in p-n space. However, equation 111 seems to be independent of the density, which cannot describe the steep lines of constant normalized pressure gradient α in figure 36 (page 51). The density dependence is contained in the dependence of the total flux ψ_a on the shape of the current density profile and is neglected when approximating $\psi_a \sim I_P$. For fixed total current I_P, a decreasing bootstrap current density usually increases the total flux by "smoothing" the integrated current profile. Thus, the lines of constant pressure gradient α are increasing with density, as $p_{\text{ped}} \sim (\psi_a(n_{\text{e,ped}})^2/I_P)^2 \sim \psi_a(n_{\text{e,ped}})^4$. In this approximation, the density dependence of ψ_a is amplified by a power of 4. Here, we ignored the pressure dependence of the edge current density $\psi_a(n_{\text{e,ped}}, p_{\text{ped}})$, which however has no effect on the qualitative description of the density dependence of the lines of constant α. One can see that a larger "transport prefactor" increases the slope of the lines of constant pressure gradient α by $p_{\text{ped}} \sim w_{\text{pre}}^2$, which is what we observed for the steep stability boundaries for $\delta = -0.2$ in the previous chapter.

Next, we want to derive a mapping $(s, \alpha) \mapsto n$. Firstly, a relation between peak shear and edge current density is given by the simple equilibrium relation $s = 2 - 2j_{\parallel} \cdot A(r = a)/I_P$ from equation 23 (page 9). Secondly, the current density is related to the electron density by the bootstrap current formula, which can be seen as a constraint that prescribes the "operational path" through the s-α space. Following [46], we use the simplified collisionality dependence of the neoclassical bootstrap transport coefficients $\mathcal{L}_{\square} \sim 1/(1 + \sqrt{\nu_{e,*}} + c_Z \nu_{e,*})$ with $c_Z \equiv (2Z_{\text{eff}})^{-2}$, where $\square$ is a placeholder for 31 or 32. Then, the edge peak current density, given by equation 34 (page 14), is approximated to:

$$j_{\parallel} = c_j \frac{\sqrt{p_{\text{ped}}}}{1 + \sqrt{\nu_{e,*}} + c_Z \nu_{e,*}} \tag{112}$$

with the proportionality constant c_j, where we additionally used equation 111, the EPED transport constraint and neglected the ion flow term $\tilde{\alpha} \mathcal{L}_{34}$ in equation 34.

Solving equation 112 for $\nu_{e,*}$ and using $\nu_{e,*} = c_\nu q (1 + \eta)^2 n_{e,ped}^3 Z_{eff}/p_{ped}^2$ (equation 36 on page 15) results in

$$
n_{e,ped}(s, p_{ped}) = \left[\frac{2 p_{ped} \sqrt{Z_{eff}}}{\sqrt{c_\nu}\ \sqrt{q}\ (1+\eta)} \left(\sqrt{(Z_{eff}^2 - 1) + \frac{2 c_j \sqrt{p_{ped}} A(r = a)}{I_P(2-s)}} - Z_{eff} \right) \right]^{2/3}
$$
(113)

where c_ν is a proportionality constant. Equation 113 describes the lines of constant shear in the p-n space. Inserting 111 into 113 yields the mapping $(s, \alpha) \mapsto n$. Thus, we have derived analytical mappings relating the p-n and the s-α space.
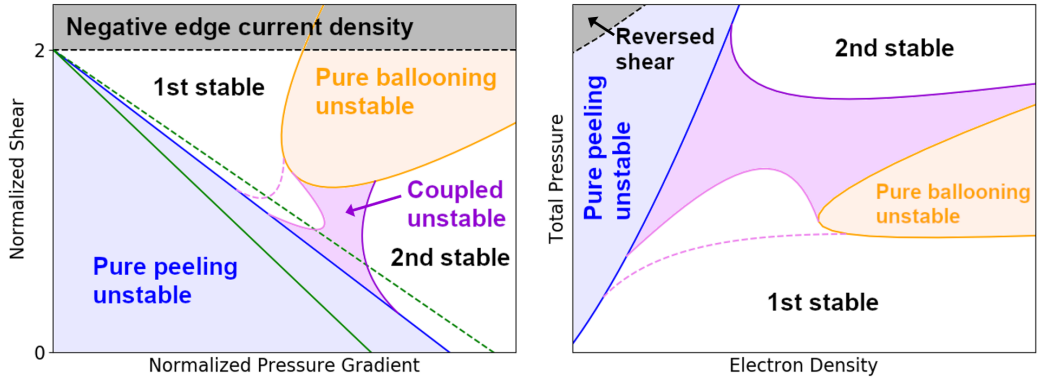

Figure 37: Sketch of the stability borders for pure high-n ballooning (orange) and peeling (blue) modes as well as lines to guide the eye for coupled peeling-ballooning stability borders (violet). Left: Boundaries in s-α space as shown in figure 5 for direct comparison of the p-n and the s-α space, based on [22], Right: Boundaries in p-n space using the mappings 111 and 113. The different shading of the coupled stability borders is to distinguish them. The violet dashed line is an artificially modified version of the coupled stability border, representing stronger coupling. The solid green line is the low collisionality bootstrap current limit $n_{e,ped} = 0$ corresponding to the p-n diagram on the right. The dashed green line marks a typical low collisionality bootstrap current limit for the observed stability diagrams presented in chapter 4.

At first, we apply the mappings 111 and 113 to the stability diagrams in s-α space that were derived in section 2.1 from the theory of peeling and ballooning modes. The pure high-n peeling and ballooning stability boundaries as well as coupled peeling-ballooning boundaries in s-α space, as discussed in section 2.1, and their mapping to p-n space are shown in figure 37. The solid bright violet line represents weak coupling between peeling and ballooning modes, usually observed for high positive triangularities, whereas the dashed bright violet line indicates stronger coupling between peeling and ballooning modes for less shaped plasma cross-sections (sketched based on [22]). In addition, for weak shaping, the ballooning and peeling unstable regions might intersect (see [12]), which is probably the case for the stability diagrams that we observed for the negative triangularity scenarios in section 4.2. As a result from figure 37, the obtained stability boundaries, using the strongly simplified mappings 111 and 113, are qualitatively equal to the stability boundaries determined with IPED2-HELENA-MISHKA presented in the previous chapter. As already motivated in the previous chapter, the high-n stability boundaries in the IPED2 stability diagrams are related to pure ballooning instability, as

they are equivalent in shape and location considering both p-n and s-α stability diagrams. Analogously, the low-n stability boundaries from IPED2 are associated with coupled peeling-ballooning or kink/peeling instabilities, where depending on the coupling between peeling and ballooning modes a pressure drop is observed (dashed and solid violet boundaries in figure 37). For this reason, we will identify the high-n and low-n boundaries shown in the previous chapter as "ballooning" and "peeling" boundaries, respectively. Here, we remind that the coupling between peeling and ballooning modes (dashed and solid violet boundaries) is strongly dependent on shaping (see equation 108). Finally, the pure high-n peeling boundary is expected to be typically located at inaccessibly high current densities which exceed the low collisionality bootstrap current limit. For the simplified stability diagrams in figure 37, the low collisionality bootstrap current, $j_\parallel \sim \alpha$ as $n_{e,ped} \rightarrow 0$, is represented by a straight line through $(s, \alpha) = (2, 0)$ in the s-α diagram (green lines) and is a lower bound for the "operational paths" that might prohibit access to the pure high-n peeling boundary. While the solid green line represents the low collisionality bootstrap current limit $n_{e,ped} = 0$ corresponding to the p-n diagram in figure 37 (right), the dashed green line marks a typical low collisionality bootstrap current limit for the observed stability diagrams presented in chapter 4.
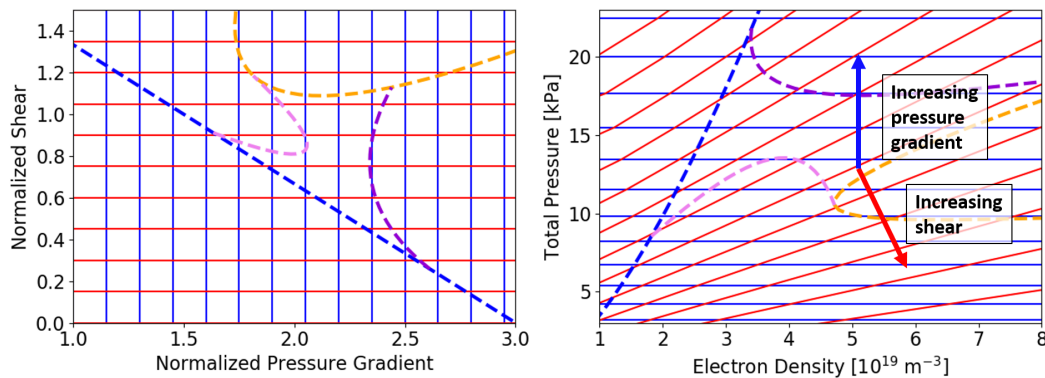

Figure 38: Lines of constant normalized magnetic shear (red) and normalized pressure gradient (blue), forming a mesh with spacing $\Delta s = \Delta \alpha = 0.15$ in s-α space (left). Transformation to p-n space (right) using the mappings 111 and 113 with equal parameters as for figure 37. Dashed lines: Stability borders for pure high-n ballooning (orange) and peeling (blue) modes as well as lines to guide the eye for coupled peeling-ballooning stability borders (violet) taken from figure 37.

Figure 38 displays a regular grid in s-α space and its transformation to p-n space using the mappings 111 and 113. One can see that the grid is strongly stretched and sheared by the transformation. Note that the lines of constant shear asymptotically approach the density axis as $s \rightarrow 2$, which is a direct consequence of equation 113, where $s > 2$ is associated with negative edge current densities. Furthermore, the stretching of the grid is approximately perpendicular to the "pressure drop" boundary, which implies that small uncertainties near the pressure drop in s-α space might be amplified by the transformation to p-n space.

A proper numerical transformation for an IPED 2 stability diagram is shown in figure 39. Comparing figures 38 and 39, the simplified mappings 111 and 113 seem to describe the numerical transformation remarkably well. However, effects of the precise bootstrap current model formulas of Sauter or Redl, the current density profile
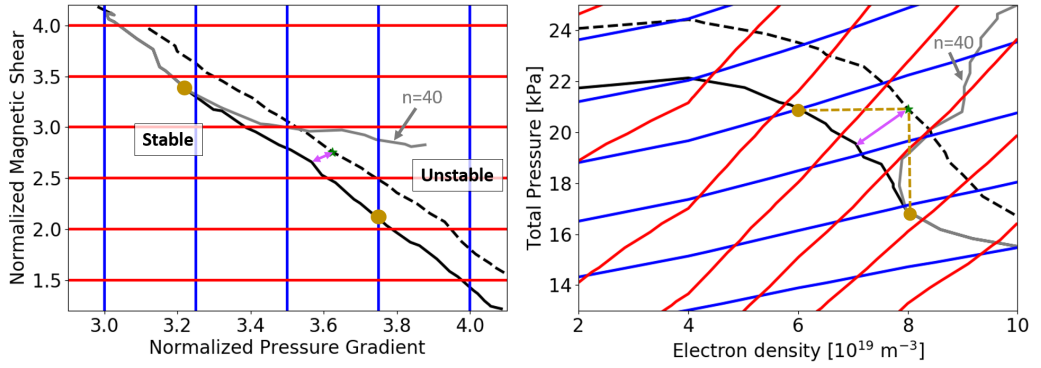
Figure 39: Ideal stability boundaries using AUG parameters with $\kappa = 1.6$ and $\delta = 0.4$; we used the parabolic core current model and Redl bootstrap model. Left: s-α space, Right: p-n space. Black: Stability boundary with $\gamma_{\text{thr}} = 0.04$ (solid) or $\gamma_{\text{thr}} = 0.0623$ (dashed), Red: Lines of constant shear s, Blue: Lines of constant pressure gradient α, Gray: Stability boundary for $\gamma_{\text{thr}} = 0.04$ considering only mode number $n = 40$. Green Star: Example IPED 2 scanned point, Violet Arrow: Indicating a displacement of the stability boundary to the green star. Yellow: Lines of constant top pressure or density through the green star (in p-n space) and their crossing points with the solid black boundary.

shapes as well as effects of the finite pedestal width Δ are not covered by the simple mappings. This is reflected by differences between figures 38 and 39 at low densities, i.e. collisionalities, and by the density dependence of the lines of constant normalized pressure gradient, as mentioned previously in this chapter. Next, we determine the transformation of uncertainties from the s-α to the p-n space. The dashed stability boundary in figure 39 marks critically stable pressures for $\gamma_{\text{thr}} = 0.0623$, meaning that growth rates on the dashed boundary are $\sim 56\%$ larger than on the solid boundary. Here, the dashed boundary was chosen so that it contains the displayed IPED 2 scanned point (green star), where the mapping $(s, \alpha) \mapsto (p, n)$ of the IPED 2 scanned point is given directly by HELENA and independent of the triangular interpolation. One can see that the large difference in growth rates between the solid and dashed boundaries is represented by a relatively small shift of the stability boundary in s-α space, indicating a sharp increase of the growth rates γ_{MHD} across the stability boundary. Thus, the stability boundary in s-α space is only weakly dependent on the choice of γ_{thr} or equivalently on uncertainties of the growth rates $\delta\gamma_{\text{MHD}}$. Quantitatively, the change $\delta\gamma_{\text{MHD}} \approx 56\%$ might be interpreted as a shift (violet arrow in figure 39) of the stability boundary by $\delta\alpha = 1.6\%$ and $\delta s = 3.8\%$, where we chose the shift to be small in s-α space since we are interested in the propagation of local uncertainties. This small deviation in s-α space is then transformed to a significantly larger deviation $\delta p_{\text{ped}} = 6.9\%$ and $\delta n_{\text{e,ped}} = 13.5\%$ in p-n space, which is also represented by a violet arrow in figure 39. The comparably large deviation in p-n space is caused by the strong stretching of the transformation perpendicular to the pressure drop boundary. It is remarkable that the observed amplification of $\delta p = 6.9\%$ is larger compared to the linear propagation estimate $\delta p \approx 2 \cdot \delta\alpha = 3.2\%$ based on equation 111, which follows from the density dependence of the lines of constant normalized pressure α. Finally, the effective error of the critically stable pedestal top pressure considering (experimental) operation at a fixed density in p-n space is $\delta p = 23.8\%$, which is illustrated by the vertical yellow line in figure 39.

In summary, uncertainties of the growth rate or stability boundary in s-α might be strongly amplified by the transformation to p-n space. In combination with the influence of the core current density shape shown in section 4.1, a precise prediction of the critically stable pressure in p-n space, especially near the pressure drop, is challenging. An uncertainty of the density where the pressure drop is located can strongly influence the predicted critically stable pedestal top pressure for operation at a fixed density.

Next, we discuss and compare some trends presented in the previous chapter. Firstly, we observed only a weak influence of changes of the edge current density on the stability boundary (figures 22 and 26) at high collisionalities. This is probably explained by the vanishing influence of finite changes δj_N of the normalized edge current density $j_N = j_\parallel \cdot A(r = a)/I_P$ on both the shear $\delta s \approx -j_N \cdot \delta j_N \to 0$ for $j_N \ll 1$ and the total poloidal flux because $I_P \gg I_{\mathrm{BS}}$, where $j_N \sim 1/\nu_{e,*} \ll 1$ for high collisionalities $\nu_{e,*} \gg 1$. In addition, the differences of stability boundaries using the Redl and the Sauter bootstrap current models vanish at low collisionalities, because the edge current densities predicted by the Redl and the Sauter models are approximately equal in the low collisionality regime. Thus, the bootstrap current model only affects the stability boundary at intermediate collisionalities. Finally, the structures of the mode number boundaries for positive and negative triangularities agree well with the findings of [16] or [47].

6 Conclusion and future work

The aim of this thesis was to upgrade the IPED framework and to study non-standard pedestal stability, in particular Super H and negative triangularity scenarios, for AUG. In order to improve the normalization of pressure and current density profiles, a new procedure for the estimation of equilibrium profiles was developed and implemented into IPED, which is a predictive framework determining pedestal stability that generates pressure profiles based on the EPED model. For this procedure, the equilibrium flux surface geometry is estimated and then iteratively a current density profile is determined that self-consistently combines the EPED and bootstrap current models. Hence, the converged current density profile generates a poloidal flux within the estimated flux surface geometry that results in a consistent edge current density calculated from the bootstrap current model. The differences between the estimated equilibrium profiles and their proper Grad-Shafranov solutions were observed to be small for the geometric profiles $V(\psi)$, $A(\psi)$ and $r(\psi)$ over a large range of plasma and shaping parameters. Deviations $\gtrsim 10\%$ were found for the estimated pedestal safety factor $q(\psi)$, which mainly affects the bootstrap current density in the high collisionality regime. However, the influence of the boot-strap current on the critically stable pressure was observed to be weak in the high collisionality regime, where we argue that this is related to the vanishing effect of the edge current density on normalized magnetic shear and poloidal flux at high collisionality.

The upgraded IPED2-HELENA-MISHKA framework was used to study MHD stability in s-α and p-n space. Based on the study of critical stability for every mode number separately, critical pedestal pressures were identified to be coupled low-n peeling-ballooning or kink/peeling mode limited at low densities and pure high-n ballooning limited at high densities. The transition between these regimes is limited

by intermediate mode numbers $n = 8 \sim 20$, where the critically stable pressures typically decrease from the "peeling" towards the "ballooning" limited stability boundary. In contrast to [15], we observed intermediate mode numbers to prohibit access to the Super H regime. That aside, we also obtain a beneficial influence of high triangularity and safety factor on critical stability, which shifts the transition regime ("pressure drop") to higher densities and stabilizes the "peeling" boundary. In order to optimize the pedestal top pressure, it is suggested to operate at high positive triangularity and high toroidal field at a density slightly below the density at which the "pressure drop" is located. Finally, studying different model specific influences of the EPED model, the core current shape affects the total poloidal flux and consequently the pressure gradient and safety factor, leading to significant changes of the stability boundary in p-n space.

To interpret our findings, we expressed the transition between s-α and p-n space by an analytical mapping, using a simplified bootstrap current formula. Applying the analytical transformation, the theoretically predicted s-α diagrams for peeling and ballooning stability aligned well with the p-n diagrams determined with IPED2-HELENA-MISHKA. Transforming a regular mesh from s-α to p-n space, one finds that small differences in the s-α space are significantly enlarged by the transformation. Finally, for operation at a fixed density that is near the "pressure drop" boundary, small uncertainties in the density imply massive changes to the critically stable pressure. In combination with the dependence of the critically stable pressure on the EPED "transport/KBM" prefactor, a precise prediction of critical stability in p-n space is challenging.

Future work might include evaluation of the different terms of the MHD work functional δW in order to obtain information on the energy composition of the instabilities. This can possibly provide insight into the stability of peeling and ballooning modes separately as well as into the coupling of these modes. Furthermore, a future version of IPED might be directly integrated into a Grad-Shafranov solver to improve the quality of the predicted safety factor profile, which would increase the accuracy of the predicted bootstrap current density. In addition, to understand the absence of Super H solutions in IPED2-HELENA-MISHKA, one might directly compare the MISHKA and ELITE codes for IPED2 scans and further analyze the influences of various EPED model details on the stability boundary in p-n space. Finally, the predictions of the IPED framework might be compared to experimental findings.

A Appendix

A.1 Sauter bootstrap formulas

The bootstrap coefficients defined by the Sauter model yield [31][32]:

$$\mathcal{L}_{31} = F_{31}(X = f_{t,31}, Z = Z_{\text{eff}}) \;, \qquad \mathcal{L}_{34} = F_{31}(X = f_{t,34}, Z = Z_{\text{eff}}) \tag{114}$$

$$\mathcal{L}_{32} = F_{32,\text{ee}}(X = f_{t,32,\text{ee}}, Z = Z_{\text{eff}}) + F_{32,\text{ei}}(X = f_{t,32,\text{ei}}, Z = Z_{\text{eff}}) \tag{115}$$

$$\sigma_{\text{neo}} = F_{33}(X = f_{t,33}, Z = Z_{\text{eff}}) \cdot \sigma_{\text{Spitzer}} \tag{116}$$

$$\tilde{\alpha} = \left(\frac{\tilde{\alpha}_0 + 0.25(1 - f_t^2)\sqrt{\nu_{i,*}}}{1 + 0.5\sqrt{\nu_{i,*}}} + 0.315\nu_{i,*}^2 f_t^6 \right) /(1 + 0.15\nu_{i,*}^2 f_t^6) \tag{117}$$

with the fit functions $F_\square$ and the effective trapped fractions $f_\square$ given by

$$f_{t,31} = \frac{f_t}{1 + (1 - 0.1f_t)\sqrt{\nu_{e,*}} + 0.5(1 - f_t)\nu_{e,*}/Z_{\text{eff}}}$$

$$f_{t,32,\text{ee}} = \frac{f_t}{1 + 0.26(1 - f_t)\sqrt{\nu_{e,*}} + 0.18(1 - 0.37f_t)\nu_{e,*}/\sqrt{Z_{\text{eff}}}}$$

$$f_{t,32,\text{ei}} = \frac{f_t}{1 + (1 + 0.6f_t)\sqrt{\nu_{e,*}} + 0.85(1 - 0.37f_t)\nu_{e,*}(1 + Z_{\text{eff}})}$$

$$f_{t,33} = \frac{f_t}{1 + (0.55 - 0.1ft)\sqrt{\nu_{e,*}} + 0.45(1 - f_t)\nu_{e,*}/Z_{\text{eff}}^{1.5}}$$

$$f_{t,34} = \frac{f_t}{1 + (1 - 0.1ft)\sqrt{\nu_{e,*}} + 0.5(1 - 0.5f_t)\nu_{e,*}/Z_{\text{eff}}}$$

$$F_{31} = X + (1.4X - 1.9X^2 + 0.3X^3 + 0.2X^4)/(Z + 1)$$

$$F_{32,\text{ee}} = \frac{0.05 + 0.62Z}{Z(1 + 0.44Z)}(X - X^4) + \frac{X^2 - X^4 - 1.2(X^3 - X^4)}{1 + 0.22Z} + \frac{1.2X^4}{1 + 0.5Z}$$

$$F_{32,\text{ei}} = \frac{0.56 + 1.93Z}{Z(1 + 0.44Z)}(X - X^4) + 4.95\frac{X^2 - X^4 - 0.55(X^3 - X^4)}{1 + 2.48Z} - \frac{1.2X^4}{1 + 0.5Z}$$

$$F_{33} = 1 - X + (-0.36X + 0.59X^2 - 0.23X^3)/Z$$

$$\tilde{\alpha}_0 = -\frac{1.17(1 - ft)}{1 - 0.22f_t - 0.19f_t^2}$$

where the trapped fraction f_t, effective charge Z_{eff} and collisionalities $\nu_{\square,*}$ are defined in section 2.3.1.

The Spitzer conductivity σ_{Spitzer} is given by [31][32]:

$$\boxed{\sigma_{\text{Spitzer}} = 1.9012 \cdot 10^4 \cdot \frac{(T_e[\text{eV}])^{1.5}}{Z_{\text{eff}}\, N_Z\, \ln(\Lambda_e)} \left[\frac{1}{\Omega\text{m}}\right] \quad , \quad N_Z = 0.58 + \frac{0.74}{0.76 + Z_{\text{eff}}}} \tag{118}$$

where the Coulomb logarithm $\ln(\Lambda_e)$ is defined in section 2.3.1.

A.2 Redl bootstrap formulas

The bootstrap coefficients defined by the Redl model yield [39][40]:

$$\mathcal{L}_{31} = F_{31}(X = f_{t,31}, Z = Z_{\text{eff}}) \ , \qquad \mathcal{L}_{34} = F_{31}(X = f_{t,34}, Z = Z_{\text{eff}}) \tag{119}$$

$$\mathcal{L}_{32} = F_{32,\text{ee}}(X = f_{t,32,\text{ee}}, Z = Z_{\text{eff}}) + F_{32,\text{ei}}(X = f_{t,32,\text{ei}}, Z = Z_{\text{eff}}) \tag{120}$$

$$\sigma_{\text{neo}} = F_{33}(X = f_{t,33}, Z = Z_{\text{eff}}) \cdot \sigma_{\text{Spitzer}} \tag{121}$$

$$\tilde{\alpha} = \left[\frac{\tilde{\alpha}_0 + (1 + 0.7(Z_{\text{eff}} - 1))\sqrt{0.25\nu_{i,*}f_t}}{1 + 0.35\sqrt{0.4\nu_{i,*}}} - 0.00025\nu_{i,*}^2 f_t^6 \right] \cdot$$
$$\cdot (1 + 0.0005\nu_{i,*}^2 f_t^6)^{-1} \tag{122}$$

with the fit functions $F_{\square}$ and the effective trapped fractions $f_{\square}$ given by

$$f_{t,31} = f_t \cdot \left[\frac{1 + 0.6(1 - 0.7f_t)\sqrt{\nu_{e,*}}}{0.2 + 0.8Z_{\text{eff}}} + \frac{0.7\nu_{e,*}}{(1 + \sqrt{Z_{\text{eff}} - 1}) \cdot (1 - 0.5f_t)} \right]^{-1}$$

$$f_{t,32,\text{ee}} = f_t \cdot \left[1 + 0.195(1 - f_t)\sqrt{\frac{1.2\nu_{e,*}}{Z_{\text{eff}}}} + 0.15(1 - 0.37f_t)\nu_{e,*} \cdot \right.$$
$$\left. \cdot \left(\sqrt{1 + 4(Z_{\text{eff}} - 1)^{1.5}} - f_t^2\sqrt{0.02(1 + 5(Z_{\text{eff}} - 1)^{1.5})\nu_{e,*}} \right)^{-1} \right]^{-1}$$

$$f_{t,32,\text{ei}} = f_t \cdot \left[1 + 0.85(1 + 0.4f_t)\sqrt{\frac{1.2\nu_{e,*}}{1 + 3\sqrt{Z_{\text{eff}} - 1}}} + 1.4875(1 - 0.4f_t) \cdot \right.$$
$$\left. \cdot (1.625 + 0.375Z_{\text{eff}})\nu_{e,*} \right]^{-1}$$

$$f_{t,33} = f_t \cdot \left[1 + \frac{0.6(1 - 0.4f_t)\nu_{e,*}}{\sqrt{Z_{\text{eff}}}} + (0.35 - 0.15f_t) \cdot (1 + 0.25\sqrt{Z_{\text{eff}} - 1})\sqrt{0.33\nu_{e,*}} \right]^{-1}$$

$$f_{t,34} = f_t \cdot \left[1 + \frac{0.4(Z_{\text{eff}} - 0.1f_t)\sqrt{1.3\nu_{e,*}}}{0.8 + 0.1Z_{\text{eff}}} + \frac{(1 - 0.5f_t)\nu_{e,*}}{Z_{\text{eff}}} \right]^{-1}$$

$$F_{31} = X + (X - 1.5X^2 + 0.2X^3 + 0.3X^4)/(8Z - 5.9)$$

$$F_{32,\text{ee}} = \frac{0.1 + 0.6Z}{Z(0.75 + 0.65(1 + (Z - 1)^{1.1}))}(X - X^4) +$$
$$+ \frac{0.7}{1 + 0.2Z}\left[X^2 - X^4 - 1.2(X^3 - X^4)\right] + \frac{1.3}{1 + 0.5Z}X^4$$

$$F_{32,\text{ei}} = -\frac{0.4 + 1.93Z}{Z(0.8 + 0.6Z)}(X - X^4) + \frac{5.5}{1.5 + 2Z}\left[X^2 - X^4 - 0.8(X^3 - X^4)\right] -$$
$$- \frac{1.3}{1 + 0.5Z}X^4$$

$$F_{33} = 1 - X + (-0.14X + 0.35X^2 - 0.21X^3)/Z$$

$$\tilde{\alpha}_0 = -\frac{0.62 + 0.018\tilde{\alpha}_I}{0.53 + 0.105\tilde{\alpha}_I}\frac{1 - f_t}{1 - 0.35f_t - 0.2f_t^2}$$

where the trapped fraction f_t, effective charge Z_{eff} and collisionalities $\nu_{\square,*}$ are defined in section 2.3.1 and the impurity strength is defined in section 2.3.2.

A.3 IPED 2 scaling laws

Standard deviations and VIFs for equation 105:

$$\beta_{pp} = 0.686 \cdot \kappa^{0.50} \; \widehat{\delta}^{1.68} \; \widehat{q}^{1.61} \; \beta_p^{0.33} \; \widehat{n}_e^{0.06} \; w_p^{1.29}$$

	κ	$\widehat{\delta}$	$\widehat{q}$	$\beta_p/\widehat{q}$	$\widehat{n}_e$	w_p
σ_{std}	0.13	0.04	0.05	0.04	0.02	0.06
VIF	1.04	1.07	1.02	1.01	1.00	1.08

Standard deviations and VIFs for equation 106:

$$\beta_{pp}^{n \geqslant 30} = 1.894 \cdot \widehat{\delta}^{1.03} \; \widehat{q}^{1.03} \; \beta_p^{0.31} \; \widehat{n}_e^{0.28} \; w_p^{1.33}$$

	$\widehat{\delta}$	$\widehat{q}$	$\beta_p/\widehat{q}$	$\widehat{n}_e$	w_p
σ_{std}	0.06	0.06	0.05	0.02	0.06
VIF	1.48	1.56	1.05	1.22	1.11

Standard deviations and VIFs for equation 107:

$$\beta_{pp}^{n \leqslant 8} = 0.766 \cdot \kappa^{1.27} \; \widehat{\delta}^{1.98} \; \widehat{q}^{1.40} \; \beta_p^{0.25} \; \widehat{n}_e^{0.09} \; w_p^{1.41}$$

	κ	$\widehat{\delta}$	$\widehat{q}$	$\beta_p/\widehat{q}$	$\widehat{n}_e$	w_p
σ_{std}	0.12	0.05	0.06	0.03	0.01	0.08
VIF	1.26	1.20	1.50	1.05	1.29	1.03

Standard deviations and VIFs for equation 109:

$$\widehat{n}_D = 0.022 \cdot \widehat{\delta}^{2.14} \; \widehat{q}^{1.98} \; \beta_p^{0.24}$$

	$\widehat{\delta}$	$\widehat{q}$	$\beta_p/\widehat{q}$
σ_{std}	0.14	0.16	0.11
VIF	1.03	1.03	1.02

B   Operators and definitions

B.1   Averages

Volume or standard flux-surface average:

$$\langle \dots \rangle_V \equiv \partial_V \int_{\mathcal{V}(r)} \dots \, \mathrm{d}\vec{x}^3 \quad \text{with} \quad V(r) = \int_{\mathcal{V}(r)} \mathrm{d}\vec{x}^3 \tag{123}$$

where $\mathcal{V}(r) \in \mathbb{R}^3$ and $V(r) \in \mathbb{R}$ represent the volume enclosed by a flux surface.

Area average:

$$\langle \dots \rangle_A \equiv \partial_A \int_{\mathcal{A}(r)} \dots \, \mathrm{d}\vec{x}^2 \quad \text{with} \quad A(r) = \int_{\mathcal{A}(r)} \mathrm{d}\vec{x}^2 \tag{124}$$

where $\mathcal{A}(r) \in \mathbb{R}^2$ and $A(r) \in \mathbb{R}$ represent the area enclosed by a flux surface in the (R, Z)-plane.

Transport or magnetic field average:

$$\langle \dots \rangle_B \equiv \langle \dots \cdot \vec{B} \rangle_V / B_T \tag{125}$$

where $\vec{B}$ is the total magnetic field and B_T is the value of the magnetic field at the magnetic axis. If "$\dots$" represents a vector-component parallel to the magnetic field, $\vec{B}$ is replaced by $|\vec{B}|$.

B.2   Parameter sets

Name	**R_{maj}** [m]	**a** [m]	**w_{pre}**	**Z_{eff}**	**Z_{imp}**	**I_P** [MA][*]	**B_T** [T][*]	**β_N**[*]
AUG	1.65	0.5	0.11	1.3	5.5	1.0	2.6	1.8
DIII-D	1.66	0.6	0.076	2.7	5.5	1.5	1.9	1.8
ITER	6.2	2.0	0.076	2.0	5.5	15.0	5.3	2.0

Table 1: Parameter sets for the different devices. [*] These plasma parameters are used if not otherwise specified. The DIII-D and ITER parameter sets are based on [15].

References

[1] J. Wesson. (2004). *Tokamaks - Third edition.* Oxford: Clarendon Press

[2] J. P. Freidberg. (2008). *Plasma Physics and Fusion Energy.* Cambridge: Cambridge University Press

[3] H. Zohm. (2016). *Plasma performance, burn and sustainment.* In G. H. Neilson (Ed.), *Magnetic Fusion Energy.* Cambridge: Woodhead Publishing.

[4] H. Zohm. (2015). *Magnetohydrodynamic Stability of Tokamaks.* Weinheim: WILEY-VCH Verlag GmbH & Co. KGaA

[5] R. J. Groebner. (1993). An emerging understanding of H-mode discharges in tokamaks*. *Phys. Fluids B: Plasma Physics*, 5(7), 2343.

[6] F. Wagner, G. Becker, K. Behringer, D. Campbell, A. Eberhagen, W. Engelhardt, G. Fussmann, O. Gehre, J. Gernhardt, G. v. Gierke, G. Haas, M. Huang, F. Karger, M. Keilhacker, O. Klüber, M. Kornherr, K. Lackner, G. Lisitano, G. G. Lister, H. M. Mayer, D. Meisel, E. R. Müller, H. Murmann, H. Niedermeyer, W. Poschenrieder, H. Rapp, H. Röhr, F. Schneider, G. Siller, E. Speth, A. Stäbler, K. H. Steuer, G. Venus, O. Vollmer, & Z. Yü. (1982). Regime of Improved Confinement and High Beta in Neutral-Beam-Heated Divertor Discharges of the ASDEX Tokamak. *Phys. Rev. Lett.*, 49(19), 1408.

[7] ASDEX Team. (1989). The H-Mode of ASDEX. *Nucl. Fusion*, 29(11), 1959.

[8] G. Federici, A. Loarte, & G. Strohmayer. (2003). Assessment of erosion of the ITER divertor targets during type I ELMs. *Plasma Phys. Control. Fusion*, 45(9), 1523.

[9] D. C. van Vugt, G. T. A. Huijsmans, M. Hoelzl, A. Loarte, ASDEX Upgrade Team, & EUROfusion MST1 Team. (2019). Kinetic modeling of ELM-induced tungsten transport in a tokamak plasma. *Phys. Plasmas*, 26(4), 042508.

[10] H. Zohm. (1996). Edge localized modes (ELMs). *Plasma Phys. Control. Fusion*, 38(2), 105.

[11] D. Lortz. (1975). The general "peeling" instability. *Nucl. Fusion*, 15(1), 49.

[12] J. W. Connor, R. J. Hastie, & H. R. Wilson. (1998). Magnetohydrodynamic stability of tokamak edge plasmas. *Phys. Plasmas*, 5(7), 2687.

[13] P. B. Snyder, R. J. Groebner, A. W. Leonard, T. H. Osborne, & H. R. Wilson. (2009). Development and validation of a predictive model for the pedestal height. *Phys. Plasmas*, 16(5), 056118.

[14] H. R. Wilson, P. B. Snyder, G. T. A. Huysmans, & R. L. Miller. (2002). Numerical studies of edge localized instabilities in tokamaks. *Phys. Plasmas*, 9(4), 1277.

[15] P. B. Snyder, W. M. Solomon, K. H. Burrell, A. M. Garofalo, B. A. Grierson, R. J. Groebner, A. W. Leonard, R. Nazikian, T. H. Osborne, E. A. Belli, J. Candy, & H. R. Wilson. (2015). Super H-mode: theoretical prediction and initial observations of a new high performance regime for tokamak operation. *Nucl. Fusion*, 55(8), 083026.

[16] A. Merle, O. Sauter, & S. Yu Medvedev. (2017). Pedestal properties of H-modes with negative triangularity using the EPED-CH model. *Plasma Phys. Control. Fusion*, 59(10), 104001.

[17] M. G. Dunne, L. Frassinetti, M. N. A. Beurskens, M. Cavedon, S. Fietz, R. Fischer, L. Giannone, G. T. A. Huijsmans, B. Kurzan, F. Laggner, P. J. McCarthy, R. M. McDermott, G. Tardini, E. Viezzer, M. Willensdorfer, E. Wolfrum, The EUROfusion MST1 Team, & The ASDEX Upgrade Team. (2016). Global performance enhancements via pedestal optimisation on ASDEX Upgrade. *Plasma Phys. Control. Fusion*, 59(2), 025010.

[18] A. B. Mikhailovskii, G. T. A. Huysmans, S. E. Sharapov, & W. Kerner. (1997). Optimization of computational MHD normal-mode analysis for tokamaks. *Plasma Phys. Rep.*, 23(10), 844.

[19] G. T. A. Huysmans, J. P. Goedbloed, & W. Kerner. (1991). Isoparametric Bicubic Hermite Elements for Solution of the Grad-Shafranov Equation. *Int. J. Mod. Phys. C*, 2(1), 371.

[20] I. B. Bernstein, E. A. Frieman, M. D. Kruskal, & R. M. Kulsrud. (1958). An energy principle for hydromagnetic stability problems. *Proc. R. Soc. Lond.*, 244(1236), 17.

[21] C. C. Hegna, J. W. Connor, R. J. Hastie, & H. R. Wilson. (1996). Toroidal coupling of ideal magnetohydrodynamic instabilities in tokamak plasmas. *Phys. Plasmas*, 3(2), 584.

[22] H. R. Wilson, & R. L. Miller. (1999). Access to second stability region for coupled peeling-ballooning modes in tokamaks. *Phys. Plasmas*, 6(3), 873.

[23] R. L. Miller, M. S. Chu, J. M. Greene, Y. R. Lin-Liu, & R. E. Waltz. (1998). Toroidal coupling of ideal magnetohydrodynamic instabilities in tokamak plasmas. *Phys. Plasmas*, 5(4), 973.

[24] D. D. Schnack, D. C. Barnes, D. P. Brennan, C. C. Hegna, E. Held, C. C. Kim, S. E. Kruger, A. Y. Pankin, & C. R. Sovinec. (2006). Computational modeling of fully ionized magnetized plasmas using the fluid approximation. *Phys. Plasmas*, 13(5), 058103.

[25] W. M. Tang, J. W. Connor, & R. J. Hastie. (1980). Kinetic-ballooning-mode theory in general geometry. *Nucl. Fusion*, 20(11), 1439.

[26] W. M. Tang, R. L. Dewar, & J. Manickam. (1982). Influence of diamagnetic drifts on critical beta in tokamaks. *Nucl. Fusion*, 22(8), 1079.

[27] R. J. Hastie, Peter J. Catto, & J. J. Ramos. (2000). Effect of strong radial variation of the ion diamagnetic frequency on internal ballooning modes. *Phys. Plasmas*, 7(11), 4561.

[28] P. B. Snyder, R. J. Groebner, J. W. Hughes, T. H. Osborne, M. Beurskens, A. W. Leonard, H. R. Wilson, & X. Q. Xu. (2011). A first-principles predictive model of the pedestal height and width: development, testing and ITER optimization with the EPED model. *Nucl. Fusion*, 51(10), 103016.

[29] B. D. Dudson, M. V. Umansky, X. Q. Xu, P. B. Snyder, & H. R. Wilson. (2009). BOUT++: A framework for parallel plasma fluid simulations. *Comput. Phys. Commun.*, 180(9), 1467.

[30] A. G. Peeters. (2000). The bootstrap current and its consequences. *Plasma Phys. Control. Fusion*, 42(Supplement), B231.

[31] O. Sauter, C. Angioni, & Y. R. Lin-Liu. (1999). Neoclassical conductivity and bootstrap current formulas for general axisymmetric equilibria and arbitrary collisionality regime. *Phys. Plasmas*, 6(7), 2834.

[32] O. Sauter, C. Angioni, & Y. R. Lin-Liu. (2002). Erratum: "Neoclassical conductivity and bootstrap current formulas for general axisymmetric equilibria and arbitrary collisionality regime" [Phys. Plasmas 6, 2834 (1999)]. *Phys. Plasmas*, 9(12), 5140.

[33] O. Sauter, R. W. Harvey, & F. L. Hinton. (1994). A 3-D Fokker-Planck Code for Studying Parallel Transport in Tokamak Geometry with Arbitrary Collisionalities and Application to Neoclassical Resistivity. *Contrib. Plasma Phys.*, 34(2-3), 169.

[34] R. W. Harvey, & M. G. McCoy. In *Proceedings of International Atomic Energy Agency Technical Committee Meeting on Advances in Simulation and Modeling of Thermonuclear Plasmas*, Montreal, 1992. (International Atomic Energy Agency, Vienna, 1993), p. 489.

[35] C. Angioni. Private communication.

[36] O. Sauter. (2013). A simple formula for the trapped fraction in tokamaks including the effect of triangularity. *CRPP-EPFL*: https://doi.org/10.13140/2.1.1351.3284 .

[37] E. A. Belli, J. Candy, O. Meneghini, & T. H. Osborne. (2014). Limitations of bootstrap current models. *Plasma Phys. Control. Fusion*, 56(4), 045006.

[38] E. A. Belli, & J. Candy. (2008). Kinetic calculation of neoclassical transport including self-consistent electron and impurity dynamics. *Plasma Phys. Control. Fusion*, 50(9), 095010.

[39] A. Redl. (2019). *Ein Satz von analytischen Formeln zur Berechnung des Bootstrapstromes in Tokamaks*. (Master Thesis). München: Ludwig-Maximilians-Universität.

[40] A. Redl. Private communication.

[41] P. B. Snyder, N. Aiba, M. Beurskens, R. J. Groebner, L. D. Horton, A. E. Hubbard, J. W. Hughes, G. T. A. Huysmans, Y. Kamada, A. Kirk, C. Konz, A. W. Leonard, J. Lönnroth, C. F. Maggi, R. Maingi, T. H. Osborne, N. Oyama, A. Pankin, S. Saarelma, G. Saibene, J. L. Terry, H. Urano, & H. R. Wilson. (2009). Pedestal stability comparison and ITER pedestal prediction. *Nucl. Fusion*, 49(8), 085035.

[42] P. B. Snyder, R. J. Groebner, J. W. Hughes, T. H. Osborne, M. Beurskens, A. W. Leonard, H. R. Wilson, & X. Q. Xu. (2011). A first-principles predictive model of the pedestal height and width: development, testing and ITER optimization with the EPED model. *Nucl. Fusion*, 51(10), 103016.

[43] P. A. Schneider, E. Wolfrum, R. J. Groebner, T. H. Osborne, M. N. A. Beurskens, M. G. Dunne, B. Kurzan, T. Pütterich, E. Viezzer, The ASDEX Upgrade Team, The DIII-D Team, & JET EFDA Contributors. (2013). Analysis of temperature and density pedestal gradients in AUG, DIII-D and JET. *Nucl. Fusion*, 53(7), 073039.

[44] T. Luda, C. Angioni, M. G. Dunne, E. Fable, A. Kallenbach, N. Bonanomi, P. A. Schneider, M. Siccinio, G. Tardini, The ASDEX Upgrade Team, & The EUROfusion MST1 Team. (2020). Integrated modeling of ASDEX Upgrade plasmas combining core, pedestal and scrape-off layer physics. *Nucl. Fusion*, 60(3), 036023.

[45] Y. Chen, S. E. Parker, J. Lang, & G.-Y. Fu. (2010). Linear gyrokinetic simulation of high-n toroidal Alfvén eigenmodes in a burning plasma. *Phys. Plasmas*, 17(10), 102504.

[46] O. Sauter, R. J. La Haye, Z. Chang, D. A. Gates, Y. Kamada, H. Zohm, A. Bondeson, D. Boucher, J. D. Callen, M. S. Chu, T. A. Gianakon, O. Gruber, R. W. Harvey, C. C. Hegna, L. L. Lao, D. A. Monticello, F. Perkins, A. Pletzer, A. H. Reiman, M. Rosenbluth, E. J. Strait, T. S. Taylor, A. D. Turnbull, F. Waelbroeck, J. C. Wesley, H. R. Wilson, & R. Yoshino. (1997). Beta limits in long-pulse tokamak discharges. *Phys. Plasmas*, 4(5), 1654.

[47] U. A. Sheikh, M. Dunne, L. Frassinetti, P. Blanchard, B. P. Duval, B. Labit, A. Merle, O. Sauter, C. Theiler, C. Tsui, the TCV Team, & the EUROfusion MST1 Team. (2019). Pedestal structure and energy confinement studies on TCV. *Plasma Phys. Control. Fusion*, 61(1), 014002.

Acknowledgements

At the end of this thesis, I want to express my gratitude to all people who supported this work.

Firstly, a special thanks goes to my academic supervisor **Hartmut Zohm**. Giving his lecture on hydrodynamics with contagious enthusiasm, he drew my attention to the field of plasma physics. I am also especially grateful for our fruitful discussions, which resulted in new approaches and majorly contributed to my understanding of plasma physics.

I want to thank my supervisor **Mike Dunne** for taking always time and for answering my countless questions. More than once, his critical view on results and our discussions made me rethink my initial conclusions. Finally, I also want to thank Mike for his attempts to make my English sound less German and for rigorously reading through numerous drafts of this work.

I am thankful for the discussions with **Phil Snyder** on the EPED framework and access to Super H modes. I also want to thank **Clemente Angioni** and **Andreas Redl** for answering my questions regarding the bootstrap current and definitions in the bootstrap current models. Finally, I am grateful to **Teo Luda** for the help with Python programming and the spontaneous discussions about new outcomes.

Furthermore, I am grateful for the positive atmosphere in the office with **Teo Luda** and **Christian Kiefer** and at IPP in general. A special thanks goes also to **Magdalena Bauer** for discovering hydrodynamics and plasma physics together and for being a great friend!

Finally, I want to thank my family and especially my parents **Stefan** and **Sabine** for their unconditional support. Thank you for always being there for me!

Erklärung

Hiermit erkläre ich, die vorliegende Arbeit selbständig verfasst zu haben und keine anderen als die in der Arbeit angegebenen Quellen und Hilfsmittel benutzt zu haben.

München, den _____   _____

                                                              Unterschrift, Jonas Puchmayr